2018

STEM CELL THERAPY FOR STROKE

ANUKA MINASSIAN

Vamos despacio
Para encontrarnos
El tiempo es arena en tus manos
Sé por tus marcas
Cuánto has amado
Más de lo que prometiste

Gustavo Cerati “Lago en el cielo”, 2006.

Document layout by Dániel Vincze (inspired by the art of M. F. Masman)

Max Planck Institute
for Metabolism Research

Universität
zu Köln

Stem Cell Therapy For Stroke

Modulation of structural and functional adjustments
after stem cell implantation
in a mouse model of cortical stroke

Inaugural-Dissertation
zur Erlangung des Doktorgrades
der Mathematisch-Naturwissenschaftlichen Fakultät
der Universität zu Köln

vorgelegt von
Anuka Minassian
aus Córdoba, Argentinien

Köln, 2018

Berichterstatter: (Gutachter)	Prof. Dr. Peter Kloppenburg Prof. Dr. Heike Endepols Prof. Dr. Mathias Höhn

Tag der mündlichen Prüfung: 21. November 2018

ABSTRACT

Stem cell therapy for ischemic stroke is an emerging field in light of an increasing number of patients surviving with permanent disability. Such stem cells entail the potential to differentiate into mature neurons and thus replace dysfunctional tissue or enhance the surviving tissue's plasticity. There is a strong need for imaging modalities which allow the tracking of neural stem cell differentiation longitudinally and non-invasively *in vivo*, and thus the monitoring of the therapeutic outcome of stem cell-based approaches.

Within this thesis, the fate of engrafted cells was monitored longitudinally *in vivo* via optical imaging and complemented with immunohistochemistry. Lightsheet Fluorescence Microscopy enabled the evaluation of the graft's spatial migration while electrophysiology was used to assess the phenotypic electric characteristics of the implanted cells. Cells were engrafted in both naïve and ischemic brains. Resting state fMRI and behavioral testing were used to assess the functional connectivity of the sensorimotor networks and the behavioral outcome, respectively.

To investigate the effect of neural stem cell implantation after the event of an ischemic stroke, I first characterized the changes caused by ischemia in the brain and in the functional network using the dMCAO model in mice. Following experimental stroke, mice demonstrated expected sensorimotor dysfunction and changes in the resting state sensorimotor network. Implantation of cells did not improve post stroke behavioral outcome. Moreover, in control animals, I observed changes in functional networks due to the stereotaxic procedure of engraftment and due to the damage caused to the meninges in dMCAO sham occlusion. This illustrates the sensitivity of resting state fMRI to all sort of surgical procedures in the brain. I hypothesize that such damages may have prevented functional and network recovery which has not been previously identified due to the application of different data analysis and the lack of proper control groups.

The findings in this thesis represent one of few preclinical studies in resting state fMRI network changes post stroke that apply this technique to evaluate functional outcomes following a potential clinically applicable human neural stem cell treatment for ischemic stroke. It was found that disruption of the network structural architecture e. g. by means of a needle puncture does not necessarily imply a decrease in the connectivity of the non-affected tissue and that injury caused by stereotaxic injection should be taken into account when assessing the effectiveness of treatment.

ZUSAMMENFASSUNG

Die Stammzelltherapie bei ischämischen Schlaganfällen geniesst zunehmendes Interesse angesichts einer wachsenden Zahl von Patienten, die mit einer dauerhaften Behinderung überleben. Diese Stammzellen bergen das Potenzial, sich in reife Neuronen zu differenzieren und so dysfunktionales Gewebe zu ersetzen oder die Plastizität des überlebenden Gewebes zu verbessern. Es besteht ein großer Bedarf an bildgebenden Verfahren, die es ermöglichen, die Differenzierung neuronaler Stammzellen im Zeitverlauf und nicht-invasiv *in vivo* zu verfolgen und damit den therapeutischen Erfolg stammzellbasierter Strategien zu verfolgen.

Im Rahmen dieser Arbeit wurde das Schicksal von transplantierten Zellen in in Longitudinalstudien *in vivo* mittels optischer Bildgebung beobachtet und durch Immunhistochemie ergänzt. Lichtblatt-Fluoreszenzmikroskopie ermöglichte die Charakterisierung der räumlichen Migration des Transplantats und die Elektrophysiologie wurde zur Beurteilung der zelltypischen elektrischen Eigenschaften der implantierten und differenzierten Zellen eingesetzt. Zellen wurden sowohl in naive als auch in ischämische Gehirne transplantiert. Ruhezustand fMRI und Verhaltenstests wurden verwendet, um die funktionelle Konnektivität der sensomotorischen Netzwerke bzw. Verhaltensdefizite und -verbesserungen zu beurteilen.

Um den Effekt der neuronalen Stammzellimplantation nach einem ischämischen Schlaganfall zu untersuchen, habe ich zunächst die durch Ischämie verursachten Veränderungen im Gehirn und im funktionellen Netzwerk mit dem dMCAO-Modell bei Mäusen charakterisiert. Nach einem experimentellen Schlaganfall zeigten Mäuse die erwartete sensorimotorische Dysfunktion und Veränderungen im Ruhezustand des sensorimotorischen Netzwerks. Die Implantation von Zellen hat das Verhaltensrgebnis nach einem Schlaganfall nicht verbessert. Darüber hinaus beobachtete ich bei Kontrolltieren Veränderungen in funktionellen Netzwerken nach stereotaktischer Transplantation und durch die Schädigung der Hirnhäute bei dMCAO Operation ohne tatsächlichen Gefäßverschluss. Dies demonstriert die Empfindlichkeit der Resting State fMRI für funktionelle Netzwerkveränderungen nach verschiedenen chirurgischen Eingriffen im Gehirn. Ich schließe daraus, dass solche chirurgischen Eingriffe allein bereits eine Funktions- und Netzwerkwiederherstellung verhindern, die aufgrund der Anwendung unterschiedlicher Datenanalysen und des Fehlens geeigneter Kontrollgruppen bisher nicht identifiziert wurde.

Die Ergebnisse in dieser Arbeit stellen eine der wenigen präklinischen Studien dar zu Änderungen des funktionellen Netzwerks nach Schlaganfall, die die Technik des resting state fMRI anwenden, um funktionelle Ergebnisse nach einer möglichen klinisch anwendbaren Behandlung mit humanen neuronalen Stammzellen für ischämischen Schlaganfall zu bewerten. Ich habe in meinen Untersuchungen gefunden, dass eine Störung der Netzwerkstrukturarchitektur, z. B. Durch eine Nadelpunktion, nicht unbedingt eine Verringerung der Konnektivität des nicht betroffenen Gewebes bedeutet und dass Verletzungen durch stereotaktische Injektion bei der Beurteilung des Behandlungserfolgs berücksichtigt werden müssen.

CONTENTS

1

CHAPTER 1

THEORETICAL BACKGROUND

1.1 Stroke

Stroke is a neurological disease that entails a heavy burden for global health and local governments. According to the World Health Organization (WHO), 16 million people have suffered from stroke for the first time in 2005, including the 5.7 million patients who died as a consequence of it (Strong et al., 2007). Also in the same year, the estimated incidence of stroke was 89 per 100000 individuals, a rate expected to rise due the ageing of the global population, and the resolution of epidemiological factors in developing countries (Lopez and Mathers, 2006).

Taken together, stroke and other vascular diseases such as ischemic heart disease, are the leading cause of death in adults. If stroke is isolated from the rest of vascular diseases, it becomes the second cause of death for patients above 60 years of age and the fifth cause of death for patients between 15 and 59 years of age (WHO 2018). One in six people are in risk of getting a stroke, one in three stroke patients dies and another third remains disabled (Mackay and Mensah 2013). Due to the prognosis that the incidence will impact heavier on the worldwide welfare, current research focuses on alleviating stroke incidence rates by improving prevention, acute phase response and post stroke care and rehabilitation strategies (Norrving and Kissela, 2013).

1.1.1 Pathogenesis of stroke

The WHO definition of stroke is: “rapidly developing clinical signs of focal (or global) disturbance of cerebral function, with symptoms lasting 24 hours or longer or leading to death, with no apparent cause other than of vascular origin” (WHO MONICA Project Investigators. The World Health Organization MONICA Project, 1988). By applying this definition, transient ischemic attack, which is defined to last less than 24 hours, and patients with stroke symptoms caused by subdural hemorrhage, tumors, poisoning or trauma are excluded.

The pathological background for stroke may either be ischemic or hemorrhagic disturbances of the cerebral blood circulation. Thrombotic cerebral infarction results from the atherosclerotic obstruction of large cervical and cerebral arteries, with ischemia in all or part of the territory of the occluded artery. This can be due to occlusion at the site of the main atherosclerotic lesion or to embolism from this site to more distal cerebral arteries.

Embolic cerebral infarction is secondary to embolism by a clot in the cerebral arteries coming from other parts of the arterial system, for example from cardiac lesion, either at the site of the valves or of the cardiac cavities, or due to rhythm disturbances with stasis of the blood, which allows clotting within the heart as seen in atrial fibrillation. Lacunal cerebral infarctions are small deep infarcts in the territory of small penetrating arteries due to a local disease of these vessels, mainly related to chronic hypertension. Several other causes of cerebral infarction exist and are of great practical importance for patient management. As they are relatively rare they can be ignored for most epidemiological purposes.

Spontaneous intracerebral hemorrhages (as opposed to traumatic ones) are mainly due to arteriolar hypertensive disease, and more rarely due to coagulation disorders, vascular malformation within the brain, and diet (such as high alcohol consumption, high LDL concentration, high blood pressure, etc.). Cortical amyloid angiopathy (a consequence of hypertension) is a cause of cortical hemorrhage especially occurring in elderly people and it is becoming increasingly frequent as populations become older. (www.who.int/healthinfo/statistics)

Once the artery has been occluded, the brain regions that are supported by the affected artery are then no longer sufficiently supplied with oxygen and glucose to guarantee a normal metabolism of the brain cells. This malnutrition of the brain parenchyma can lead to extensive cell death due to rapid ATP reduction, a metabolite that brain cells depend on for function and survival. Ionic gradients across membranes are highly and exclusively dependent on ATP which can only be anabolized from glucose provided by the blood stream. Since the ion gradient cannot be kept, excitotoxicity overcomes and the cells are rapidly irreversibly damaged and turn necrotic. Because of a high functional specialization of neurons, this cell type as well as oligodendrocytes are most susceptible to insufficient supply with oxygen and nutrients (Lo et al., 2003). Hence, this irreversible damage to the parenchyma is visible within minutes in the case of a complete stop of blood flow or its reduction below 10 ml / 100 g tissue / min. (Choi and Rothman, 1990).

The ischemic cascade, which is the process of degeneration following stroke, begins during the next few minutes after the insult, stretching to days afterwards. It entails energy metabolism failure, ionic imbalance, depolarization, excitotoxicity, oxidative and nitrosactive stress, spreading inflammation and finally the activation of the apoptotic pathway or the triggering of necrotic process (Lo et al., 2003, Muthaian et al., 2012). Excitotoxicity occurs when neurons depolarize due to lack of ATP, as stated above. Glutamate is uncontrollably released from the presynaptic vacuoles and attaches to postsynaptic receptors in adjacent neurons, which triggers calcium influx, activation of proteases and lipases. These enzymes digest DNA, proteins and lipids, damaging the entire structure of the cell (Neuhaus et al., 2017). Restoration of blood flow entails the release of pro-inflammatory cytokines and causes further damage to the already damaged tissue.

1.1.2 TREATMENT FOR STROKE

Mechanical removal of the clot by surgery is a therapy limited to those patients who can reach a high complexity diagnostic health institution where the clot can be localized with aid of a contrast agent and imaging equipment (Ellis et al., 2011). Apart from surgery, the only FDA approved treatment is the administration of tissue plasminogen activator (tPA) which can dissolve the clot totally or partially via fibrinolysis and reestablish blood flow to the ischemic tissue. For this treatment to be effective, tPA must be administered before 3 hours of stroke onset, or up to 4.5 – 6 hours in specific cases.

There have been several clinical trials of potential therapeutic molecules such as NMDA antagonists to prevent further excitotoxicity damage in the still viable ischemic area. To date, no effective therapies to restore function and structure of lost tissue are available in the clinic. Strategies to reduce

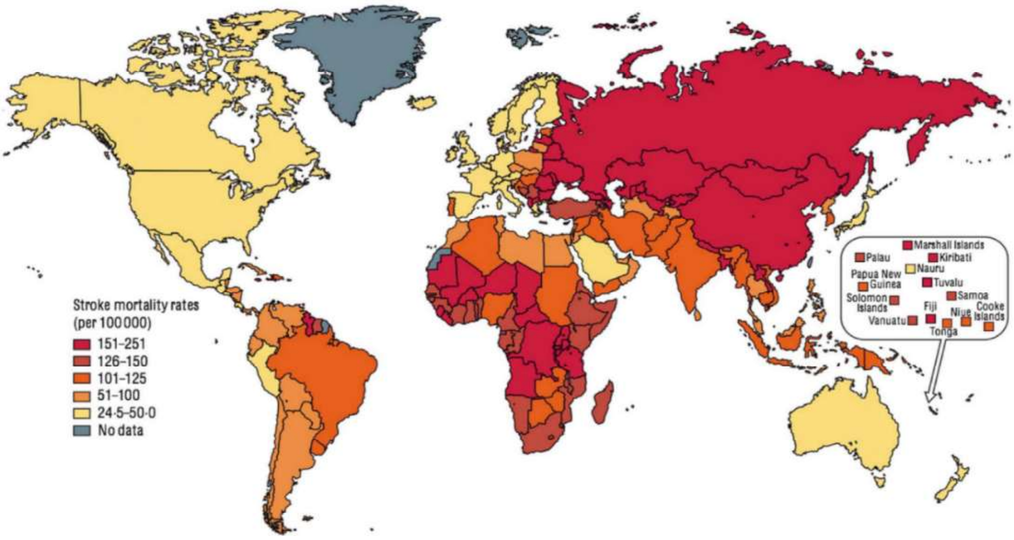

Figure 1.1: Epidemiology of stroke. Estimated mortality rates of stroke based on monitoring and modelling, from Norrving and Kissela, 2013.

the burden of stroke are focused on prevention, in an attempt to change lifestyles: sedentary habits and risk factors play a decisive role in the incidence of this pathology. Those patients that do not receive acute treatment or even some patients that are acutely treated are left with permanent impairments in their nervous system. Figure 1.1 reflects that the stroke mortality rate is higher in developing countries compared to developed countries, presumably due the lack of immediate access to health care facilities for all members of the population. There are many mortal stroke patients whose life could have been spared if they had received a thrombolytic treatment within the first hours after stroke onset. Efficient post-stroke therapies are needed if the massive impact of this neurological disease on global health is to be alleviated because no effective treatment to improve functional recovery exists in the post-ischemic phase for the surviving patients which results in a heavy burden on public health policies. Stem cell-based approaches could provide completely novel therapies to restore function after stroke (Lindvall and Kokaia 2011).

1.1.3 Animal models of ischemic stroke

Animal models are an invaluable resource for investigating the organ-wide and systemic effects of a pathology and/or therapeutic. In the case of stroke, they are essential for understanding the structural and functional changes which occur following local injury. The middle cerebral artery is the most commonly occluded vessel in humans (Heiss, 2016) and this is reflected in the *in vivo* models. Mice and rats are the most popular choice of species for preclinical stroke research due to lower relative costs, similar cerebrovasculature to man, the availability of comorbid / genetically modified models, well understood physiology, and greater ethical acceptance compared to non-human primates (Macrae, 2011). Middle cerebral artery occlusion (MCAO) can be carried out by a range of mechanical or pharmaceutical methods.

The most popular method of MCAO is the intraluminal filament method of mechanical occlusion (Koizumi et al., 1986a; Longa et al., 1989). Occlusion can be permanent or transient with the withdrawal of the coated filament after a prescribed period of time simulating reperfusion. The ischemic damage caused is primarily in the striatum and often the sensorimotor cortex. The method is popular due to the short procedural duration allowing for high throughput, and the absence of a need to perform a craniectomy. Occlusion can be confirmed by Laser Doppler Flowmetry with reasonable success, however, the method still carries a large variance in infarct volume as well as a risk of vessel rupture and intracerebral hemorrhage (Schmid-Elsaesser et al., 1998). Edematous swelling can cause death within 48 hours in large infarcts due to compression of the bulbar structures within the intact skull. In hypertensive rats, MCAO methods which involve craneotomy lead to lower mortality rates as the brain has space to expand, lowering intracranial pressure (Ord et al., 2012).

Other mechanical methods of MCAO include permanent occlusion of the MCA at proximal or distal locations via electrocoagulation (Tamura et al., 1981), or injection of an autologous blood clot (Kaneko et al., 1985). Electrocoagulation methods are more favorable for controlling infarct volume (by determination of which area of the MCA to occlude) and generation of favorable amounts of penumbra (Macrae, 2011), but require greater surgical skill and time.

Examples of pharmaceutical methods of MCAO are topical application of endothelin onto the MCA (Macrae et al., 1993), stereotaxic injection of endothelin into the brain parenchyma (Sharkey et al., 1993), intraluminal injection of thrombin (Orset et al., 2007), and photochemical generation of free radicals (and thus clot generation) via photo-excitation of Rose Bengal (Watson et al., 1985).

The methods described above are an example of the wide array of models available depending on the nature of the scientific question poised. Disadvantages of rodent models include the lack of white matter, the limited cognitive behaviors compared to humans and the lissencephalic nature of their brains in comparison to other mammals, including primates (Hollyer, 2016).

1.2 STEM CELL THERAPIES FOR STROKE

The brain has an intrinsic capability to regenerate through the process of neurogenesis - which is more occurring in animals compared to humans. Yet, this repair mechanism is not able to fully replace the tissue lost or damaged during massive necrosis, such in stroke conditions (Hermann et al., 2014). There is evidence that neuronal replacement in the human brain can take place in Parkinson disease, as shown by Lindvall and Bjorklund, 2004. However, stroke is a much more complex pathology and the fact that improvement could be achieved with neuronal replacement still remains a challenge. Many research groups around the world are picking up the challenge and are trying different experimental strategies to achieve such goal. A much explored strategy is the introduction of external stem and precursor cells, due to the fact that they can survive, differentiate into neurons, and partially restore function after transplantation in the stroke-damaged rodent brain (Daadi et al., 2008).

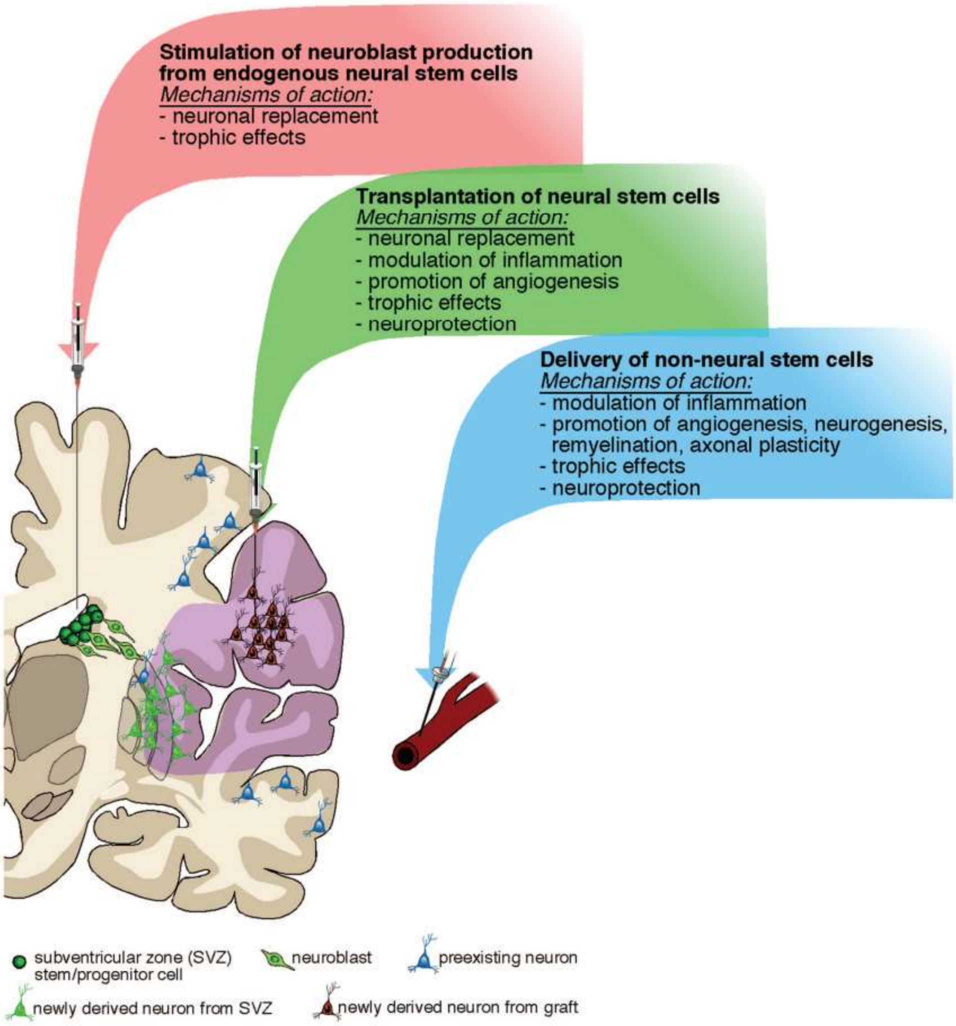

Figure 1.2. Stem cell based approaches for stroke therapy. Apart from the proposed transplantation of NSCs, the stimulation of endogenous neuroblast production and the delivery of non-neural stem cells are two proposed mechanisms thought to exert benefits over the restoration of normal brain function after stroke. From Kokaia and Lindvall 2011.

Upon cell transplantation into the brain, they differentiate in situ to integrate into the host tissue by developing synaptic processes and acquiring local phenotypes. Full functional integration to replace dead tissue has not been observed yet in the case of stroke, where a complete assimilation of tissue is needed to restore impaired cognitive and motor functions (Lindvall and Kokaia 2011). However, it has been shown that grafts can also benefit the ischemic environment via trophic factors, neuroprotection and immunomodulation (Bjorklund and Lindvall, 2000).

Several technologies have been developed to generate neural precursors to be integrated into brain tissue. In particular, fetal neural tissue, embryonic stem cells (ESCs) and induced pluripotent stem cells (iPSCs) can be derived into neuronal precursors (Kim and de Vellis, 2009). They can divide via mitosis and differentiate into all cells of neuronal lineage, namely neurons, astrocytes and oligodendrocytes. They are less likely to form teratoma than pluripotent stem cells and they can be stimulated *in vitro* with cytokines to drive their differentiation fate *in vivo*, in an attempt to improve therapeutic effectiveness (Kim and de Vellis 2009). Another advantage resides in the fact that they promote neurological recovery via indirect mechanisms that involve the stimulation of endogenous angioneurogenesis and neural plasticity, stabilization of the blood brain-barrier as well as modulation of peripheral and central immune responses (Doeppner et al., 2012, Hermann and Chopp 2012, Mora-Lee et al., 2012, Zhang and Chopp 2013). Neurorestaurative treatment paradigms using neural stem cells against stroke have not found their way into the clinic yet, however, proof-of-concept studies evaluating mesenchymal stem cell transplantation in human stroke patients achieved promising data, which justifies more systematic studies (Uccelli et al., 2008, Lee et al., 2010, Honmou et al., 2011). Nevertheless, there is some controversy with this method as Detante and colleagues showed that labelled human MSCs did not cross into the brain already one week after MCAO (Detante et al., 2009).

Other investigations have focused on the chronic post-stroke period (Barbosa da Fonseca et al., 2010; Bhasin et al., 2011). At this stage, the majority of dead tissue has been removed with the infarct replaced by a CSF filled cyst, inflammation is reduced, and surviving tissue plasticity mechanisms are under way. Implantation of stem cells at this stage may therefore enhance the plastic compensatory approaches. Using neural stem cells (which have a more direct lineage to NSCs cells compared to MSCs) seems a rational choice.

However, this provides unique challenges in the sourcing and administration of such cells whereas autologous mesenchymal stem cells are far easier to isolate. Despite these challenges, both neural and mesenchymal stem cells are currently in clinical trials. Steinberg and colleagues recently published the results of a Phase 1/2a clinical trial of allogenic bone marrow mesenchymal stem cells transfected with a Notch1 intracellular domain (Steinberg et al., 2016), which has a role in stem cell differentiation into neurons and glia (Lundkvist and Lendahl, 2001; Dezawa et al., 2004). The study demonstrated that intracerebral implantation of the cell line into the peri-infarct area, on average 22 months post stroke, lead to a mean decrease in NIHSS scores of 2 and a mean increase in the Fugl-Meyer motor function of 11.4% with no serious adverse effects of transplantation. However, caution in interpretation is advised due to the uncontrolled study design which was also not powered to detect improvements in clinical scores (Hollyer, 2016).

1.3 NONINVASIVE IMAGING TOOLS

In longitudinal experiments there is a need to follow up the event taking place inside of the subject without having to sacrifice it or expose it to invasive imaging techniques that could alter the development of the changes happening in the place of interest. Some critical steps have only been resolved with traditional experimental methods or sacrificing high number of animals at different time points. Using noninvasive imaging strategies it is possible to investigate the whole physiological or pathological process while the organism remains alive, and also hold the advantage of only mildly affecting the physiological homeostasis of the subject (i. e. by anesthesia administration, or an injection with substrate). This thesis employs two noninvasive imaging techniques, bioluminescence (BLI) and magnetic resonance imaging (MRI) for the investigation of changes after ischemic onset and after cell implantation in the healthy or the lesioned brain.

1.3.1 Bioluminescence imaging

1.3.1.1 Imaging principles

BLI imaging consists in the detection of light to visualize cellular and molecular processes. Such photons are generated through an enzymatic reaction, in this thesis project I used luciferase as the enzyme and luciferin as the specific substrate. Different luciferases have been isolated over the last years, all of them entailing specific substrates, wavelengths and cofactors (Vogel et al., 2017). In particular, I used the luciferase isolated from the firefly photinus pyralis, which emits photons at a wavelength between 530 – 640 nm with a peak at 562 nm (Sadikot and Blackwell, 2005). This enzyme catalyz-

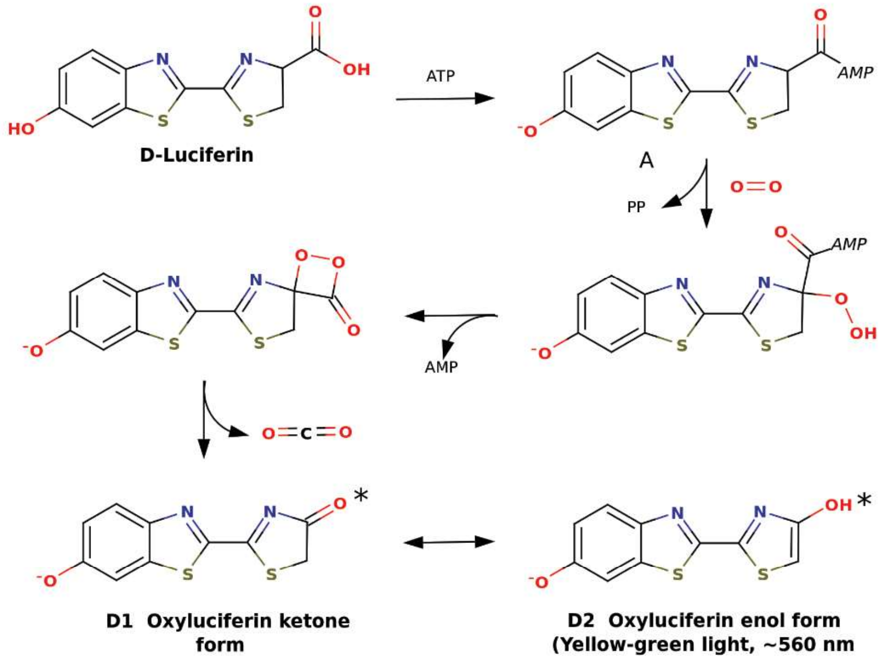

Figure 1.3. ATP-dependent BLI reaction catalyzed by the firefly luciferase. The cofactor Mg^{+2} must be present for the reaction to happen (not depicted). Following the formation of the enzyme-bound luciferyl adenylate, a proton is abstracted from the C-4 carbon of the adenylate by a basic side chain amino acid residue of luciferase. Next, molecular oxygen adds to the newly formed anion and an electronically excited state oxyluciferin molecule and carbon dioxide are produced from a highly reactive dioxetanone intermediate (not detailed). Red light emission (λmax 615 nm), which is observed at pH 6.0, results from the keto form of the emitter. At pH 8, the familiar yellow-green light emission (λmax 560 nm) is produced from the enolate dianion form of the excited state oxyluciferin by a presumed enzymatically assisted tautomerization (Branchini 2013).

es the substrate D-luciferin specifically in a two-step chemical reaction that requires ATP and Magnesium as a cofactor. Since the substrate is a light and small molecule, it diffuses fast and crosses the blood brain-barrier (James and Gambhir, 2012). Because the reaction is an oxidation, it must take place in an environment where O_2 is available. Figure 1.3 depicts the complete chemical reaction for the production of photons.

1.3.1.2 BLI applications in pre-clinical research

To make use of the above mentioned reaction, the cells must be able to stably express the luciferase enzyme. By locating the gene downstream to a maturation-specific promoter, it is possible to follow the maturation process of the cell that expresses the enzyme (Tennstaedt et al., 2015). The gene can also be placed downstream of a constitutive promoter so that the activity of the enzyme reflects the viability of the cell as long as it is located in an oxygenated environment. Signal intensity is mainly dependent on substrate concentration, route of injection, type and dosage of anesthesia. I followed the protocol established and improved by our colleagues (Aswendt et al., 2013). The photon emission peaks at around 10-12 minutes after i.p. administration of the substrate, but it is possible to observe subjects with an earlier or later peak.

The photons produced as a result of the chemical reaction are detected by a highly sensitive charge-coupled device (CCD) camera attached to a light chamber in an imaging system. The CCD camera spatially encodes the intensity of acquired photons into an electrical signal to generate an image (Figure 1.4). Noise of the system is reduced by active cooling of the camera and tight closure of the animal receptacle, removing any light reflecting object.

One of the most important advantages of the method – compared to fluorescent measurements – is the lack of excitation from a light source, which leads to photo bleaching of the tissue. It is a method simple to use, processes can be monitored over a long period of time as long as the enzyme is being expressed and multiple measurements can be performed on the same subject, which reduces the amount of animals needed. BLI offers high signal specificity and sensitivity, however, it is limited in spatial resolution due to tissue-induced light scattering. Assuming sufficient access to substrate and cofactors, there is a linear correlation between photon emission and enzyme concentration and therefore quantification both *in vitro* and *in vivo* is possible (Berger et al., 2008).

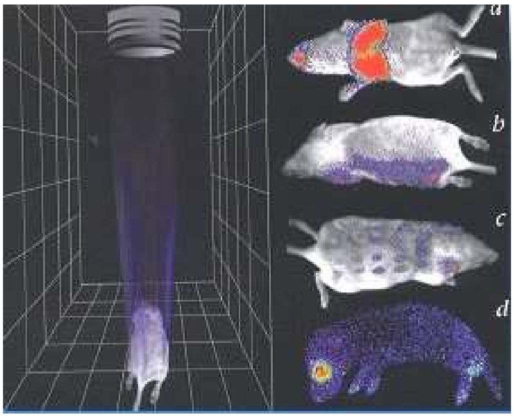

Figure 1.4: *In vivo* monitoring of luciferase-produced photons in mice. The diagram on the left is a representation of the bioluminescence imaging device showing the lens that focuses light from the animal into the CCD detector. On the right, the pseudocolor images indicate light intensity (red most and blue least intense). Adapted from Contag et al., 1998.

Among the disadvantages of the method lies the light absorption by tissue chromophores such as hemoglobin and melanin, and the light scattering, which limits detection in deep tissues. Only photons at 600 nm and above can penetrate the tissue, the interaction with the tissue produces scattering which decreases the spatial resolution to a mm scale. At two centimeters of depth, one million of luciferase expressing cells are necessary to produce the same signal as a few hundred cells in the subcutaneous tissue (Rice et al., 2001). I.p. administration of the substrate could result in bowel injections if the scientist is unexperienced.

In conclusion, BLI is a powerful tool for longitudinal noninvasive *in vivo* imaging of small animals and the experimental setup of each protocol must be evaluated for the application of need.

1.3.2 Magnetic resonance imaging

Nuclear Magnetic Resonance (NMR) is the phenomenon whereby nuclei with a spin align with an external magnetic field and precess, creating a net magnetization M_0 (given by the average of all angular momenta).

1.3.2.1 Imaging principles

The hydrogen nucleus is commonly used in clinical research because of its abundance in organisms. The intrinsic angular momentum of subatomic particles, such as the proton, is called 'spin', they align parallel or antiparallel when introduced in the magnetic field B_0 along the field directions, resulting in a net sum magnetization M_Z that is parallel to B_0. (Figure 1.5). The proton spins precess around the axis M_Z with a special frequency (ω), which depends on the external magnetic field strength (B_0) and on a nucleus dependent constant (the gyromagnetic radio, γ), and is termed "Larmor frequency". $\omega = \gamma B_0$

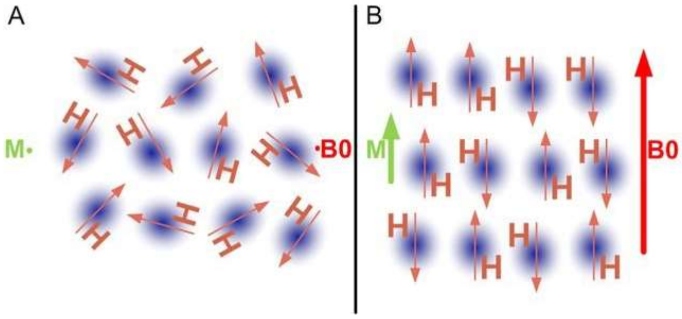

Figure 1.5: Protons in a magnetic field. In the absence of a magnetic field (left) the spins are oriented randomly. Upon placement in a magnetic field (right) with magnetic strength B0, they align with the field and precess around the B0 axis. Adapted from Burns 2014.

When protons are excited by a radiofrequency (RF) or excitation pulse of matching Larmor frequency i.e. resonance frequency, the net magnetization is tilted from along the B_0 axis (or z-axis) into the xy-plane, thereby inducing phase coherence among the nuclei. The new transverse magnetization M_T continues to precess around the M_Z axis and induces a current in a conductive coil, which represents the MR signal. When the radiofrequency pulse is ended, the M_T magnetization will gradually disappear by a process called relaxation, until the proton spins reach their equilibrium in realigning with the external field M_Z. The relaxation can be divided into two distinct components: the transverse relaxation and the longitudinal relaxation. The first describes the decay of the transverse component of the magnetization and is called free induction decay (FID), which follows a time constant termed T2* relaxation time. A refocusing pulse reverses the impact of external magnetic field inhomogeneities on the signal by generating an echo for signal detection. The amplitude of the echoes decays with a tissue specific time constant called T2 relaxation. The longitudinal component of the net magnetization recovers with a tissue specific time constant T1 until the equilibrium of spin alignment with the external magnetic field is reached (Figure 1.6).

These relaxation processes can be used for contrast generation between different types of tissue. Variation of the major parameters of repetition time (TR) and echo time (TE) can create images with enhanced contrast. Different tissues have different chemical compositions and structural components where the behavior of proton spins varies. Fat protons are within large triglyceride structures surrounded by electroneutral carbon atoms compared to the more exposed protons of water molecules. The difference in relaxation times is able to even distinguish between subtle differences such as between gray and white matter. Depending on the compared tissue, either T1 or T2 results in the best contrast. By applying short TRs and short TEs,

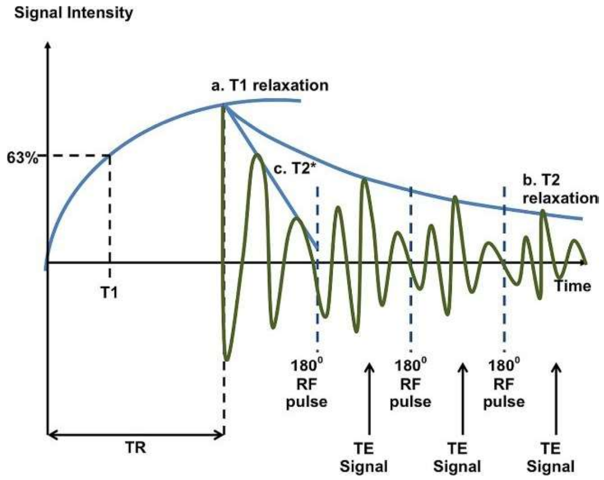

Figure 1.6: T1, T2 and T2* relaxation. A) T1 curve: Plotting the recovery of longitudinal magnetization over time following the switching-off of a radiofrequency (RF) pulse results in a T1 curve. B) T2 curve: An 180° refocusing pulse acts to 'combat' the effects of external magnetic field inhomogeneity by rephasing the protons. This results in a temporary gain in signal intensity at echo time (TE) termed spin echo. A sequence of 180° pulses results in a chain of spin echoes. Each subsequent echo will be of lower intensity due to T2 effects. A curve connecting the spin echo intensities is the T2 curve. C) T2* curve: This curve results when 180° refocusing pulses are not used. The signal decays much faster due to T2* effects. TR, repetition time. Extracted from Currie et al., 2013.

the T2 relaxation effects are minimized and therefore allow for differentiation of structures based on their T1 values. Longer TEs and TRs reduce T1 relaxation effects and allow for T2 contrast (Figure 1.7).

The Signal-to-noise ratio (SNR) of MRI data is determined by several variables including: hardware properties, proton density, voxel volume, receiver bandwidth, T1, T2, flip angle, TE, TR to name a few. Optimization of these variables will improve SNR, and thus image quality.

Pulse sequences describe the manner in which RF pulses and gradients are applied which in turn determines the signal measured and the resultant images. Diverse sequences have been developed which permit investigations into various macro- and micro-structural properties of tissues but also the metabolic and functional behaviors within all organs including the brain.

- Spin-echo sequences: A Spin-Echo (SE) sequence applies a 90^0 excitation pulse, flipping the magnetization vector into the orthogonal plane. Due to the T2* effect, spins begin to dephase. Application of a 180^0 pulse will cause the spins to precess in the opposite direction, and to become in phase again. Spin re-phasing eliminates B_0 effects resulting in a T2 weighted echo (Hahn, 1950). The TR and TE of the spin echo sequence will determine the contrast of the image as described above.

- Gradient-echo sequences: Gradient echo/Gradient recalled echo (GRE) sequences were developed to decrease scan time. A short TR and small flip angle (less than 90^0) are used with an echo generated via gradient reversal. The TE used and thus the resultant signal will determine the amount of T2* weighting. However, because of this, GRE images are confounded by a lower SNR compared to SE sequences with similar parameters.
- Echo-planar imaging: Echo-planar imaging (EPI) sequences are very rapid acquisitions whereby k-space is filled following a single RF excitation pulse by rapid switching of the frequency and phase encoding gradients. Multi-shot EPI uses multiple excitations to fill k-space, increasing acquisition time but reducing susceptibility artefacts. EPI image contrast is determined by the TE when the phase encoding gradient is zero (Hollyer, 2016).

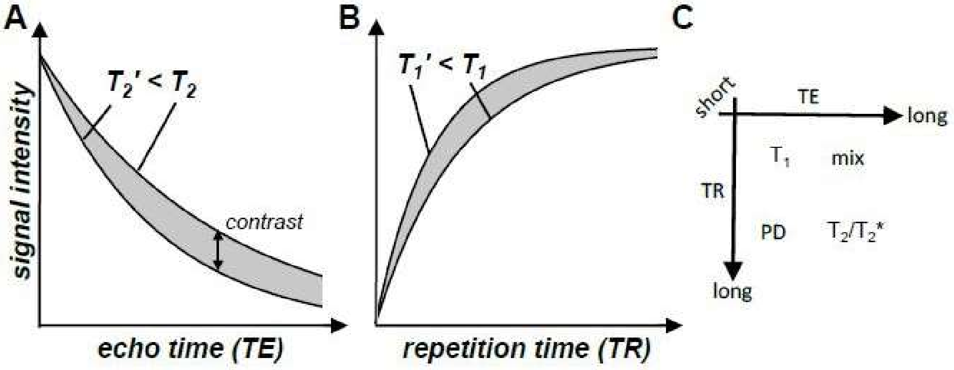

Figure 1.7: Formation of contrasts through variation of imaging parameters. A) Tissues with different T2 yield different signal intensities depending on the choice of TE. B) Signal intensity is limited by the available longitudinal magnetization. Its regrowth after an excitation is determined by T1 thus leading to a TR dependent contrast for tissues with different T1. C) The choice of TE and TR determines the gross contrast of an MRI image to be proton density (PD), T1, T2 (or T2* in case of gradient echo) or mixed weighted. Extracted from Kalthoff, 2012.

1.3.2.2 The BOLD signal

One of the stable methods to investigate brain function during activation and rest, the Blood Oxygenation Level Dependent (BOLD) signal is a reflection of a complex integration of cerebral blood flow, blood volume, and metabolic events in response to neuronal activation. BOLD data are often presented as ‘activated’ voxels overlaid on anatomical maps to reflect spatiotemporal signal changes of statistical significance. The mammalian brain is highly metabolically active, consuming 20% of the body’s energy at rest (Mangia et al., 2008). The majority of ATP use is devoted to maintaining the cellular ionic gradients required for signal propagation and synaptic transmission. Functional hyperemia is the phenomenon of the increase in blood flow in response to neuronal activation. The mechanisms by which functional hyperemia is induced are multifaceted, further complicated by the varying distributions of energy consumption throughout different regions of the brain. Energy use within the cerebral cortex is distributed between synaptic transmission, housekeeping (non-signaling tasks), action potentials, and maintaining resting potentials estimated at 44, 25, 16, and 15 percent, respectively (Howarth et al., 2012). Flow-metabolism coupling evolved to ensure active neurons and glia receive adequate blood supply to maintain normal function. We are now aware of a multitude of molecular signals which work in concert to direct flow at the macro- and microscopic level to ensure that active regions are supplied with sufficient oxygen and glucose to function. These include glutamate, lactate, oxygen, etc. (Attwell et al., 2010). As a result, we are also beginning to unravel potential mechanisms by which flow-metabolism coupling dysfunction may occur, contributing to disease onset or pathology.

Prior to the early 1980s, it was conventionally believed that the blood flow response to neural activity was driven by metabolic demand in a linear fashion (Roy and Sherrington, 1890). However, measurements of cerebral blood flow (CBF), and oxygen extraction fraction (OEF) via Positron Emission Tomography (PET) imaging, using 15O labelled water and molecular oxygen, respectively, showed that the blood flow response to somatosensory stimulation exceeded metabolic rate by nearly 6-fold (Fox and Raichle, 1986). The term functional hyperemia was coined to describe how activity at the cellular level within the brain is coupled with disproportionate increase in local blood flow.

The brain has a relatively constant oxygen extraction fraction (OEF) of 40% from the blood at rest (Gusnard and Raichle, 2001). During activation, however, feed-forward mechanisms increase CBF to anticipate the increased demand for oxygen and glucose. For example, stimulation of the human V1 area results in a 15% increase in energy demand with a 60% increase in CBF (Lin et al., 2010). Consequently, functional hyperemia causes a reduction in the OEF; the fundamental basis of the BOLD signal. For increasing metabolic demand, the oxygen gradient between blood and the tissues must be increased either by increasing capillary pO2 or decreasing mitochondrial pO2.

Deoxyhemoglobin is paramagnetic and the degree of magnetization (susceptibility) of blood changes as a linear function of oxygenation (Weisskoff and Kiihne, 1992). Deoxygenated blood has a greater susceptibility compared to its oxygenated counterpart which is diamagnetic (zero susceptibility) causing local field inhomogeneities within erythrocytes, the lumen contents, and surrounding tissues; shortening the net T2 in the voxel. One may initially believe that as a result of neural activity, the T2 signal would decrease further as oxygen is extracted. However, as described above, functional hyperemia causes a surplus of oxygenated blood to be delivered to the region of activation thereby decreasing the concentration of paramagnetic deoxyhemoglobin within the vessel lumen. The contrast changes within the vessels of the hyper-/hypoxic rodent brain were first identified via a gradient echo pulse sequence at 7T (Ogawa et al., 1990). Comparisons between contrast during carbon monoxide inhalation and hypoxia, inferred that the contrast changes were generated by susceptibility differences between intravascular deoxyhemoglobin and the surrounding tissues (Figure 1.8). Hence, the hypothesis that MRI could be utilized to investigate activity in the brain was proposed.

The cortical BOLD signal represents regional inputs and processing in the voxel of excitatory neurons as well a inhibitory interneurons. Excitatory inputs are either intrinsic signals from within the cortex or thalamo-cortical afferents to pyramidal cells whereas inhibitory connections are short and local, possibly tuning the projecting neural outputs (Logothetis, 2003). The resultant BOLD signal changes as a consequence of functional hyperemia are typically weak, within 1-2% (greater at higher field strengths). As such, a substantial degree of image pre- and post-processing is required to detect changes in brain activity (see below).

Most BOLD experiments are conducted using a GRE-EPI sequence. However, the signal is often mislocalised due to the draining of deoxyhemoglobin-rich blood into pial vessels and surface veins (Disbrow et al., 2000). Spin-echo (SE) sequences, as described earlier, eliminate T2 decay and can improve the spatial specificity of the BOLD signal to the parenchyma (Goense et al., 2007).

A large number of functional imaging studies have been conducted in non-human primates. They are a preferable model for fMRI investigations compared to rodents due to their larger brain size, greater grey-to-white matter ratio, more homologous brain structure to humans, and their ability to be trained for conscious experiments for long periods of time. However, due to cost and low public approval, their use is limited to a few specialized centers. As a result, functional imaging studies in rodents have increased in popularity. Although it is possible to train rodents to remain still within an MRI scanner (Liang et al., 2015), anesthesia or sedation is preferred with various tested compounds, each with their own strengths and caveats for BOLD imaging (Hollyer, 2016).

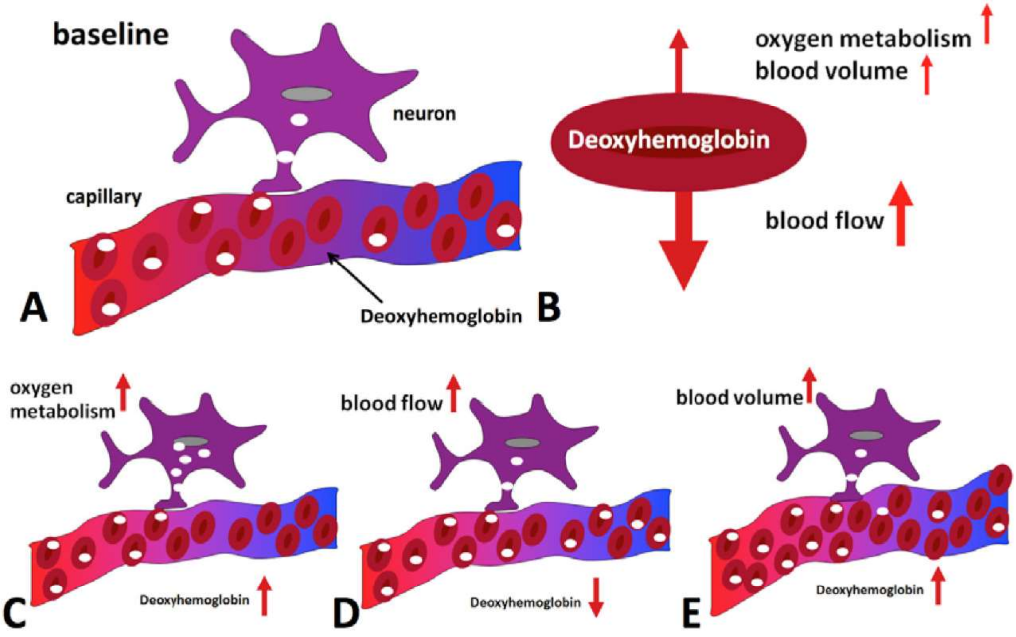

Figure 1.8: Hemodynamic effects contributing to the BOLD signal during activation. A) situation in the baseline state, with only some of the delivered oxygen being utilized. The diagrams at the bottom illustrate the effect of C) oxygen metabolism, D) blood flow and E) blood volume increases on deoxyhemoglobin concentration. B) Blood flow increase dominates, leading to a net reduction of deoxyhemoglobin and an increase in MR signal is hence observed. From Barth and Poser, 2011.

1.3.2.3 The BOLD signal in the resting state

Great focus has been applied to understanding the mechanisms underpinning the intrinsic activity of the resting brain. PET, and later BOLD imaging, where the subject was invited to remain at 'rest' during imaging, showed that brain activity occupied a specific network known as the Default Mode Network whose activity reduced during task driven activations (Raichle et al., 2001). Resting BOLD signal fluctuations in bandwidths previously considered as noise (< 0.1 Hz) were first identified by Biswal across the human sensorimotor network (Biswal et al., 1995). Additional resting cortical networks have subsequently been identified. Leopold and colleagues identified low frequency fluctuations in the local field power in the macaque visual cortex with high coherence between electrodes over 20mm apart (Leopold et al., 2003). He and colleagues showed, using electrocorticography in humans, that slow cortical potentials correlated with spontaneous BOLD fluctuations in several states (He et al., 2006).

1.3.2.4 Data pre-processing

Pre-processing of raw functional data is an essential component of all functional MRI data analysis. In statistical terms, noise is the variable that does not fit the model, so by managing the variance through several pre-processing steps, the power of the data is increased (Hollyer, 2016).

- Motion correction: Slight motion or rotation can lead to misalignment of voxels. Most correction methods use rigid-body registration, which corrects for motion along three translational dimensions and three rotations. A large series of functional images (repetitions) are acquired for resting state fMRI. One volume, usually the first volume of the series, is used as a reference for the registration of all the volumes of the functional series (Kalthoff, 2012).
- Coregistration: Coregistration to a well-recognized anatomical atlas with distinct structural delineations improves the spatial localization of the regions of the brain involved in resting-state networks. The most popular coregistration method (the above-mentined rigid-body transformation) is based on mutual information which aims to maximize the association between grouped voxel intensities (Collignon et al., 1995).

- Spatial smoothing: Spatial smoothing replaces a voxel value at each TR by a weighted average of its neighbors by the full weight at half maximum kernel. As such, high frequency noise over small areas is removed and by doing so, increases the SNR. The data also become more normally distributed and therefore more rigorously fit to the statistical tests used in functional MRI analyses (Ashby, 2011).
- Temporal filtering: Temporal filtering smoothes voxel data across the time series, removing signal beyond certain frequency, considered as noise.
- Field-mapping and distortion correction: Echo planar imaging (EPI) is highly susceptible to geometric distortion due to B0 inhomogeneities caused by sources such as the air within the ear canals, hemorrhages within the parenchyma, or implanted devices. These sources of susceptibility cause the greatest distortion in the phase direction due to the smaller bandwidth. As such, inhomogeneities cause shifts in voxel position, altering the shape of the brain. Distortion (often dissimilar between subjects) complicates EPI image intra-subject co-registration as well as co-registration to standard atlases. Field-mapping is a direct measurement of the inhomogeneities within a subject and is calculated by acquiring two 3D gradient echo images at different echo-times, calculating the phase difference between them, and dividing it by the difference in TE. A voxel displacement map is calculated and the EPI volume subsequently unwarped (Jezzard and Balaban, 1995).

1.3.2.5 Measuring anisotropic diffusion with MRI

Diffusion MRI is a unique imaging technique that is based on the inherent property of water particles to diffuse in a medium and enables to visualize microstructural properties with a macroscopic imaging technique. It allows reconstructing the neural pathways of signaling in the brain. The image contrast provided by diffusion MRI is based on the path of diffusing spins (e.g hydrogen in water molecules) over time and thus gives information about the underlying brain architecture.

Water molecules in tissue are rarely free to diffuse. They diffuse along tissue boundaries, such as membranes and are therefore either hindered or completely restricted in their diffusion direction. In order to visualize the connectivity of the brain with diffusion, we are interested in modeling axonal bundles, also called fibers. Water molecules can relatively freely diffuse along an axon, but are constrained in all perpendicular directions. The myelin sheaths of the axons thereby determine the degree of constraint. Fully myelinated axons restrict the water molecule along the axon, whereas non-myelinated or partially myelinated axons pose only a hindrance of diffusion. However, the diffusion coefficient is only defined for a single value (scalar) and is not able to describe the gradient dependent, different diffusion behavior in three dimensions.

The most common index for quantifying the degree of anisotropy is the fractional anisotropy (FA). The FA value is calculated for each fiber population. It is not my intention to describe all the characteristics of Diffusion MRI imaging, including fiber tracking or Q-Ball imaging, since I only made use of a tool to calculate FA in defined ROIs.

2

Chapter 2

Materials and methods

2.1 Animal handling

Homozygous male NMRI-Fox1^{nu}/Fox-1^{nu} mice with Tyr^{c} albino background were used for all experiments. The autosomal recessive mutation in the Foxn1 gene (chromosome 11) causes thymic aplasia, which results in immunodeficiency. As a consequence, there is a lack of T cells, B cells remain, which makes this strain ideal to host allograft implants. This mutation also leads to a keratinization defect of the hair follicles and the epidermis, the mouse has transient downy hair (www.janvier-labs.com). Therefore, these mice are colloquially named "nude" mice, which is the term that is used in this thesis. Mice were purchased from Janvier Labs (Le Genest-Saint-Isle, France) and housed under a 12:12 hours light:darkness cycle, resting in quarantine for one week after arrival. Mice had access to food and water *ad libitum* and 3-4 individuals shared the same cage for the purpose of social housing. At the first week of the longitudinal experiment, mice were 8 weeks old and weighted 30 ± 2 grams.

All animal experiments were conducted in accordance with the German Animal Welfare Act guidelines and approved by the local authorities from LANUV (Landesamt für Natur, Umwelt und Verbraucherschutz Nordrhein Westfalen). The animal permission was approved under the number 84-02.04.2014.A370.

2.2 Bioluminescence Imaging (BLI)

In order to determine the viability and to control for proliferation or extinction of cells, the photon emission of the transgenic graft was recorded with an IVIS SPECTRUM CT (Perkin Elmer, Waltham, MA, USA).

D-Luciferin 50 mg/ml solutions were prepared diluting the powder contained in one vial of D-Luciferin sodium salt purchased from Synchem (Felsberg, Germany) into 20 ml of Dulbecco's phosphate-buffered saline (PBS, Life Technologies). Solutions were filtered sterile prior to use and stored at -20°C. Before *in vivo* measurements, aliquots were thawed and kept to reach room temperature before injecting the animal. Animals were injected peritoneally with 300 mg/kg dose of D-Luciferin. After injection, anesthesia was immediately induced with a mixture of 2% Isoflurane in 70:30 N_2O:O_2 atmosphere. When no longer conscious, animals were immediately placed inside the Photon Imager IVIS SPECTRUM CT under the same gas mixture conditions of anesthesia. The time lag between substrate injection and beginning of image acquisition was kept constant at 3 minutes. The image acquisition protocol included one photon emission measurement every 2 minutes, recorded for 30 minutes (Tennstaedt et al., 2015)

In vivo BLI data was analyzed using the Living Image Software® (Perkin Elmer, Waltham, MA, USA). In short, the photon emission signal was color coded according to magnitude, and overlaid to a black and white photographic image of the field of view containing the animal, and a tritium standard to control for signal variation in photo detection. The dynamics of photo emission was plotted to ensure that the maximum photo emission fell within the 30 minutes window. When such condition was not met, the animal's measurement was repeated within the same week. The total flux was measured in photons/second at the moment of maximum emission within a circular ROI delimited over the head of the mouse. The size and location of the ROI was preserved in subsequent measurements for all animals.

2.3 Electrocoagulation model for distal middle cerebral artery occlusion

The mouse was placed into an induction chamber with an isoflurane concentration of 4% in an atmosphere of 70:30% $N_2O:O_2$. When its movements stopped, the animal was placed on a warm plate to keep his temperature stable during surgery, with the aid of a rectal temperature probe. Caprofen (Rymadil) diluted 1:100 in saline was injected to induce analgesia, in a dose of 4 mg/kg. The mouse's head was placed laterally in the anesthesia mask and isoflurane concentration was lowered to 2%, monitoring that the breathing rate was above 80 bpm at all times. Dexpanthenol eye ointment was applied on both eyes to preserve them from drying. After checking for pain reflexes, the skin on the right side of the head was sterilized and a 1 cm incision was made between the ear and the eye. The skin was pushed to the side and the temporal muscle exposed. The electrocoagulation forceps at 12 W was used to detach the muscle from the skull in its apical and dorsal parts with the intention to make a flap to expose the bone. The skull was cleared from tissue and the MCA was identified though the translucent bone in the rostral part of the temporal area, rostral to the retro-orbital sinus (Figure 2.1). Some drops of saline were applied on the skull and the bone was drilled

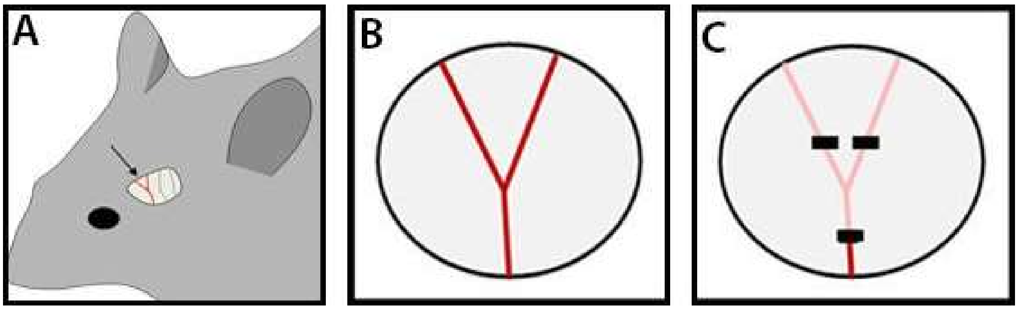

Figure 2.1: Transcranial view after removal of the temporal muscle and schematic view of MCA occlusion. (A) After removing the temporal muscle the cortical arteries can be viewed through the partially translucent mouse skull (in 8-12 week old mice). The dominant MCA branch can be identified in the rostral part of the temporal view as well as further cortical arteries branching from the MCA and the PCA in the caudal part. (B) Schematic view on the dominant MCA branch in its predominant variation with a bifurcation on the lateral temporal cortex after drilling a burr hole and removing the skull. (C) Black squares represent the MCA coagulation sites at the proximal and distal sides of the bifurcation (Llovera et al., 2014).

thin above the coagulation site. When the bone layer became transparent, the remaining bone sheet was removed manually with the help of a thin forceps. Once the artery was exposed, the electrocoagulation forceps was set to 7 Watts (bipolar) and the artery was coagulated from both sides without grasping it to avoid a rupture and subsequent hemorrhage. 30 seconds after coagulation, the artery was checked for reperfusion, in which case the electrocoagulation procedure was repeated until spontaneous recanalization was excluded. The temporal muscle was flapped back into its position, which covered the bone hole. The skin was sutured with silk thread and the stitches removed 3 days after surgery. Analgesia was maintained with Tramadol in drilling water ad libitum for the following 3 days.

For the sham operation, the same steps were followed. This time, the forceps tips were kept more separated from each other to make sure the artery was not coagulated.

2.4 CELL CULTURE, CLONING AND TRANSDUCTION

Human neural stem cells (hNSCs) (Thermo Fisher Scientific) were chosen because their use had already been well established in our lab as neural precursors to be transfected with a double construct (Tennstaedt et al., 2015). The line was initially derived from the NIH-approved human embryonic stem cell line H9 (WA09) (Zhang et al., 2001).

The cell culture was maintained under 37°C and 5% CO_2 according to the manufacturer's protocol (Life Technologies) and were cultured at a density of $5x10^4$ cells/cm^2 on a Geltrex matrix (Thermo Fisher Sceintific) in StemPro NSC SFM complete medium, consisting of KnockOut DMEM/F12 medium, 2mM GlutaMax, 20 ng/mL of basic fibroblast growth factor (bFGF) and epidermal growth factor (EFG), and 2% of StemPro Neural Supplement (Thermo Fisher Scientific). The cells were passaged every 3 days using StemPro Accutase (Thermo Fisher Sceintific) to maintain them in undifferentiated state.

The bioluminescence reporter firefly luciferase (Luc2) from *Photinus pyralis* (Promega) and the enhanced green fluorescent protein (eGFP) from *Aequorea victoria* were cloned into a lentiviral plasmid designed for multicistronic expression. The T2A peptide was used for self-cleaving. The construct was placed under regulation of the constitutive promoter Elongation Factor 1 Alpha (EF1α) to express eGFP and Luc2 throughout the entire life of the cell. The final plasmid for transduction was pCDH-EF1α-Luc2-T2A-eGFP.

A 3rd generation HIV-lentiviral vector expression system was used consisting of the pCDH plasmid containing viral genetic elements, and the packaging plasmids pPACKH1-GAG, pPACKH1-REV and pVSV-G providing the structural replication and integration proteins (System Biosciences). Pseudoviral particles were produced by transfection (Lipofectamine Plus, Life Technologies) of 293T cells with 2.25 mg pPACKH1 packaging plasmid mix and 1 mg target vector in Optimem (Life Technologies). The virus supernatant produced by the 293T cells was collected und subsequently used for lentiviral infection of the H9 hNSCs facilitated by addition of 8 mg/ml Polybrene (Sigma Aldrich). Transgene expressing cells were sorted via FACS for high or medium levels of GFP (10^3-10^4 counts, respectively $10^{2.5}$-10^3).

2.5 ELECTROPHYSIOLOGY MEASUREMENTS

All electrophysiology experiments were performed by Dr. Simon Hess, in the working group of Prof. Dr. Peter Kloppenburg, Biocenter, Cologne, Germany.

Experiments were performed on brain slices containing the implanted graft, 16 weeks after transplantation. Animals were anesthetized with halothane (Sigma Aldrich) and decapitated, the brain removed and the block of interest was cut out. The brain was cut coronally in slices of 300 um with a microtome (ThermoScientific) under carbogenated glycerol-based modified artificial cerebrospinal fluid at 4°C to prolong viability of neurons. The sections were transferred into such fluid and kept at 35°C for 20 minutes, then at room temperature for 30 minutes prior to the recordings in the recording chamber, were the slices were continuously perfused at a flow rate of 2 ml per minute. The graft was identified by its green fluorescence using a fixed-stage upright Olympus microscope with interference contrast and fluorescence optics.

Current-clamp recordings were performed with an EPC10 patch clamp amplifier (HEKA), data were sampled at 10 kHz and low-pass filtered at 2 kHz with a four-pole Bessel filter.

Perforated patch recordings were performed using protocols modified from Horn and Marty (Horn and Marty, 1988) and Akaike and Harata (Akaike and Harata, 1994). After completion of the test protocols, perforated-patch recordings were converted to the whole cell configuration and biocytin was allowed to diffuse into the cell for 3-5 minutes. Brain slices were fixed in Roti-Histofix overnight at 4°C and subsequently rinsed in PBS, incubated in PBS-based blocking solution and with DyLight 650 conjugated streptadivin. Finally, brain slices were cleared in xylene (Appliochem) and mounted in Permount (Fisher Scientific). The fluorescence images were captured with a confocal microscope (Carl Zeiss).

For a more detailed description of buffer compounds concentrations and washing or incubation steps, please refer to Tennstaedt et al., 2015, section Materials and Methods.

2.6 Cell transplantations

Mice were anesthetized with Isoflurane in 70:30% N_2O:O_2 and 4 mg/kg Caprofen was injected to induce analgesia. The animal was placed on a warming pad to keep its temperature stable at 37°C and the temperature was controlled with a rectal probe. The head was fixed in a stereotactic frame (Stoelting, Dublin, Ireland). An incision in the skin was made to expose the skull, and Bregma was localized. A single hole was drilled at the following coordinates relative to Bregma: AP +0.5 (in the right hemisphere); ML 1.8; DV 0.8 from the brain surface. The coordinates were modified from Oki et al., 2012, to fit our settings of cortical implantation next to the ischemic lesion location.

The homogenous cell suspensions were kept on ice during surgery and were injected into the brain using a NanoFil syringe for microinjection (World Precision Instruments, Sarasota, FL, USA) with a 33G needle using a micropump system with injection flow rate of 150 nl/min. A volume of 1 ul containing 150.000 cells was injected and the needle was kept in place for 5 minutes after injection, to allow decantation of cells in the injection canal and avoid cell withdrawal together with the retraction of the needle. The wound was closed with silk and the stitches were removed 3 days after surgery, right before the first BLI measurement. Analgesia was provided for 3 days with Tramadol in drilling water ad libitum.

2.7 Histology and Immunohistochemistry

Mice were perfused transcardially under Isoflurane anesthesia at 4% with 20 ml PBS followed by 20 ml PFA. The brain was extracted carefully with a surgical spatula and incubated overnight with 4% PFA at 4°C. Subsequently, the PFA was replaced by 30% sucrose solution, and the brain was incubated for 2 days at 4°C. On the third day, brains were frozen in a flash cryoconservation at -40°C and rapidly transferred into -80°C storage. Sections of 14 or 30 um were cut in the coronal plane in the cryostat (Leica) and stored at -20°C.

Before immunostaining, and depending on the antibodies to be used, tissues received different pretreatment. The following table contains details of the antibodies used, brand, concentration, pretreatment and emission wavelength.

Staining	Pre treatment	1st Antibody	2nd Antibody	Emission λ
DAPI	Applied together with the 2nd antibody at a concentrarion of 1:1000			461 (blue)
HuNu	Sodium citrate	Anti HuNu mouse 1:100, Millipore	Cy5 donkey anti mouse, 1:100 JIR 715.175.151	670 (red)
NeuN	Sodium citrare	Anti NeuN chicken 1:100, Synaptic System	Cy3 donkey anti chicken 1:100 JIR 703.165.155	570 (yellow)
GFAP	Acetone -20°C 20 min	Anti GFAP mouse, 1:200, Sigma	Cy5 donkey anti mouse, 1:200 JIR 715.175.151	670 (red)
eGFP	None	Anti GFP rabbit, 1:200, Invitrogen	Alexa fluor 488 donkey anti rabbit 1:200 A21206 Thermofischer	525 (green)
Iba1	Acetone 4°c 20 min	Anti Iba1 rabbit, 1:500, Wako	Cy3 donkey anti rabbit, 1:200 JIR 711.165.152	570 (yellow)

In short, glasses were washed 3x 3 minutes in PBS, and then placed in the pretreatment solutions if applicable. They were washed again 3x 3 min in PBS. Sections were delimited with PAP Pen to limit the surface of work. A pre-incubation followed for one hour, in a solution containing PBS, 0.25% Triton and 5% NDS. The first antibodies were diluted in the blocking solution (0,25% Triton-X / PBS + 5% NDS) overnight at 4 °C and washed away the following day in 3 steps of 3 minutes immersion in PBS. The secondary antibody was also diluted in blocking solution and incubated in a wet chamber at room temperature for 2 hours, and subsequently washed again 3x 5 minutes with PBS. Slides were shortly dipped in distilled water and the glasses were left to dry under the hood. PAP Pen was removed with Ethanol. They were mounted with the glue Cytoseal XYL and left overnight to dry.

We also made use of histochemistry Nissl staining. Tissue sections were rehydrated in subsequent solutions containing descending concentrations of Isopropanol until pure distilled water. See below for details of time and concentration. The tissue was placed in a solution containing cresyl violet and again washed in distilled water. Finally, the tissue was dehydrated and differentiated in ascending concentration solutions of Isopropanol and Roti-Histol, which is free of water. Tissue was covered with coverslips and Cytoseal XYL and left to dry overnight.

Protocols and solutions used for Nissl staining in this project:

Rehydration

100% Isopropanol I	1 min
100% Isopropanol II	1 min
96% Isopropanol	1 min
70% Isopropanol	5 min

Staining

Cresyl violet 1:5	30-40 sec
Destilled water	1 min

Dehydration and differentiation

50% Isopropanol	30 sec
70% Isopropanol	30 sec
96% Isopropanol	30 sec

Check intensity of colors under the microscope and continue accordingly

100% Isopropanol I	1 min
100% Isopropanol II	1 min
Roti-Histol I	5 min
Roti-Histol II	5 min

2.8 Lightsheet fluorescence microscopy

The clearing of the brain tissue and subsequent recording of microscopy images was performed in the group of Dr. Martin Schwartz (University Clinic Bonn, Germany). The tissue clearing (BABB method) is meticulously described in Dodt et al., 2007. Briefly, whole mouse brains stored in PBS were dehydrated at room temperature by incubation in organic solvents / water mixtures of increasing solvent concentrations (30%, 50%, 70%, 80% 96% and twice 100%), followed twice by clearing solution at the respective pH and temperature for 24 hours.

Optically cleared samples were fixed in a glass cuvette filled with clearing solution. eGFP fluorescence was collected through a bandpass filter at 503-537 nm. For microscope settings and file management settings, please refer to Schwarz et al., 2015.

2.9 BEHAVIORAL TESTS

2.9.1 MODIFIED NEUROLOGICAL DEFICIT SCORE (MNDS)

The mNDS has been described in Hamzei Taj et al., 2016. Refer to the table below for a detailed description of sensorimotor assessments and the corresponding points for each task. The test includes a set of sensorial, motor and reflexes evaluations in the way of muscle status, abnormal movement, tactile stimulus, proprioception, audible cues, on a scale of 0-16. Weight loss is also assessed. The points are calculated as detailed in the following table:

Modified Neurological Deficit Score	Points
General Health	1
Weight Loss	2
Less than 5%	0
Between 5% and 15%	1
Between 15% and 20%	2
Motor tests - Raising mouse by tail	3
Flexion of forelimb	1
Flexion of hindlimb	1
Head moved >10°to vertical axis within 30s	1
Placing mouse on floor	2
Normal walk	0
Inability to walk straight	1
Circling toward paretic side	2
Sensory tests	2
Proprioceptive test (deep sensation, pushing the paw against the table edge to stimulate limb muscles)	2
Reflexes absense	6
Pinna reflex (head shake when auditory meatus is touched	2
Whisker relfex (head shake when whiskers is slightly touched with cotton)	2
Startle reflex (motor response to a brief noise)	2
Maximum points	16

2.9.2 ROTAROD TEST

The set-up consists of a rotating cylinder of 3 cm of diameter where multiple mice (up to 4) can be tested simultaneously in separated compartments. The rod was located 30 cm above a platform, and the animal would walk on the rotating rod and try to remain on it to avoid falling down. Mice were evaluated for "latency to fall" in seconds in two stages of the experiment: before dMCAO and one week after ischemia, as suggested in Balkaya et al., 2013. The paradigm for the motor deficit assessment after stroke included a gradual acceleration followed by constant speed, as follows:

Time in seconds	Speed in rpm
0 to 10	Accelerating 0 to 10
11 to 30	Accelerating 10 to 20
31 to 50	Accelerating 20 to 30
51 to 80	constant on 30

2.9.3 ROTATING BEAM TEST

The apparatus consists of a rotating fiberglass beam of 120 cm of length and 13 mm of diameter, distances marked every 10 cm. The beam attaches to a motor that rotates and is located 60 cm above a table covered with bubble cushions. The test consists on placing the animal directly on the rotating beam next to the starting end and the animal is expected to start walking along the beam to avoid falling to the floor as a consequence of the beam rotation. On the other side of the beam there is an arrival platform where the mouse is expected to climb and rest from the task. Mice were pre-trained at 8, 6 and 4 days before surgery, and the latest record was set as baseline speed for comparison after stroke. On the "arrival" platform at the end of the beam, a food pellet was placed to motivate the mouse to walk forward and not turn back on its steps. The beam was set to rotate at 6 rpm on constant speed, the animal was placed on the departing end of the beam in motion and left to walk to the arrival end. The total time until the animal was safely located on the arrival platform was recorded. Rarely will an unimpaired mouse fall off the beam, they use the four limbs and the tail to keep their balance while moving forward on the beam (blue mouse in Figure 2.2). Under sensorial or motor impairment, many mice show slips of the hind paws that could lead to a fall (red mouse in Figure 2.2). In the case of a fall, the distance until the fall

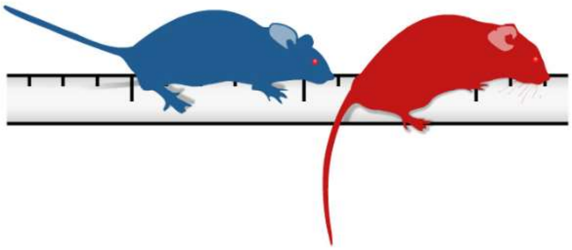

Figure 2.2: Schematic representation of two mice on the Rotating Beam. The blue mouse has no functional deficits and walks on the rod with full command of its four limbs. The red mouse entails a functional deficit on one side of the brain and slips to the side when walking on the rod. Sometimes the slip leads to a fall.

was recorded, and 60 seconds were added to the time it took to fall, therefore reflecting a poorer performance in speed.

Measurements after surgeries were obtained at 3, 7 and 14 days in the ischemic or sham occlusion groups. In the ischemia plus cell implanted group, further measurements were added to the previous ones, at 4, 6, 8 and 12 weeks after stroke. Results are expressed as a percentage of baseline speed at the timepoint of measurement, therefore each of the values after surgery is related to the same animal's baseline and only later averaged for the group.

2.9.4 Corner test

The testing apparatus consists of four connected varnished wooden walls placed in the shape of a diamond with 30 and 150 angles. Each wall measures 30 x 20 x 1 cm. As the animals enter the corner the whiskers are stimulated. The animals rear up and make a turn when they reach the end of the corner as graphically explained in Figure 2.3. Right and left turns are counted and compared for a side preference. In our particular setting, a small opening at the junction of the wall is left to motivate the mice to go deeper into the corner. The animal was carefully placed in the middle of the open space inside of the diamond-shaped area and left to explore the corners freely. At some point after entering the corner, the animal would rear and turn to either side. There was no time limit to record its moves, the first 10 successful turns after approaching the narrow corners were recorded and noted as “right turn” or “left turn”. Turns that were not part of a rear movement were discarded. A baseline measurement was done before induction of stroke to compare intra-animal tendency to turn to one or other side, hence the results were expressed as % of right turns and normalized to the baseline of each animal. Measurements were taken for the stroke and sham occluded group at 3, 7 and 14 days after stroke.

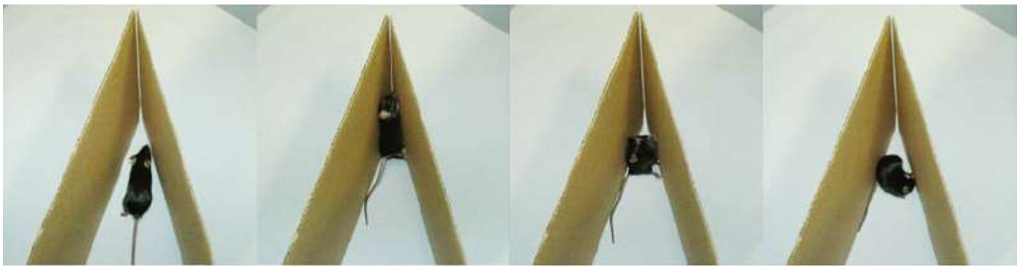

Figure 2.3: Corner test. Two boards are attached to each other at an angle of 30°. As the animals enter the corner the whiskers are stimulated. The animals rear up and make a turn when they reach the end of the corner. Right and left turns are counted and compared for a side preference.

2.10 MRI DATA ACQUISITION

MRI measurements were performed on a 9.4 Tesla animal scanner (Bruker Biospin, Ettlingen, Germany) with 20 cm horizontal bore diameter, equipped with actively shielded gradient coils with 600 mT/m. RF transmitting and signal receiving was acquired with a Helium-cooled mouse 1H quadrature cryogenic surface coil (CryoProbe, Bruker Biospin). The SNR increases compared to conventional surface coils, due to reduced thermal noise by the cooling of the coil to 20-35 Kelvin degrees. The manufacturer's software Paravision 6.1 (Bruker Biospin) was used to control the MRI acquisition protocols. The animal is placed in an acrylic animal holder equipped with a mask containing a teeth holder and breathing gases supply. The holder also includes ear bars to fixate the mouse's head, a thoracic breathing pad (SA instruments, NY, USA) to track the breathing movements, an optic fiber rectal probe (SA instruments, NY, USA) to monitor the animal's temperature and a water circulating system (Medres, Cologne, Germany) to adjust the animal's body temperature which was kept constant at 37 ± 1.0 °C.

DASYlab software (Measurement Computing, Norton, USA) was employed to monitor breathing rate and body temperature throughout the scan sessions. Anesthesia of the animal is induced in a "knock out box" in an Isoflurane enriched environment (70:30 N_2O:O_2, 4% Isoflurane), after which the animal is checked for pain reflexes and positioned in the acrylic holder, lowering Isoflurane concentration to 2%.

2.10.1 MRI ACQUISITION PROTOCOLS

A reference scan was acquired to confirm correct positioning of the mouse head. If the head was positioned in a tilted angle of up to 4 degrees in the coronal plane, or moved during positioning, or if the head was positioned too far away from the isocenter, then the animal was removed from the scanner and positioned again. The next scans were performed to set the reference gain for correct RF-pulse setting and to improve local field homogeneity through a local shim.

Next, a high-resolution anatomical T2 weighted TurboRARE sequence was acquired with a RARE factor of 8 and two averages. The field of view was set to 17.5 x 17.5 mm^2 and 48 slices of 0.3 mm thickness were placed to cover the whole mouse brain, the matrix dimension was set to 256 by 256, repetition time (TR) to 5,500 ms and echo time (TE) to 10.83 ms. A multi-slice multi-echo (MSME) sequence was measured for quantitative T2 imaging. MSME acquisition parameters were as following: TE = 11 ms, TR = 3,000 ms, number of echoes = 16, scan time of 6 min 24 sec, number of averages was 1, matrix size was 128 x 128, FOV of 18 x 18 mm^2, in-plane spatial resolution of (0.14 mm)^2, bandwidth of 50.000 Hz, slice thickness was 0.5 mm, number of slices was 11, coronal orientation, slice gap of 0.5 mm. T2 maps were calculated with an in-house developed procedure in IDL (Exelis Visual Information Solution, Boulder, CO, USA).

For resting state measurements, a gradient-echo echo-planar imaging (GRE-EPI) sequence was acquired using the following parameters: FOV 17.5 x 17.5 mm^2, matrix size 96 x 96, TR of 2,840 ms and TE of 18 ms. The scan was set up for 16 slices of 0.5 mm thickness placed over the forebrain in the coronal plane; placement of slices was done by adjusting the third slice on the rhinal fissure. 105 repetitions were acquired. To maintain functional activation during anesthesia while acquiring functional scans, we switched from Isoflurane anesthesia to Medetomidine sedation, adapting a protocol previously established by Grandjean and colleagues (Grandjean et al., 2014). We modified the dose of the drug to adjust for the sensitivity of the nude mouse strain. In short, a bolus containing 0.1 mg/kg of medetomidine hydrochloride (Domitor™, Pfizer, Berlin, Germany) in 250 uL of saline solution was injected by means of a line while the mouse is in the carrier inside of the scanner. The breathing rate starts descending as a consequence of the drug effect, concomitantly the Isoflurane levels were gradually lowered to 0% to avoid a respiratory arrest. The breathing rate was continuously monitored so that it would stay 90 and 130 rpm – else the animal was taken out of the scanner due to a risk of respiratory arrest or waking up respectively -, the body temperature was externally adjusted to be kept at 37 C. 10 minutes after

Isoflurane levels had been shut down, the functional scan was allowed to start, to ensure the minimum amount of residual Isoflurane in the animal's system. After the scan was finished, the animal was taken out of the holder and injected with an antagonist of medetomidine, atipamezol hydrochloride (Antisedan™, Pfizer, berlin, Germany), 0.1 mg/kg in a bolus of 250 uL of saline, to restore a normal breathing pattern and thermic regulation.

To acquire diffusion data, I followed a protocol established in our laboratory by Dr. Claudia Green, who thoroughly documented it in her dissertation (Green, 2017). 8 separate scans with 126 diffusion encoding gradient directions were acquired, distributed on a upper half sphere in q-space and a constant b-value of 2000 s/mm^2, each preluded by a non-diffusion weighted image to aid data processing. Software tools were implemented in custom-written Python scripts with additional bash scripts that enable batch processing. The acquisition details of the scans were the following: FOV 17.5 x 17.5 mm^2, 16 slices of 0.5 mm thickness, TR 3,500 ms, TE 20 ms, matrix dimension was set to 128 x 128, bandwith of 40.000 Hz, coronal orientation, no slice gap, in-plane spatial resolution of (0.14 mm)^2.

2.11 MRI DATA PROCESSING

Interactive Data Language (IDL 6.4, ITT visual information solutions, Boulder, CO, USA), Python 2.7.6, Matlab R2014b, Linux Ubuntu 16.04 LTS shell scrips were programming languages. FMRIB Software Library (FSL 5.0.9) and Advanced Normalization Tools (ANTS 2.1.0), DSI Studio 20170214, ImageJ 1.48s with macros (scripting language) and plugins (Java 1.6) were tools used to process the MRI data. All images acquired with Paravision 6.1 software were first converted to Nifti format and scaled up by a factor of 10 on each dimension to be able to be processed in software developed for human brain studies e.g FSL bet.

2.11.1 PROCESSING OF RSFMRI DATA

Images were averaged and in the mean image the brain extracted with FSL-BET. The mask resulting of the brain extraction was applied to the single functional images, which were motion corrected with custom made shell scripts developed by Dr. Daniel Kalthoff employing FSL McFlirt. The matrices of transformation parameters were saved and used later in the analysis of regressors. Regressors for breathing, motion correction and drift variations (of 1st, 2nd and 3rd order) were generated from the physiological monitoring data, the output files from McFlirt (par files) and drift functions, respectively. The functional data fluctuations (correlating with respiration, motion correction and drifting) were regressed out slicewise using FSL Regfilt.

Major regions of interest were chosen for the data analysis that are known to be mostly affected by the dMCAO and others that play an important role in brain function due to their association with the cortical affected areas. The following five bilateral regions were determined for pairwise correlation:

- The motor cortex (M), including M1 and M2.
- The primary somatosensory cortex (SS1) including the areas responsible for sensorial processing the limbs (where the functional deficits after dMCAO are observed) and all the remaining areas of the SS1 regions.
- The secondary somatosensory cortex (SS2), which together with the SS1 are irrigated by the MCA and directly affected by the ischemic damage.
- The thalamus (Th), a relay station for cortical information.
- The caudate putamen (CPu).

These regions of interest were extracted from a publicly available atlas, the Australian Mouse Brain Mapping Consortium atlas or AMBMC in order to minimize bias and allow comparisons among different studies and groups. Figure 2.4 depicts the anatomical representation of the selected ROIs in the mouse brain. Since left and right ROIs were taken into account for analysis, the final amount of assessed regions raises to ten.

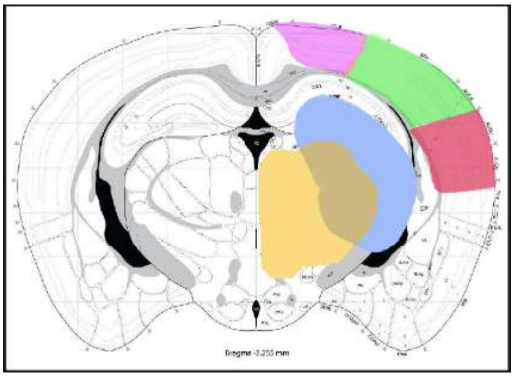

Figure 2.4: Anatomical representation of the selected ROIs.

- M in purple
- SS1 in green
- SS2 in red
- Th in orange
- CPu in blue

Subsequently, datasets were smoothed using FSL's SUSAN to enhance spatial Signal-to-Noise ratio, which reduces outliers in signal intensity by taking a value closer to its surrounding voxels. The edges of the ten selected ROIs are also smoothed in this process and the comparison between subjects is facilitated. The last step in the preprocessing consists of filtering the higher and lower frequencies that originate from signal drifts or physiological parameters (Biswal et al., 1996). My colleague Claudia Green adapted the parameters from Biswal during the development of her own doctoral project, and established them for this method in our lab. The bandpass filter excludes signal outside the 0.01 – 0.08 Hz range.

Next, the AMBMC selected labels need to be aligned to the functional data. For that purpose, the anatomical data was first converted to Nifti format (scaled up 10x), brain extracted with FSL's BET and bias corrected with FSL's FAST. It was then coregistered to an in-house generated custom-made structural nude mouse brain template (n=20) by means of an affine registration with 12 degrees of freedom, for the pre-stroke and 48 hours after stroke time points. This template had been previously coregistered to the AMBMC atlas. For the 2, 6 and 12 weeks time points, linear affine coregistration did not lead sufficient results and a different strategy was employed: the hippocampus was manually delineated and the results applied in a point set expectation nonlinear registration and was combined to a subsequent diffeomorphic nonlinear registration. The results of the affine or combined (point set + diffeomorphic) transformation, either matrices or warp fields, were combined and applied to the selected ROIs represented as labels in the AMBMC (Figure 2.4). Such labels are then transformed and aligned to the functional data.

Finally, the ROIs extracted from the atlas for both hemispheres are merged in a hyperstack. The datasets are used to calculate group analysis on the functional connectivity strength within each ROI (since the major labels include many voxels) and among ROIs, the latter for an assessment of the correlation between different brain regions, using FSLNets. The mean time course of all voxels within a ROI is calculated for each animal and stored in a textfile. For all animals in a group, the mean time course of each ROI was additionally averaged and the averages were pairwise cross-correlated with Pearson full correlation among every ROI. Resulting values are displayed as z-scores in a widely-spread-color coded matrix connecting all 10 labels to each other, for better visual inspection (See section 3.3.4).

2.11.2 Generation of FA maps

All eight diffusion scans were decomposed into one image for each diffusion direction and non-diffusion weighted images (A0 images). All A0 images were brain extracted using FSL's BET (the contribution to non-brain tissue were set to zero value) and motion corrected in two steps. First, between the first acquired and each of the other A0 images with FSL's MCFLIRT. The transformation details are stored for each A0 image in matrix form. Next, the resulting transformation matrices were linearly interpolated and applied to each diffusion direction. The final motion-corrected diffusion images from each diffusion direction were finally merged to one single file. The motion corrected diffusion datasets were then fed into DSI-Studio and non-brain tissue was discarded by applying a binary mask of the brain-extracted A0 images. The datasets were reconstructed within DSI-Studio and to extract diffusion parameters, i.e. the degree of anisotropy in pre-defined regions and to perform fiber tracking. Fractional anisotropy maps were extracted from DSI-Studio. For the region of interest manually delimited in the core of the ischemic lesion, the mean value was calculated with the Image processing tool ImageJ using custom-written macros, and all datasets were group averaged.

2.11.3 Generation of T2 incidence maps and determination of lesion volume

For the purpose of assessing lesion volume in the acute period and following its development during the entire longitudinal experiment, MSME scans were performed at 48 hours after stroke, and again at 2, 6 and 12 weeks. Mice were prepared for MRI acquisition as described above, except that there was no need to use Medetomidine for this measurement. The MRI signal in MSME scans was fitted on a voxel-wise basis with a monoexponential decay (custom-written IDL script).

For each subject, the first echo of the MSME scan was linearly co-registered with the corresponding anatomical TurboRARE image using FSL flirt (Jenkinson et al., 2002; Jenkinson and Smith 2001). Then, the anatomical data were co-registered to the in-house created template of 8 weeks old nude mice mentioned above. The two transformation matrices were combined and applied to the T2 maps, resulting in linearly transformed T2 maps. Cortical T2 value was determined and a T2 threshold at 15% or more above the normal values was set for reliable discrimination of the ischaemic lesion. Further, a mask was created with ImageJ software (National Institutes of Health, Bethesda, USA) to exclude the ventricles of each individual subject. From the co-registered T2 maps and the mean T2 threshold to determine ischemic tissue, stroke incidence maps were created using in-house ImageJ plugins.

In this mouse stroke model of distal MCA occlusion, the effective lesion encompasses i) the cortical tissue denoted by hyper- and hypo-intense areas and ii) the volume of lost tissue due to resorption of necrotic tissue. Due to the continuously increasing, massive morphological changes of the brain during the 12 weeks observation period after stroke, the following complex procedures became necessary for the quantification of the cortical tissue. Using ANTs (Avants et al., 2011), a nonlinear coregistration of the anatomical data (TurboRARE) onto the template was performed, followed by a nonlinear coregistration of the template onto publicly available mouse brain atlas of the neocortex (Ullmann et al., 2013). The two transformation matrices were combined and the inverse transformation was executed, mapping the cortex labels of the mouse brain atlas onto the original, unchanged anatomical data. The voxels of the contralateral, normal cortex and of the thinned and distorted ipsilateral cortex were summed up to determine the cortex volume of both hemispheres using FSLstats (FSL). Lost cortical tissue volume was the difference between ipsilateral cortex volume before stroke minus volume at the time point of interest after stroke.

Hyper- and hypo-intense areas were present in particular during the early stroke periods and became increasingly patchy with time. Therefore these regions were manually delineated in all slices for each time point from 2 to 12 weeks and the volume calculated.

2.12 STATISTICS

For behavioral tests and cortical volume determination, ANOVA for repeated measurements was performed (SPSS Statistics version 22, IBM Corp., USA), assuming sphericity in the distribution. After checking for statistically significant differences within repetitive measures in the same group, a post hoc Bonferroni test was chosen to check differences among the groups at the same time point. One-sided Student’s t-test was used for the normalized values of the rotating beam test. A p-value ≤0.05 was considered to be significant, and p ≤0.005 was considered to be highly significant.

3

Chapter 3

Characterization of dMCAO

as a model for cortical stroke

3.1 AIM

Brain imaging has enabled the characterization of human stroke, including the concept of evolving stroke damage and the ischemic penumbra. However, there are 3 concepts regarding human stroke that seem to be less primarily included, even neglected, in the translational research in animal models. These 3 concepts include the small size of the ischemic lesion (4.5-14% of the ipsilateral hemisphere), the substantial degree of reperfusion originating from clot lysis and collateralization, and the patterns of recovery that follow a reproducibly determined functional reorganization in the brain. (Carmichael, 2005)

One of these above mentioned 3 concepts, the small size of the ischemic lesion in the vast majority of human strokes is the primary target of neurotherapeutics. Only few of the established animal models can mimic the size of the average human stroke, one of them being the electrocoagulation distal middle cerebral artery occlusion, as described in the Introduction Chapter.

For translational purposes, it becomes imperative to know the model in depth, and my aim was to characterize the development of the lesion *in vivo* and *ex vivo*, together with the symptomatic recovery (behavioral testing) and functional connectivity of selected areas of the brain network through resting state functional MRI. Long-term functional and behavioral outcome has not been thoroughly characterized (Rosell, 2013), creating a limitation for translational basic research that should provide supporting data to enable further clinical trial evaluation.

3.2 EXPERIMENTAL DESIGN

There are very few long-term studies where the consequences of stroke in mice have been observed. Caballero-Garrido explained the role of microRNA miR-155 in the modulation of infarct size, in a study that lasted 3 weeks (Caballero-Garrido, 2015). A comparison of several MCAO models to check for reproducibility and location of lesion was performed by Kuraoka during a period of 8 days (Kuraoka, 2009).

Thus, I decided to observe and describe the development of the lesion in both the acute and the chronic phase, regularly checking for behavioral performance and network connectivity, as well as histological changes. Finding the right frequency of procedures to apply to the mouse was a delicate balance, since I did not want to exhaust the animal and overexpose it to unnecessary anesthesia sessions, although I was always trying to obtain the most amount of relevant data throughout the observation period.

I included observations before any intervention to have a baseline measurement to compare the following observations to. Several experiments took place during the first days after surgery, and following the initial acute period the frequency of observations became less dense. Most of the animals were kept alive until the end of the observation period of 12 weeks after ischemic onset, with a few exceptions that were sacrificed at 3 selected time points (48 hours, 2 weeks and 6 weeks) for the purpose of *ex vivo* characterization of histological changes.

Figure 3.1 is an outline of the timeline of experiments including MRI measurements – either for MSME scans, resting state fMRI or diffusion data –, behavioral observations and the time points in which the subjects were sacrificed for histology and IHC experiments.

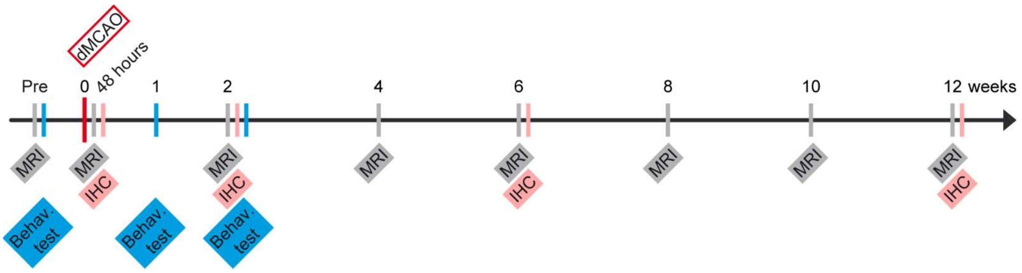

Figure 3.1: Schematic of the experimental protocol. Outline of experimental design for the cohort of mice with dMCAO. The sham occluded group was similarly designed. The ischemic cohort was divided into two subgroups for the purpose of having enough time to perform all experiments on each animal. The second subgroup was prepared only after the first one had concluded the longitudinal experiments. The sham occluded group was smaller in size as the ischemic cohort.

3.3 Results

3.3.1 Lesion volume and tissue loss

For a correct assessment of the amount of brain tissue affected by the lesion, the changes in the brain morphology and the development of the stroke affected area, the animals underwent several MRI scan sessions starting at 48 hours after surgery every second week until the end of the longitudinal experiment 12 weeks later. These acquired anatomical scans served for the purpose of qualitative inspection of lesion location and size. The vasogenic edema in the affected tissue 48 hours after stroke covers a large extent of the dorsolateral cortex across the rotro-caudal axis, as shown on a multislice set of T2-weighted images for one representative animal in Figure 3.2.

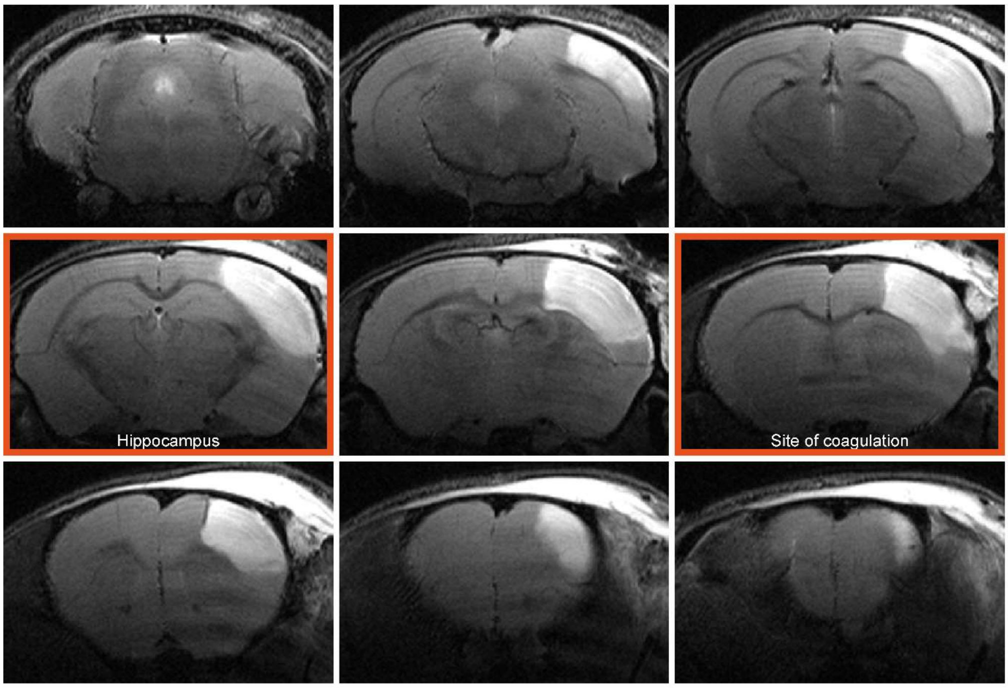

Figure 3.2: Cortical lesion depiction at the acute time point after ischemia. A representative example of T2-weighted multi-slice MRI of a mouse 48 hours after dMCAO shows pronounced hyperintense regions in the right cortex covering a major part of the caudo-rostral extent. The image planes at the site of coagulation and the site where the hippocampal distortion is maximal are marked with a red frame. These two planes are used for further detailed analysis of the temporal development of the pathophysiological changes.

At 48 hours, 2 weeks, 6 weeks and 12 weeks after surgery, an MSME scan was included in the scan session, for the purpose of quantitative analysis of hyperintensity regions corresponding to edematous areas in the brain, directly related to lesioned tissue. All operated animals in this group showed a cortical edema in the area adjacent to the electrocoagulation of the artery. The stroke location was consistent in all animals: such reproducibility in is reflected in a heat map, also called "Incidence map" (Figure 3.3). This map shows where the hyperintensity signal is detected – using a threshold to differentiate from other less hyperintense areas and a mask to detect only areas affected by edema. The mask is manually drawn taking into consideration where the lesion is to be expected in the cortex, and excluding areas without supply of the MCA. The incidence map also shows the amount of animals where the lesion-related hyperintensity is present: in the case of the subjects scanned 48 hours after stroke, the amount of animals presenting a cortical stroke is of 100% (Figure 3.3A). As clearly shown in the heat map, the stroke size is not identical for all animals: for 16 of the 18 animals, the change in hyperintensity is evident in all 6 selected coronal cuts, one animal presents this change is 5 of the sections and the remaining animal in only one of the sections meaning that the edematous tissue is less extended than in the majority.

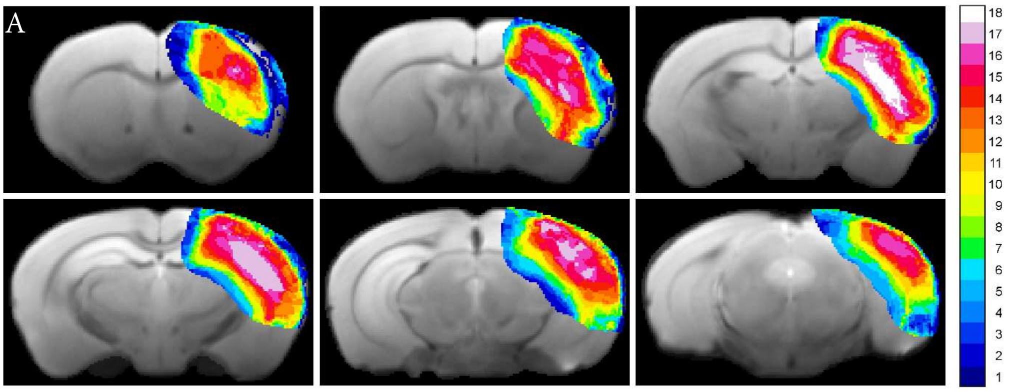

Figure 3.3: Incidence maps of ischemic lesion. T2-weighted multi-slice MR imaging was performed after dMCAO in 19 animals which were carried through the whole 12 weeks observation period. Coregistration with a mouse brain template and superposition of the hyperintense region at this time point onto the template data set indicated a stable and robust ischemic region in the cortex covering a large part of the ipsilateral cortex. A) at 48 hours after stroke; B) 2 weeks after stroke; C) 6 weeks; and D) 12 weeks. One scan was discarded in the first time point, another one in the 6th week, an another in the 12th week. One animal died at the 6th week assessment, two more died before the 12th week.

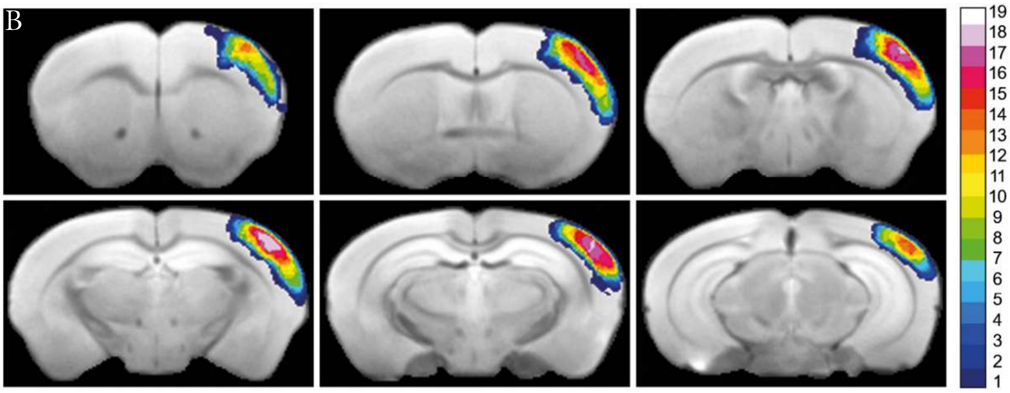
B
19
18
17
16
15
14
13
12
11
10
9
8
7
6
5
4
3
2
1

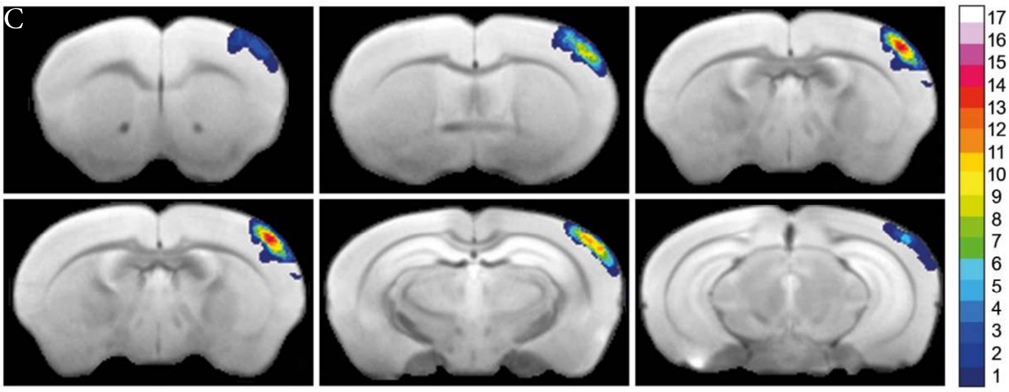
C
17
16
15
14
13
12
11
10
9
8
7
6
5
4
3
2
1

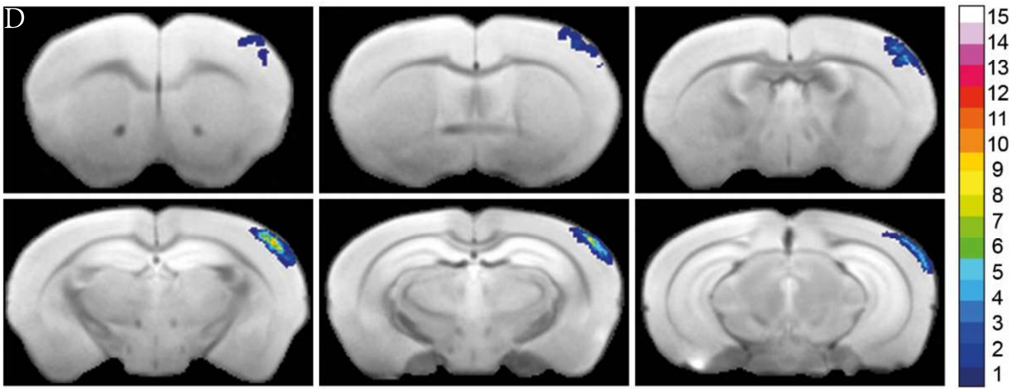
D
15
14
13
12
11
10
9
8
7
6
5
4
3
2
1

The lesion volume decreased over time and by the second week after stroke the hyperintensity observed in the first 48 hours had mostly vanished in the peripheral areas, and remained still present for most of the animals in the areas proximal to the electrocoagulation site. However, the threshold used to determine the 48 hours time-point hyperintensity no longer detected the lesion in the MSME acquired data, in spite of it being clearly visible in the anatomical scans. Therefore, I visually inspected every slide acquired with the TurboRARE protocol of every subject and manually drew the remaining lesion site over the anatomical slide for each of the animals. It was then possible to create an incidence map based in manually drawn masks, and not in hyperintensity detection above a designated threshold. Figure 3.3B shows the incidence map for 2 weeks after stroke. At this time point, the lesion can still be detected in 100% of the operated animals. Even before performing a quantitative analysis on the lesion volume, it is clear to visualize that the edema size has dramatically decreased at this time point.

The same manual analysis was performed for the cohort scanned at 6 and 12 weeks after stroke, since the contrast with the hyperintense area became even less evident, although still completely distinguishable for visual inspection. Figure 3.3C displays the incidence map for the cohort scanned 6 weeks after the ischemic damage.

This is the first moment in which the lesion is no longer assessable via visual inspection for all the subjects. The incidence for this time point is no longer 100%: only in 82% of the mice the lesion can be localized in any of the coronal cuts. The difference in the lesion size among the subjects becomes evident as some animals display clearly distinguishable and relatively prominent edematous tissue whereas others have completely resolved it according to the MSME scan.

Finally, 12 weeks after stroke, the lesion is still visually recognizable in 66% of the animals as depicted in Figure 3.3D.

Since in the control group, also called “sham occlusion group”, the surgery does not involve damage to the MCA, there is no ischemic damage in the tissue, no edema develops and therefore there is absence of hyperintensity upon MSME scan. No incidence maps were generated for this group. Figure 3.4 shows selected coronal cut sections of the anatomical scan -obtained by the TurboRARE protocol- of a mouse in which sham occlusion was performed, 48 hours after the surgery.

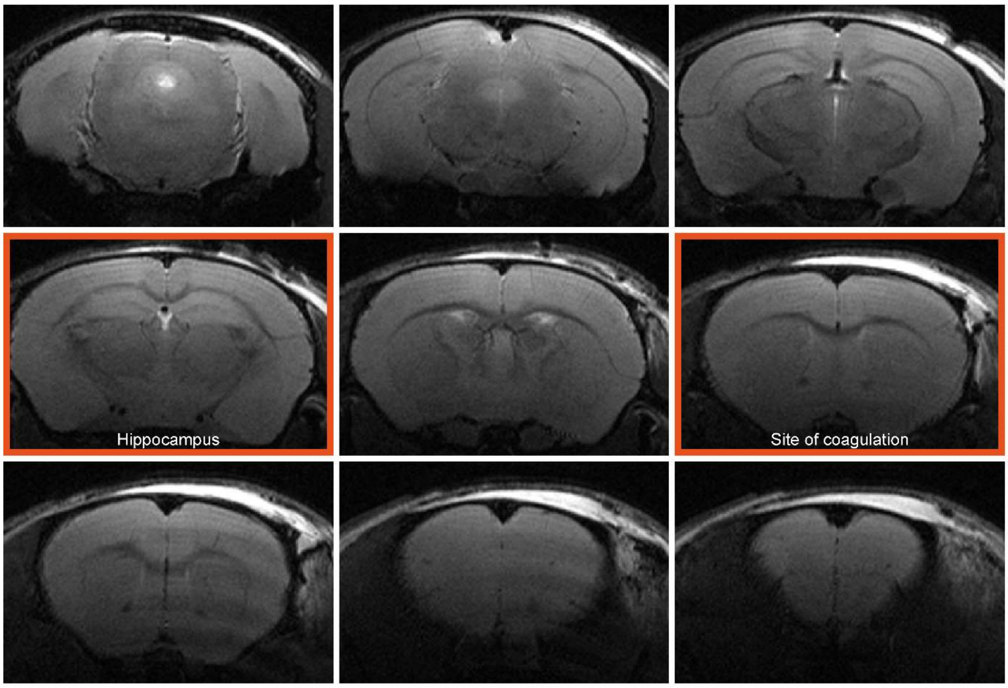

Figure 3.4: Cortical lesion depiction at the acute time point after sham occlusion. A representative example of T2-weighted MRI of a mouse 48 hours after sham dMCAO shows both hemispheres equivalent with no sign of damage. Only at the cortical surface at the level of the sham coagulation site a minute hyperintense spot is marked indicating a weak reaction to the hot forceps touching the brain surface during sham surgery. The image planes at the site of coagulation in the ischemic animals and at the level where the hippocampal distortion is maximal in the ischemic animals are marked with a red frame. These two planes are used for further detailed analysis of any potential temporal changes.

Figure 3.5A highlights the development of the anatomical changes in two different planes: the site of the electrocoagulation of the MCA and the site where the hippocampus and cortex width show the most drastic changes. Both sites were selected after inspecting all planes (depicted in Figure 3.2) for all animals. Figure 3.5B shows the same coronal slides for sham occluded animals. For the ischemic cohort, a thinned cortex becomes clearly visible on the ischemic hemisphere already at 2 weeks. At 4 weeks, parts of the cortex at the coagulation site have vanished completely so that the white matter reaches the brain surface. The hippocampal enlargement is visible starting at weeks 2, being more evident at week 4, expanding further and filling the void left by the thinning cortical tissue gradually until the end of the observation period at week 12.

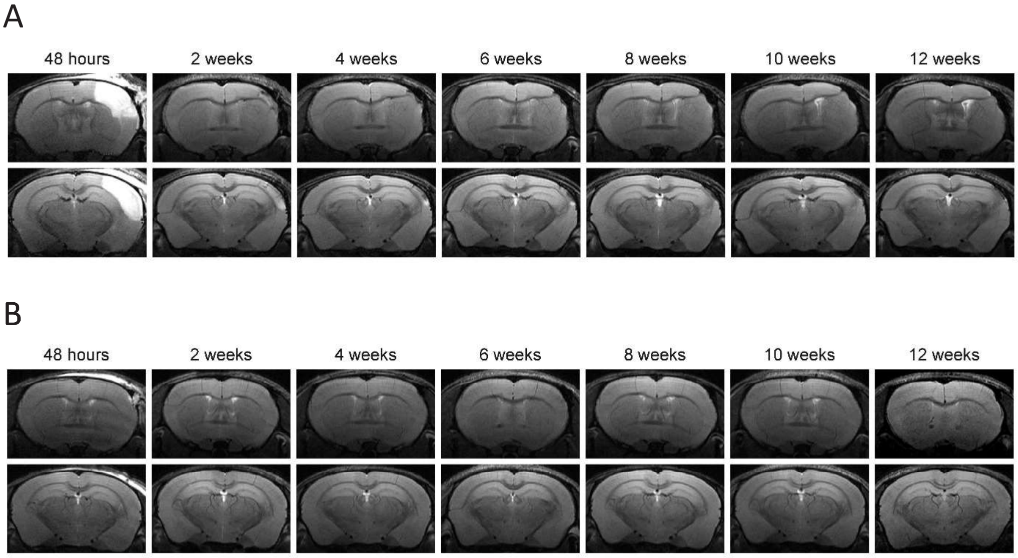

Figure 3.5: Development of the lesion during 12 weeks. A) T2-weighted MR images of two selected coronal positions through the brain of a representative mouse are shown at 48 h and for time points every two weeks following dMCAO. The slice positions were selected as described in Fig. 3.4 The hyperintensity at 48 h quickly fades away, and only in the lower row at the level of the hippocampus a small hyperintense spot at the cortical surface remains at later times. In this plane the expansion of the hippocampal volume and its movement towards the brain surface become pronounced with time. In the upper row of images at the level of the MCA coagulation, the increasing thinning of the cortex is visible together with the pronounced bending of the corpus callosum towards the brain surface on the site of coagulation. B) Similar dataset corresponding to the sham dMCAO surgery. The small hyperintense spot at 48 h quickly fades away. No increase of hippocampal volume and movement towards the brain surface are visible. In the upper row of images at the level of the sham dMCA coagulation (cf Fig. 3.4), no cortical thinning is detected and no bending of the corpus callosum towards the brain surface.

Next, I proceeded to quantify the observed changes in lesion and cortex volume: through the generation of the incidence maps the lesion volume had concomitantly been calculated. To calculate the cortical volume it was necessary to manually delineate the cortex for each subject, since the deformation of the hippocampus and the thinning of the cortical tissue hindered the linear coregistration of the anatomical scan to the atlas where the subcortical areas are detailed. Having calculated the cortical volume separately for both hemispheres, for each animal and for all above mentioned time points, I compared them to the naïve state of the brain. The amount of cortical tissue on the contralateral healthy hemisphere remained unchanged over the observation period. The brain structures in this contralesional side

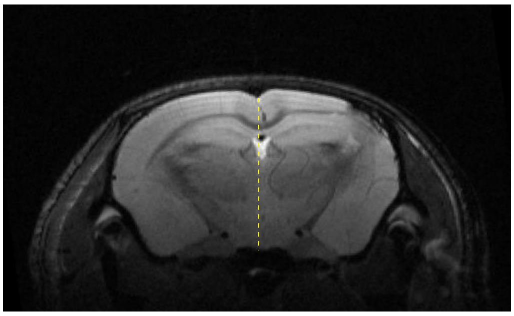

Figure 3.6: Shift in the midline of the brain 12 weeks after stroke. This change is a consequence of the movement of several structures to the right surface of the cortex i. e. the hippocampus. The yellow dashed line represents the original location of the brain midline.

of the brain presented the same morphology as in the state before surgery with the exception of a mild shift of the midline to the right hemisphere, which is best visible 12 weeks after ischemia, as depicted in Figure 3.6.

In contrast, the cortex volume of the right hemisphere presented noticeable changes. The masks of the ischemic cortex were used to calculate its volume throughout the brain expressed both in voxels and mm^3. For the purpose of later comparison and translational research, only results in mm^3 were used for further calculations (see next paragraph).

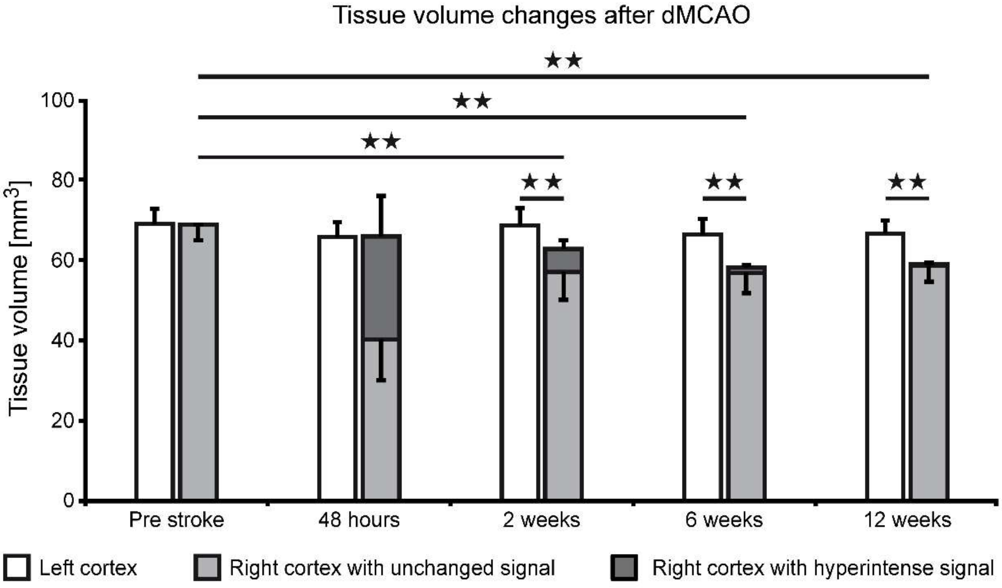

Figure 3.7: Tissue volume changes after dMCAO. Quantitative analysis of the cortical tissue volume with hyperintensity (dark grey bar) and of the normal appearing tissue (light grey bar) is presented for the whole 12 weeks observation after dMCAO. While the hyperintensity is maximal at 48 hours with 38 ± 15 % of cortical volume, it quickly decreases and reaches values of 0.6 ± 0.5 % at 12 weeks. Already visible at 2 weeks is the loss of cortical tissue, as the sum of light and dark grey bars are significantly less than the cortical volume of the contralateral hemisphere. This tissue loss further increases with time. N=11; two stars $p<0.005$.

Figure 3.7 presents the results of hyperintensity areas and cortex volume calculations. In the naïve state – depicted as pre-stroke time point – the volume of the left and right cortex appear identical. The same statement can be claimed for the measurement at 48 hours after surgery, however with the inclusion of a remarkable hyperintense volume corresponding to the edema created by the ischemic changes. From this time point on, the right cortex volume comprises non-affected tissue and edematous tissue. The sum of both measurements was compared to the contralesional cortex volume which shows no alterations in thickness nor edema formation. Two weeks after stroke, a statistically important noticeable difference with a p-value below 0,005 can be found between the left and right cortical volume. In the right cortex, the amount of hyperintense signal in the tissue has shrunk in comparison to the previous time point, and so has the total amount of cortical tissue in the right hemisphere in comparison to the left side. Such decrease in values was determined in the shrinkage of the cortex thickness around the area where the electrocoagulation of the MCA has taken place.

Continuing to the next observation point, six weeks after stroke, the volume of the right cortex keeps descending in comparison to the same structure on the previous time point, so does the hyperintense area. Twelve weeks after stroke, the changes in cortical value have stabilized, and the only change observed is the further decrease of the edematous area.

3.3.2 BEHAVIORAL PERFORMANCE

A battery of behavioral tests and assessments were applied to the subjects in order to evaluate suspected sensorimotor changes due to the lesion located in the somatosensory cortex. Body weight was monitored and the modified Neurological Deficit Score (mNDS) was recorded starting before surgical procedures and every second week until the end of the experiment in order to have a longitudinal evaluation of mNDS though the full length of experiments. Using the same mNDS as previous studies conducted in our group, I was able to support evaluation of stroke severity compared to different model of stroke, the filament MCAO (Green et al., 2018, Hamzei Taj et al., 2016).

Figure 3.8 shows the individual scoring in grey and the average scoring in red. The vertical axis was modified to fit the data for better visualization, the scoring has a maximum value of 16 points. The cohort of mice for

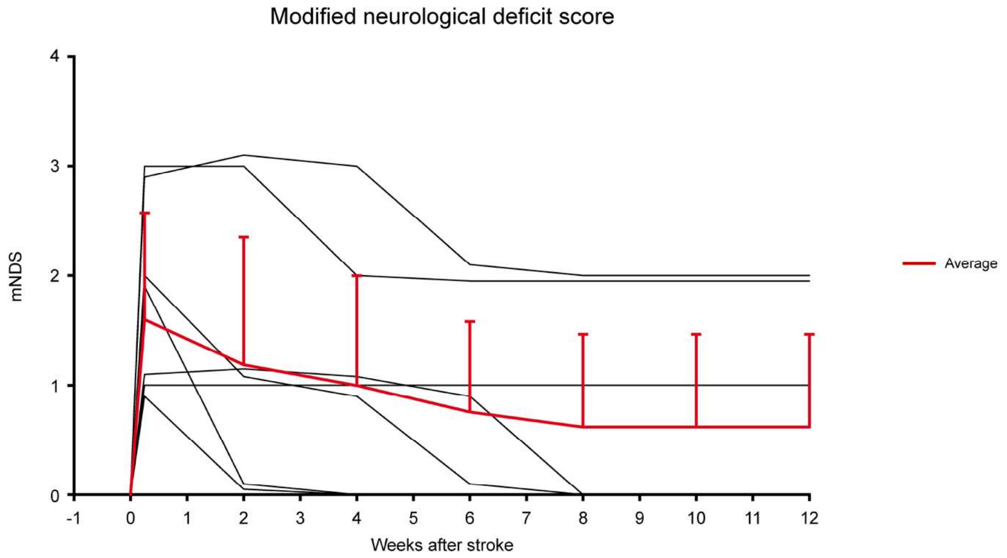

Figure 3.8: Modified Neurological Deficit Score. In grey the individual measurements for every subject, in red the average of the group. Only 8 animals were considered for this test, which belonged to the first subgroup of the ischemic cohort. For the second subgroup we chose a different test.

this test consisted of 8 subjects, which were the amount of subjects in the first experimental cohort. After analyzing the results for this cohort it was concluded that the mNDS would not be performed in the rest of the animals to be operated. The points gained in the scoring at the beginning of the assessment correspond exclusively to the following concepts: affected flexion of forelimb – one point – and proprioceptive test – two points –, that represent motor and sensorial response hindrance. Over time, the values revert to baseline for 5 of the subjects, the remaining 3 decrease their scoring down to 2 or 1 points. After the 6th week, the performance reaches a plateau in which no further improvement can be seen. The mice do not present a considerable weight loss nor a deteriorated general state, they do not display any difficulties for eating, drinking, grooming or socializing. Statistical analysis was not applied for this test due to the high standard deviations and low number of subjects.

The subjects were also exposed to the Rotarod test to evaluate the motor function and motor loss in a more exhaustive manner, with a task that becomes more challenging to perform over the passage of seconds due to the difficulty to remain on a constantly accelerating rod. Animals were familiarized with the device and task before the surgical procedure and tested again for their performance one week after surgery. Since this test involves a physically intense task, and the subjects were exposed to many other measurements and anesthesia sessions in the days following the surgery, it was decided that the Rotarod assessment would be performed only once at one week after ischemia. The ischemic group revealed a clear decrease in their capacity to remain on the accelerating rod in comparison to the sham occluded group, which served as the control. Figure 3.9 (left) shows the amount of seconds in which the subject no longer holds grip to the rod and falls to the bottom grid of the device. The amount of subjects tested was 16 for the sham occluded group and 19 for the ischemic group. A closer inspection of individual performances shows that 3 subjects from the control group perform poorly in comparison to the rest of that group that displays a highly homogenous performance in the task remaining on the rod until the end of the test at 80 seconds. In contrast, the different subjects of the ischemic group display heterogeneous task performances in a continuum, with a mean located at 40 seconds after initiation of the rod rotation, which corresponds to a speed between 20 and 30 rpm. It is notable that none of the subjects of this group remained on the rod at the time in which the test was finished – they all fell to the floor before the 80 seconds mark, 4 of the subjects falling after the rod stopped accelerating to remain on a constant speed.

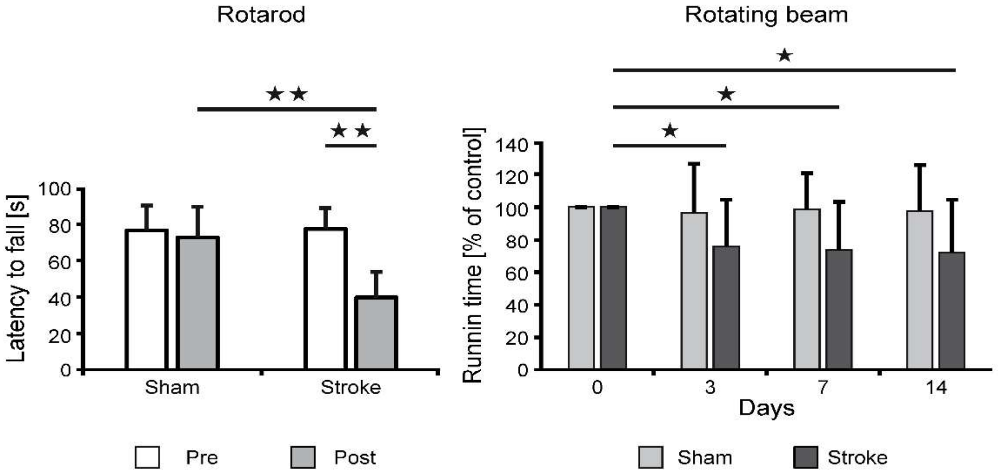

Figure 3.9: Behavioral tests. Rotarod test at 1 week after dMCAO (left diagram) shows a highly significant performance reduction of the ischemic animals compared to the pre-stroke value and compared to the sham group. The rotating beam test (diagram at right) shows a significant performance reduction of the ischemic animals relative to the pre-stroke situation, persisting at all time points during the first two weeks, while the behavior of the sham mice remains unchanged over time. Sham n=16; stroke n=19. One star $p<0.05$; two stars $p<0.005$.

Both the control and the ischemic group were also assessed in the Rotating Beam test. Similarly to the Rotarod test, the Rotating Beam test evaluates the motor performance, however in a less challenging fashion. The test was performed on the day of stroke onset – or sham occlusion, before surgery, for baseline measurements and again at 3, 7 and 14 days after the operation. Mice had to be trained before surgical procedures in three training sessions separated by two days between sessions to familiarize them with the device and task. They also had to be motivated with food pellets in the arriving end of the beam to encourage them to run in the right direction and to prevent them from turning around back to the starting end or to stay static on the rotating beam and subsequently fall to the floor. The resulting individual speeds were heterogeneous so they were normalized to baseline levels in order to be able to compare the performance of all individuals in the same graph. As displayed in Figure 3.9 (right), the control group did not show any statistically significant difference among the performance before the surgical procedure and after it, at any point during two weeks. On the contrary, there was a significant difference ($p < 0.05$) among the baseline value of the ischemic group when compared to any of the sessions after surgery. Interestingly, no significant difference was noted between the test result at day 3 and day 7, or day 7 and day 14 after ischemia onset.

Although not evidenced in the bar graph, it is relevant to mention that those animals that displayed a slower phenotype after the training sessions, remained in the slow end of the spectrum after surgery. The same statement is valid for the ones that were faster after training: they were also the fastest of the cohort when evaluated during the following days.

Last but not least, animals were evaluated for their sensorial performance in the Corner test. Results were again normalized to baseline, since every animal displayed a different tendency to turn right or left during the pre-surgical assessment, only one of them choosing both sides on a balanced ratio of 50:50 right turns:left turns. The baseline value was defined as the percentage of turns to the right, and the rest of the assessments were compared to that initial relative value, regardless of the absolute number of right turns. Figure 3.10A shows the results of the sham occluded cohort for the period of 2 weeks after surgery. The average of measurements depicts no tendency to turn to one or other side after the surgical procedure. The heterogeneity in the measurements is quite vast so that the standard deviation for the dataset ends up being very ample, not showing any significant differences among assessments in the various measurements after surgery.

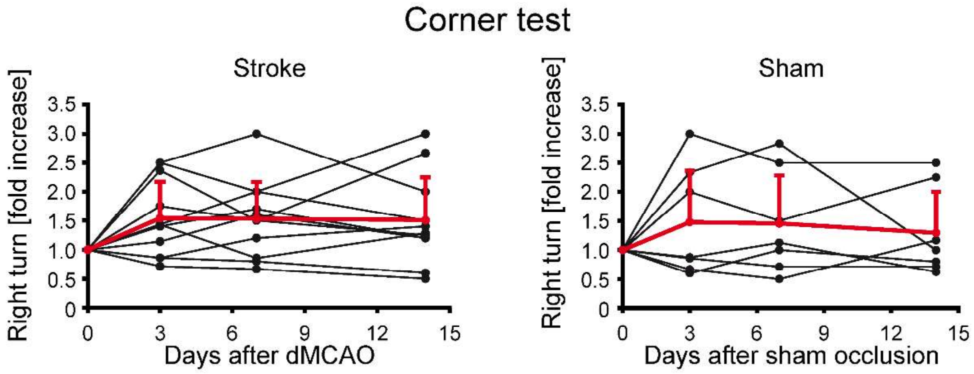

Figure 3.10: Analysis of the corner test. The corner test was performed at various time points during the first two weeks following distal MCA occlusion (left) or sham surgery (right). The scatter in individual behavior was rather large. Moreover, no difference was noted between ischemic and sham group. dMCAO n=11; sham n=7.

Figure 3.10B displays the results of the corner test for the ischemic induced cohort. In a similar way as the sham occluded group, assessments after surgery also show broad heterogeneity, without a clear tendency of change after stroke. The analysis of the average and its standard deviation shows no significant change between any of the data points over time.

3.3.3 Histology and immunohistochemistry

Some of the animals were sacrificed at different time points before reaching the 12th week after stroke in order to obtain histological samples for closer cellular and immunohistochemical evaluation. The Nissl staining allowed to visually inspect the distribution of nuclei and cells throughout the coronal cuts, in an attempts to shed some light on the process of cortex thin-

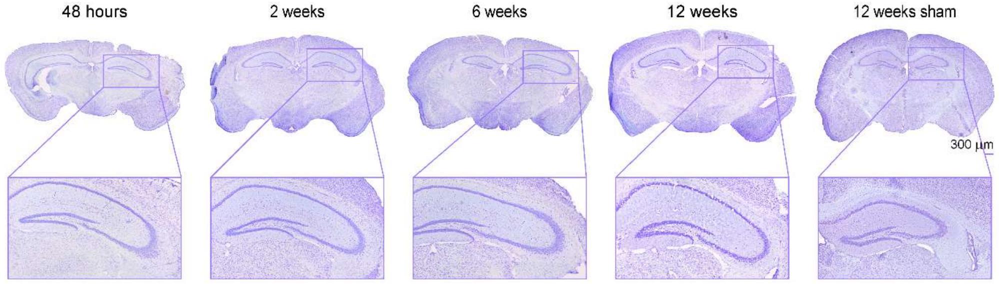

Figure 3.11: Nissl staining of cortical sections at the level of the hippocampus. Nissl staining of ischemic mice is presented at several different times over the 12 weeks observation period, together with a representative sham animal at 12 weeks after the sham surgery. At 48 hours, a beginning thinning of the cell density in the hippocampus is visible. In comparison, the density of cell nuclei in the sham mouse shows no difference between both hemispheres.

ning over time. Figure 3.11 shows the resulting images taken at different time points, together with a close-up of the lateral end of the affected hippocampus.

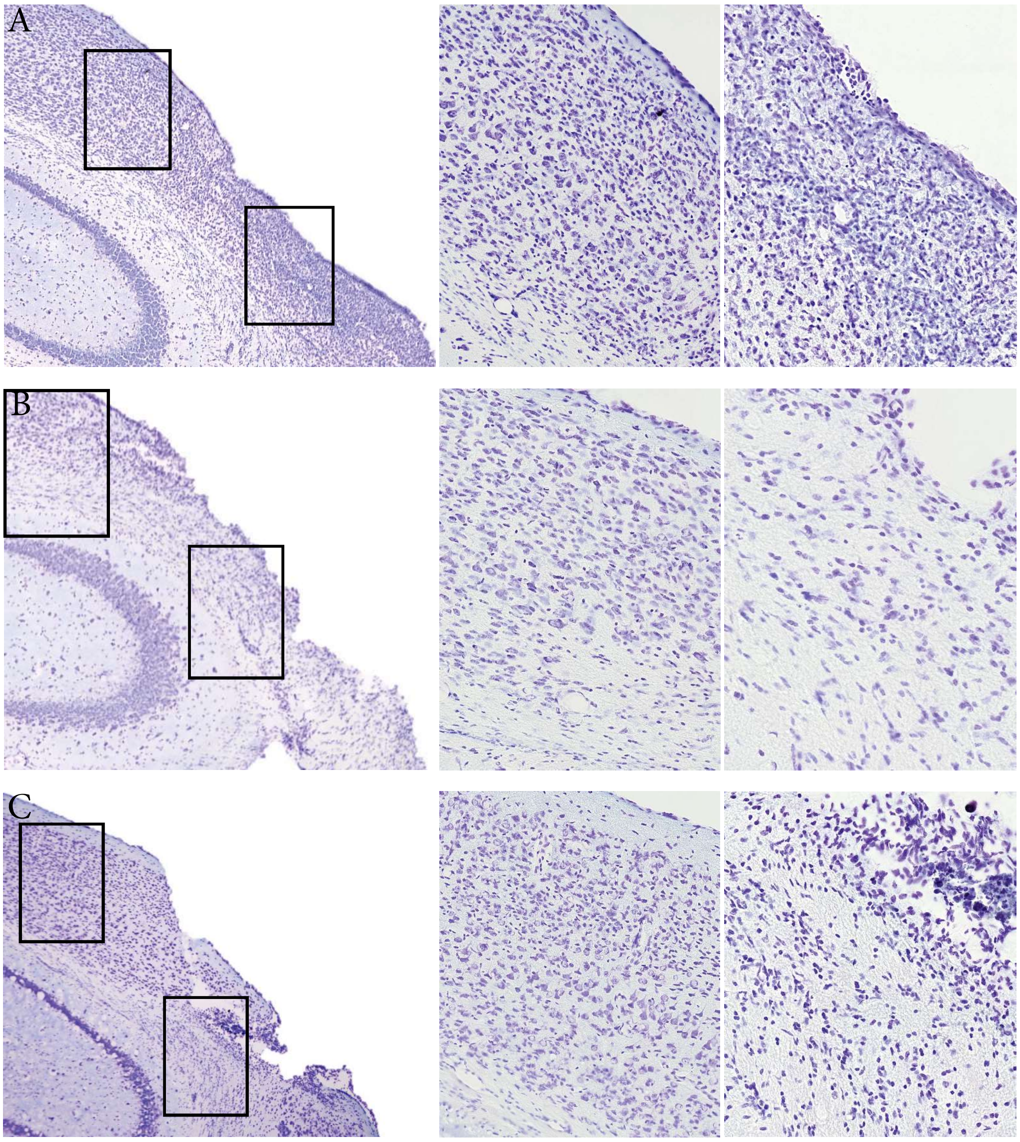

Figure 3.12: Nissl staining of cortical sections at the level of the thinning cortical tissue. Nissl staining of ischemic mice is presented at selected times over the 12 weeks observations period. Left panel, overview of the right cortex at the site of the dMCO-induced vasogenic edema. Two representative tissue areas are selected to show the cellular architecture: on the site of coagulation and the adjacent tissue. Middle panel, adjacent tissue to the site of coagulation, all cortical layers are distinguished for all time points. Right panel, cellular architecture at the site of coagulation. A) two weeks; B) six weeks; and C) 12 weeks after dMCAO.

Note the symmetry in thickness between the right and left cortex for the sham occluded group in the far right of Figure 3.11. In contrast, all other four brain sections corresponding to the ischemic group show asymmetry in the cortical thickness together with a mild deformation of the cornu ammonis (CA) and the external adjacent tissue, particularly for the 6th and 12th week time point. The difficulty to detach the whole brain from the skull upon perfusion 48 hours after stroke limited the amount of cuts available for the first time point samples, therefore the almost unaltered symmetry of the hippocampus at this moment is not reflected in the left-most panel. In this same cut, the cortex is slightly discontinued in the motor areas, however this is an artifact from the perfusion and cutting procedures.

By taking a closer look at the most prominent changes in the cortex it is possible to inspect the shrunk tissue. Starting at the second week after ischemic changes, there is already an evident disappearance of layer I together with layers II and III, although advanced immunohistochemical staining should be performed to confirm the absolute absence of these mentioned layers at the site of the electrocoagulation as detailed in Figure 3.12A right panel. Layer VI can be distinguished without disruption, layers V and IV are difficult to assess due to an apparent loss of extracellular matrix: the cells seem to have been pushed closer together. The meninges are clearly disrupted in the gap where the forceps touch the brain surface. Figure 3.12A middle panel shows the cortex adjacent to the lesion, all cell layers are clearly distinguishable. Figure 3.12B shows the state of the cortex 6 weeks after ischemic changes. The abscess in layers I to IV of the cortical tissue are presumably a consequence of the ischemic necrosis. In the site of the lesion, Layer VI can still be distinguished without disruption and layer V is now the interface to the meninges. The thickening or expansion of the CA is notable compared to previous time points.

Figure 3.12C shows the development of the lesion at the end of the experiment at the 12th week. In principle, the organization of the layers has not been further changed in comparison to the previous time point at 6 weeks, the total disorganization of the cellular architecture has not been resolved. Layer VI can barely be distinguished in the interface to the brain borders. It is remarkable that the corpus callosum has increased its width (partly) in the location where the extracellular matrix of the cortex has shrunk. In many subjects I observed that the corpus callosum stretched out to reach the surface of the brain, entirely deforming its original morphology. The rearrangement of the corpus callosum can be observed in Figure 3.13.

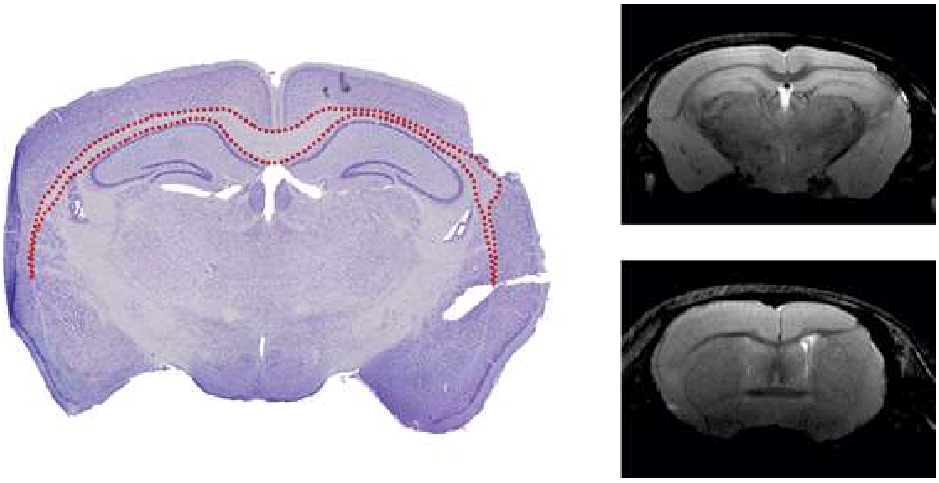

Figure 3.13: Structural changes in the corpus callosum. To the left, Nissl staining of an ischemic mouse is presented at 12 weeks after dMCAO. The dashed red line circumscribes the corpus callosum, note the enlargement of the structure towards the lesion site. To the right, two T2-weighed MRI images of the same mouse where the corpus callosum in the ipsilesional hemisphere follows a direction towards the brain surface.

After the close inspection of the cellular layers at different time points, I assessed microglial and astrocytic presence in the ischemic core. Although the extension of the necrotic tissue was reduced over time, microglia and reactive astrocytes could be localized close to the site of the electrocoagulation. Figure

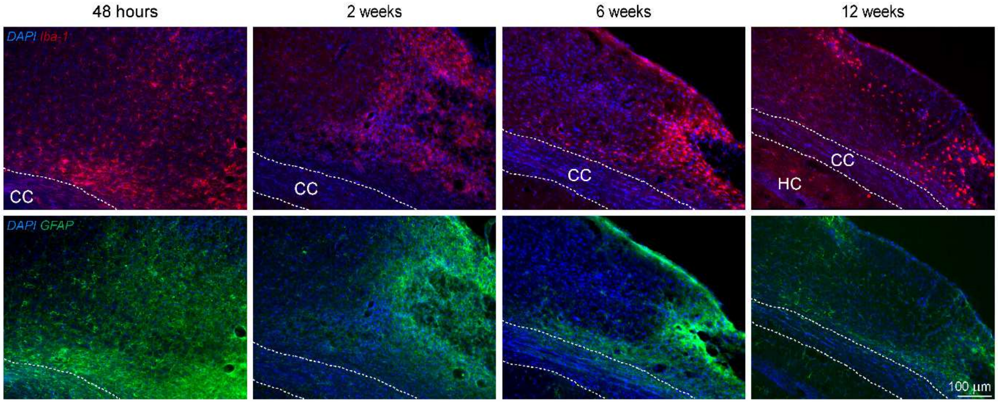

Figure 3.14: Immunohistochemical staining for inflammation and reactive gliosis. The upper row presents Iba1 positive activated microglia and infiltrated macrophages in the cortical lesion periphery. Iba1 positive cell density increases with time and inflammatory response remains high during 12 weeks. In the lower row, GFAP staining shows reactive astrocytes forming a glial scar around the lesion and spreading in the cortex along the corpus callosum. For both panels, microglia and astrocyte distribution start diffuse and become more localized through the end of the observation period. Abbreviations: CC: corpus callosum; HC: hippocampus.

3.14 depicts the presence of both cell types in the area considered as the lesion in a timewise comparison of cellular types, all including Hoechst staining for nuclei.

In the upper panel, the red signal evidences the microglial marker Iba-1 whereas in the lower panel the green staining displays the GFAP protein expressed exclusively by astrocytes. The microglial and astrocytic recruitment does not resolve in 12 weeks, however the area in which the green and red signal stems from shrinks, together with the resolution of the edema.

3.3.4 Resting state fMRI

As already mentioned in the Material and Methods section, the results of the resting state functional MRI assessment are expressed as correlation factors among all the selected regions of interest. The correlation factors were z-scored before group average and displayed color coded in numerically symmetric matrices. In such matrices, the bottom left right shows the color coded values and the upper right half the numerical values. There are subgroups of correlation factors that are worth mentioning:

1. On the upper left apex, the connectivities among the contralateral hemisphere (in relation to the lesioned side).
2. On the lower right apex, the connectivities among the ipsilesional hemisphere.
3. On the bottom left square the transhemispheric correlations. The sketch in Figure 3.15 shows a graphical explanation of these 3 above mentioned subgroups.

Figure 3.15: Representation of the different partition of the matrices displayed in this chapter. The hemispheres are divided into left (contralesional) and right (ipsilesional). Hence, different parts of the matrix show the intrahemispheric contralesional correlations (dark gray, upper triangle), the transhemispheric correlations (medium gray, square) and the intrahemispheric ipsilesional correlations (light gray, bottom triangle).

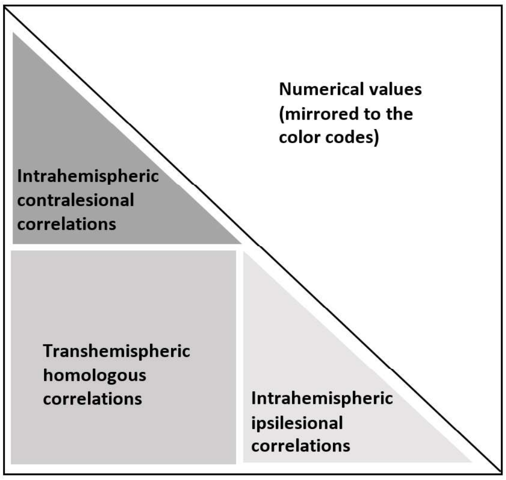

My first approach was to evaluate the development of the brain functional connectivity in the sham operated mice. Animals were scanned for RS before the surgical intervention and 2, 6 and 12 weeks after it. The resulting matrices for all 4 timepoints for 15 subjects is depicted in Figure 3.16A. The qualitative inspection of the matrix as an indicator of global connectivity strength suggests a continuation of the basal connectivity level throughout time. The second week scan shows a subtle decrease in the interhemispheric sector and a return to baseline levels on the sixth week. The same sector displays an increase on the 12th week.

A quantitative analysis of the data was carried out applying a threshold of 0.2 in change of z-scores in the difference between cross-correlation values for detection of significant changes in connectivity over time. In the sham occluded group, there are no significant changes to be observed until the 12th week, where all three cortical transhemispheric correlations – motor, primary and secondary somatosensory – show an increased connectivity compared to pre-surgical values. On addition to those, the connectivity strength between the ipsilesional motor cortex and the ipsilesional primary somatosensory cortex also shows an increase above the 0.2 threshold. For better visualization on anatomical nodes, the threshold values have been represented over a coronal brain template in Figure 3.16B, where the location of the selected regions of interest are pointed out.

Next, the ischemic group was evaluated for resting state fMRI results. Same as in the sham group, connectivity matrices were generated for the same 4 time points, shown in Figure 3.17A. Interestingly, the baseline values differ slightly from the sham occluded group baseline values, although none of the cohorts have undergone ay treatment yet. Following the ischemic cohort's results over time, it is possible to observe a clear increase in global connectivity strength at two weeks after stroke. Such increase continues to develop, since 6 weeks after surgery, the global strength has risen even further reaching its maximum values at the end of the observation period at 12 weeks. At this last time point, the stronger changes are spotted in the intrahemispheric contralesional and the transhemispheric sectors.

Applying the 0.2 of change in z-values threshold to filter out minor variations, the analysis all the three time points after ischemia compared to baseline delivered the following results:

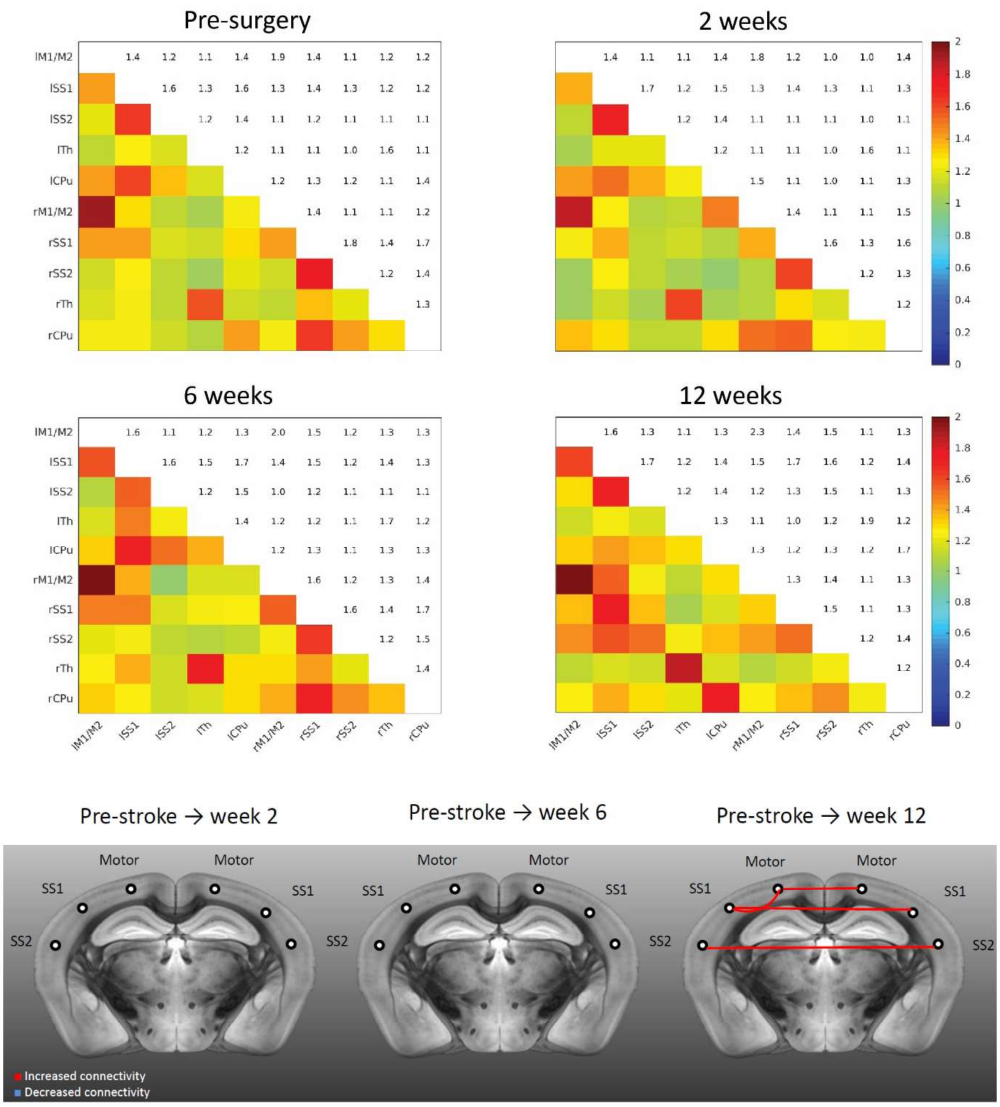

Pre-surgery

	lM1/M2	lSS1	lSS2	lTh	lCPu	rM1/M2	rSS1	rSS2	rTh	rCPu
lM1/M2		1.4	1.2	1.1	1.4	1.9	1.4	1.1	1.2	1.2
lSS1			1.6	1.3	1.6	1.3	1.4	1.3	1.2	1.2
lSS2				1.2	1.4	1.1	1.2	1.1	1.1	1.1
lTh					1.2	1.1	1.1	1.0	1.6	1.1
lCPu						1.2	1.3	1.2	1.1	1.4
rM1/M2							1.4	1.1	1.1	1.2
rSS1								1.8	1.4	1.7
rSS2									1.2	1.4
rTh										1.3
rCPu										

2 weeks

	lM1/M2	lSS1	lSS2	lTh	lCPu	rM1/M2	rSS1	rSS2	rTh	rCPu
lM1/M2		1.4	1.1	1.1	1.4	1.8	1.2	1.0	1.0	1.4
lSS1			1.7	1.2	1.5	1.3	1.4	1.3	1.1	1.3
lSS2				1.2	1.4	1.1	1.1	1.1	1.0	1.1
lTh					1.2	1.1	1.1	1.0	1.6	1.1
lCPu						1.5	1.1	1.0	1.1	1.3
rM1/M2							1.4	1.1	1.1	1.5
rSS1								1.6	1.3	1.6
rSS2									1.2	1.3
rTh										1.2
rCPu										

6 weeks

	lM1/M2	lSS1	lSS2	lTh	lCPu	rM1/M2	rSS1	rSS2	rTh	rCPu
lM1/M2		1.6	1.1	1.2	1.3	2.0	1.5	1.2	1.3	1.3
lSS1			1.6	1.5	1.7	1.4	1.5	1.2	1.4	1.3
lSS2				1.2	1.5	1.0	1.2	1.1	1.1	1.1
lTh					1.4	1.2	1.2	1.1	1.7	1.2
lCPu						1.2	1.3	1.1	1.3	1.3
rM1/M2							1.6	1.2	1.3	1.4
rSS1								1.6	1.4	1.7
rSS2									1.2	1.5
rTh										1.4
rCPu										

12 weeks

	lM1/M2	lSS1	lSS2	lTh	lCPu	rM1/M2	rSS1	rSS2	rTh	rCPu
lM1/M2		1.6	1.3	1.1	1.3	2.3	1.4	1.5	1.1	1.3
lSS1			1.7	1.2	1.4	1.5	1.7	1.6	1.2	1.4
lSS2				1.2	1.4	1.2	1.3	1.5	1.1	1.3
lTh					1.3	1.1	1.0	1.2	1.9	1.2
lCPu						1.3	1.2	1.3	1.2	1.7
rM1/M2							1.3	1.4	1.1	1.3
rSS1								1.5	1.1	1.3
rSS2									1.2	1.4
rTh										1.2
rCPu										

Pre-stroke → week 2

Pre-stroke → week 6

Pre-stroke → week 12

Figure 3.16: Results from the bilateral functional data analysis for the control group. A) The correlation strengths are visualized color-coded with dark red being the highest correlation and dark blue the lowest. Each matrix mirrors the correlation values in colors and numbers. The two matrices on top represent the first two time point measurements, the two below the later measurements. At first sight, there is no evident change in correlation strength through the whole observation period. B) Significant connectivity changes are represented over a coronal template. Increases in connectivity become evident when looking at the values of z-score. N=15, animals with negative z-scores have been excluded from the analysis.

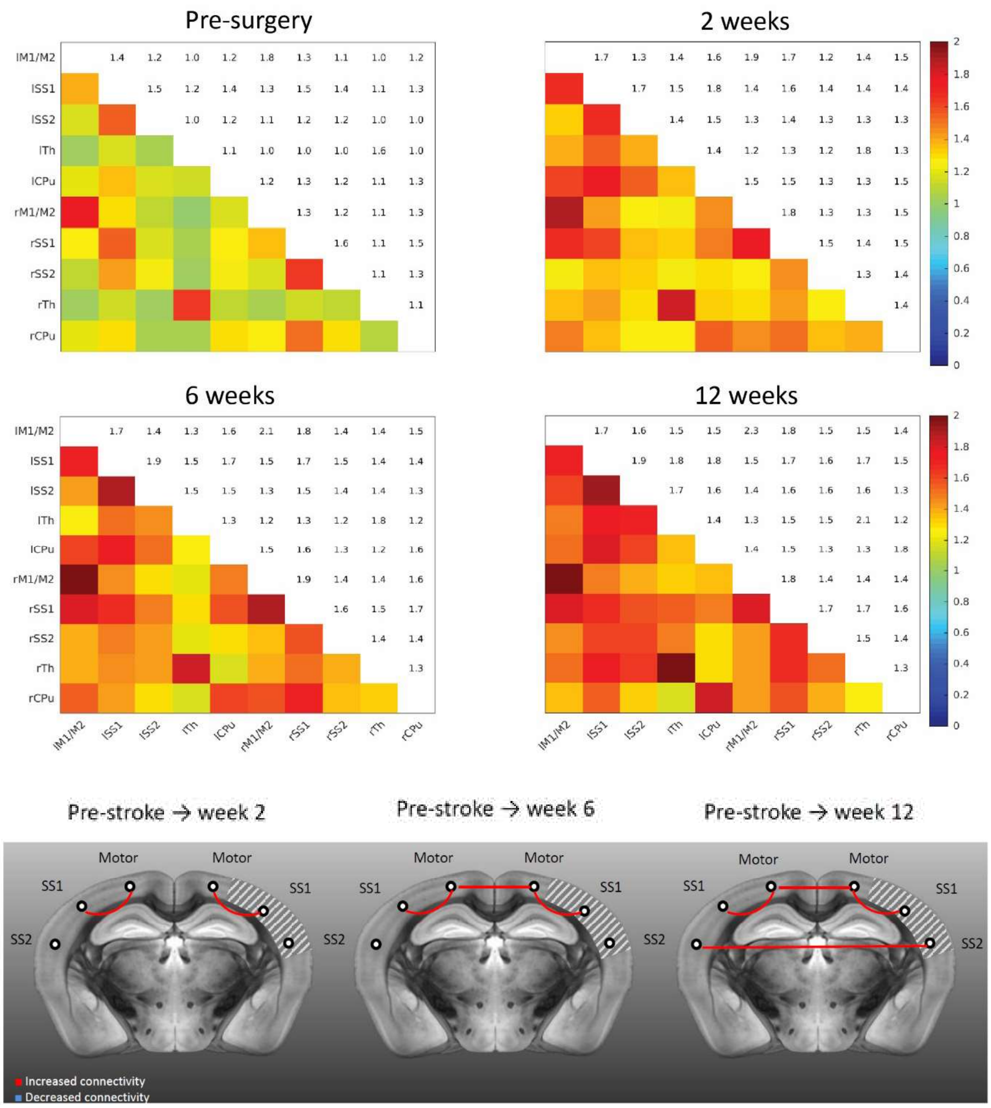

Pre-surgery

	lM1/M2	lSS1	lSS2	lTh	lCPu	rM1/M2	rSS1	rSS2	rTh	rCPu
lM1/M2		1.4	1.2	1.0	1.2	1.8	1.3	1.1	1.0	1.2
lSS1			1.5	1.2	1.4	1.3	1.5	1.4	1.1	1.3
lSS2				1.0	1.2	1.1	1.2	1.2	1.0	1.0
lTh					1.1	1.0	1.0	1.0	1.6	1.0
lCPu						1.2	1.3	1.2	1.1	1.3
rM1/M2							1.3	1.2	1.1	1.3
rSS1								1.6	1.1	1.5
rSS2									1.1	1.3
rTh										1.1
rCPu										

2 weeks

	lM1/M2	lSS1	lSS2	lTh	lCPu	rM1/M2	rSS1	rSS2	rTh	rCPu
lM1/M2		1.7	1.3	1.4	1.6	1.9	1.7	1.2	1.4	1.5
lSS1			1.7	1.5	1.8	1.4	1.6	1.4	1.4	1.4
lSS2				1.4	1.5	1.3	1.4	1.3	1.3	1.3
lTh					1.4	1.2	1.3	1.2	1.8	1.3
lCPu						1.5	1.5	1.3	1.3	1.5
rM1/M2							1.8	1.3	1.3	1.5
rSS1								1.5	1.4	1.5
rSS2									1.3	1.4
rTh										1.4
rCPu										

6 weeks

	lM1/M2	lSS1	lSS2	lTh	lCPu	rM1/M2	rSS1	rSS2	rTh	rCPu
lM1/M2		1.7	1.4	1.3	1.6	2.1	1.8	1.4	1.4	1.5
lSS1			1.9	1.5	1.7	1.5	1.7	1.5	1.4	1.4
lSS2				1.5	1.5	1.3	1.5	1.4	1.4	1.3
lTh					1.3	1.2	1.3	1.2	1.8	1.2
lCPu						1.5	1.6	1.3	1.2	1.6
rM1/M2							1.9	1.4	1.4	1.6
rSS1								1.6	1.5	1.7
rSS2									1.4	1.4
rTh										1.3
rCPu										

12 weeks

	lM1/M2	lSS1	lSS2	lTh	lCPu	rM1/M2	rSS1	rSS2	rTh	rCPu
lM1/M2		1.7	1.6	1.5	1.5	2.3	1.8	1.5	1.5	1.4
lSS1			1.9	1.8	1.8	1.5	1.7	1.6	1.7	1.5
lSS2				1.7	1.6	1.4	1.6	1.6	1.6	1.3
lTh					1.4	1.3	1.5	1.5	2.1	1.2
lCPu						1.4	1.5	1.3	1.3	1.8
rM1/M2							1.8	1.4	1.4	1.4
rSS1								1.7	1.7	1.6
rSS2									1.5	1.4
rTh										1.3
rCPu										

Figure 3.17: Results from the bilateral functional data analysis for the dMCAO group. A) The correlation strengths are visualized color-coded with dark red being the highest correlation and dark blue the lowest. Each matrix mirrors the correlation values in colors and numbers. The two matrices on top represent the first two time point measurements, the two below the later measurements. At first sight, the connectivity seems to gain strength after stroke and increases gradually through the whole observation period. B) Significant connectivity changes are represented over a coronal template. Increases in connectivity become evident when looking at the values of z-score. N=17, animals with negative z-scores have been excluded from the analysis.

1. After two weeks there is an increase in intrahemispheric correlation factors between the motor and primary somatosensory cortex for both hemispheres.
2. After six weeks, the above mentioned changes remain and an additional increase in the correlation between the transhemispheric motor cortices can be observed.
3. After 12 weeks, the already mentioned increased correlations persist, and yet another increased correlation can be perceived between the secondary somatosensory cortices of both hemispheres.

3.3.5 Fractional Anisotropy analysis

The FA values were calculated for the ischemic cohort for the following time points: pre-surgery, 2 weeks, 6 weeks and 12 weeks. I selected a region of interest in the ipsilesional hemisphere, a manually defined area of 7.48 mm^3 located within the cortical tissue affected by the ischemic changes, as noticed on the second week after stroke. The location of such ROI was kept constant for the rest of the time points and the FA values for each ROI were compared to the values of a mirrored ROI in the contralesional left hemisphere, which is considered the healthy reference where the FA remain unchanged.

In Figure 3.18 the FA values for the ipsi- and contralesional side are depicted in a bar graph with standard deviations. Focusing on the healthy side, we observe that there are no timewise significant changes in anisotropy values in comparison to pre-surgery status. Now, the FA values of the region of interest in the ischemic affected side drops dramatically after stroke, displaying a minimum value at the second week. The mean value for the right hemisphere ROI recovers above the aforementioned minimum, however still below baseline at week number six. Finally on the 12th week, the FA mean value continue rising compared to the 2nd week to a point in which there is no statistical difference compared to baseline.

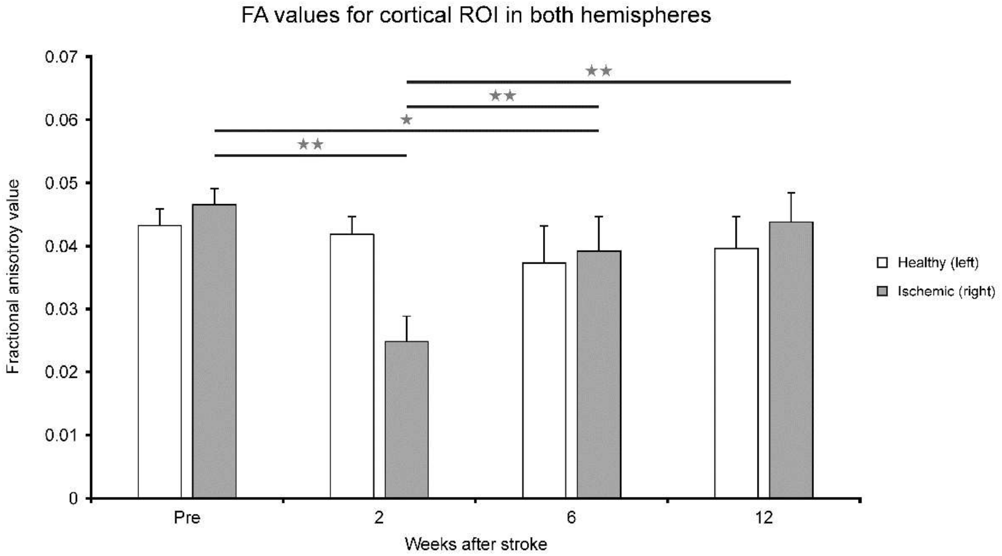

Figure 3.18: Mean Fractional Anisotropy values in a cortical region of interest for the ischemic group for all time points. The selected region of interest in located in the ischemia-affected area of the cortex, the control values are taken from a mirrored ROI in the contralesional "healthy" cortex. N=8; one star $p<0.05$; two stars $p<0.005$.

3.4 SUMMARY OF OBSERVATIONS

Taken together, all the results of the dMCAO model characterization imply permanent and developing alterations in the anatomy, histology and functional connectivity of the affected brain as well as in the behavioral performance of the mouse, in particular:

1. Resolution of the vast majority of the edema starting at 2 weeks after ischemia evidenced by decreased hyperintensity signal in MRI images.
2. Loss in cortical tissue volume in the ipsilesional hemisphere.
3. Mild shift in the brain midline compared to other stroke models
4. A change in cortical thickness where the edema develops in the first days after stroke.
5. An alteration in the morphology of the corpus callosum in the ipsilesional hemisphere.
6. A disorganization of the cellular architecture in the above mentioned shrunk cortex.
7. A mild enlargement of the CA area of the hippocampus.

8. Recruitment of astrocytes and microglia to the edematous area after stroke.
9. Resolution of astrocyte and microglia recruitment in areas beyond the region directly adjacent to the electrocoagulated artery and its surroundings.
10. Persistence of both cell types in the tissue closest to the electrocoagulation spot.
11. Changes in mNDS test observed in the motor and sensorial categories .
12. Deterioration in motor performance after stroke persisting to the second week, as evidenced by the Rotating beam test.
13. Worsening of motor coordination abilities after stroke as shown by the Rotarod test.
14. Increase in connectivity correlation factors compared to baseline in the sham occlusion cohort, as follows:
    a. Week 12: Left M to right M, left SS1 to right SS1, left SS2 to right SS2 (transhemispheric connectivities) and left M to left SS1 (contralateral to the sham occluded site).
15. Increase in connectivity correlation factors compared to baseline in the ischemic cohort, as follows:
    a. Week 2: Left M to left SS1, right M to right SS1.
    b. Week 6: Left M to left SS1, right M to right SS1, left M to right M.
    c. Week 12: Left M to left SS1, right M to right SS1, left M to right M, left SS2 to right SS2.
16. Decrease in fractional anisotropy values after stroke for a selected ROI in the ipsilateral hemisphere compared to baseline. Gradual recovery of such values until the end of the observation period at 12 weeks reaching pre-surgery status.
17. No changes in FA values for the contralesional “healthy” hemisphere through the entire observation period.

3.5 Discussion

In the subcortical only ischemic lesions, the initial relaxation time increase on T2 maps after transient filament MCAO decreases fast within one week and is completely resolved after 10 weeks. The fact that the T2 values go back to baseline does not necessarily mean that the tissue is recovered. In the filament model, necrosis and gliosis with a pronounced inflammatory reaction were observed already 2 weeks after ischemia (Wegener et al., 2005). In our permanent distal MCAO model, T2 values also revert to baseline appearance even before 2 weeks, since the 2 weeks time point TurboRare scan shows a marked decrease in hyperintense signal corresponding to the edema caused by the ischemia. We did not scan the animal on the same day as the stroke was induced nor on the following day, to minimize the stress induced by the transport from the animal house and the anesthesia session. Therefore, our earliest evidence of lesion size happened at 2 days after surgery, when the edema is clearly recognizable in the cortex of all subjects. While the initial increase in relaxation times reverts to baseline mostly within the first two weeks, the morphological changes that are a consequence of the lesion can start to be distinguished in this time point. The cortical thinning becomes more evident over the following weeks and by the end of the observation period – 12 weeks after stroke - it has reached a minimum in thickness. The cortex does not shrink inwards but on the contrary the lost volume is filled by subcortical tissue. In particular, the hippocampus enlarges and extends towards the lesion site, a morphological change that is evident for visual inspection at the 6th week time point and more pronounced on the 12th week. The corpus callosum also changes its morphology: instead of surrounding the hippocampus, it stretches towards the lesion site on the brain surface. Moreover, taking a closer look at the architecture of the cortical layers, we have observed that, at the end of our observation period, the more superficial layers are the ones that disappear, namely layers I, II and III. Cells from layer IV and V can barely be distinguished in a distorted architecture, but layer VI is mostly recognizable. The necrosis followed by abscess of tissue is more prominent on the superficial tissue reached by the MCA, whereas deeper layers seem preserved in spite of the initial edema that soaks them during the acute period after ischemia. Since the occlusion is permanent, the sparing of deeper tissue could be explained by a rapid angiogenesis surrounding the lesion starting as early as 12-24 hours after ischemia, a phenomenon extensively described elsewhere (Marti et al., 2000, Hayashi et al., 2003).

We have carefully searched in the available literature, yet none describes the morphological changes we have observed, presumably due to the fact that there are no studies covering beyond the acute or subacute period. Pena-Philippides and colleagues describe a reduction in infarct size after administration of PEMF treatment in an observation period of 21 days after stroke induced by dMCAO (Pena-Philippides et al., 2014). However the authors do not report any asymmetry in the brain structures, presumably due to the fact that the changes in hippocampus size can barely be distinguished at the second week after stroke, being more evident at the 4th week. Kuraoka and colleagues also fail to report such morphological changes in a study extending for 8 days that measures lesion volume with TTC staining. The same study reports the high reproducibility of infarct lesions and high survival rate for the model, results that are in accordance to our observations (Kuraoka et al., 2009). The loss in hyperintense signal is reported by Caballero-Garrido for the dMCAO model of stroke in mice, in a study extending for 3 weeks. Similarly, they do not report asymmetric changes in the brain structures, ending the experiment right on the edge of the hippocampus elongation start (Caballero-Garrido et al., 2015). The term “loss of tissue” is mentioned but not further investigated in two different reports from one lab (Herrmann et al., 2005, Lubjuhn et al., 2009). To our knowledge, our study is the first one to observe and report these permanent changes in the brain morphology including the 15% of tissue volume loss and the structural rearrangement of the hippocampus, corpus callosum and remaining cortex. Because of the careful design of our experiments and the presence of a sham occluded cohort for control, we can also conclude that the aforementioned changes are a consequence of the ischemia and not of the inflammation produced by the surgical procedure itself.

Endres and Dirnagl claim that mild ischemia models in rodents may be similar to transient ischemic attacks in man, particularly referring to the process of delayed neuronal cell death (Dirnagl, 2004). They also show that changes in T1/T2-weighted MR imaging 7 days after 15 min filament MCA occlusion in rats resemble those 7 to 10 days after transient ischemic attacks (TIA’s) in patients with known cardiogenic embolism. Based on these observations, the vast majority of stroke studies in rodents are performed using the filament model of MCAO. However they do not address the question of the stroke size after the transient filament MCAO, which actually give rise to massive focal strokes, which is in disagreement with the small size of most human strokes (Brott et al., 1989; Lyden et al., 1994). A step further into translational research involves mimicking the most frequent stroke size in the human. The development of primate and higher mammal stroke models is a desirable objective (Albers et al., 1999), however difficult to achieve due to the astronomic costs and breeding time it would entail, and more importantly the ethical dilemma about the performance of experiments in "superior mammals". For the dMCAO model to be extensively used, the structural rearrangements in the brain must be taken into account. Otherwise it could be wrongly assumed that the lesion resolves rapidly 2 weeks after stroke without further implications than the disappearing edematous tissue. In particular, functional connectivity is altered in later time points and further studies must be conducted to detect if such changes are a consequence to the structural rearrangements.

In the model characterized in my project, the occlusion is permanent. Previous studies with transient filament MCAO in our lab have shown two different lesion types in the rodent: either restricted to the caudoputamen (cp) or involving both cp and cortex (Wegener, 2005). Those animals presented different behavioral patterns; those with affected cortex had a loss in sensorimotor functions as opposed to those in which the cp alone was affected, a finding that is in coherence with my results. The subjects of my study had an exclusive cortical lesion and presented only sensorimotor behavioral loss. Few studies have reported behavior deficits of the dMCAO model and none has tested this model in Nude mice. Our results with behavior tests showed variable sensitivity to the ischemic impact. The results of the Corner Test clearly show that the Nude mouse strain is not appropriate for this test: the low density and short length of the mice vibrissae impact directly in its ability to recognize the walls of the test and therefore does not provide accurate information about sensorial ability of the snout. Rosell and colleagues report highly variable results of this test and other in other mouse strains (Rosell et al., 2013). The reason for such gap of knowledge in behavioral tests after dMCAO is that long term behavioral deficits (i.e. several weeks after surgery) are hard to detect in mice. This could be due not only to a high level of recovery in these species but more presumably to a low sensitivity of the behavioral testing (Freret et al., 2009). This statement is in accordance with our results of the Rotating Beam test, where our cohort of mice showed a decrease in the performance of the time points chosen after stroke but no further information could be extracted about the severity of the deficit or a short term recovery. We did not test for mnesic deficits mainly because other studies have reported no changes after dMCAO (Freret et al., 2009). McGill and colleagues reported that the cylinder test was not sufficiently sensitive to detect sensorimotor asymmetry even performed 3 days after the occlusion (McGill et al., 2005). However, I decided to test for motor deficit using a test that involves the exhausting capacity of keeping the balance on an accelerating rod: the Rotarod. We obtained highly significant differences when comparing the performance of the cohort that underwent stroke, before and one week after surgery. The sham occluded control group did not show any modifications in the performance, meaning that the surgery procedure is not affecting the mouse's fitness, but the ischemic changes are.

We have shown that inflammatory response to the ischemia induced by the dMCAO starts with a massive recruitment of microglia to the ischemia-affected tissue, which can be observed 48 hours after stroke onset. Such reaction persists over time during the entire observation period of 12 weeks, however the territory where the microglia can be found shrinks together with the cortical tissue and condenses to the site where the forceps touch the brain surface. The observed inflammatory response is to be expected: stroke induced microglial activation causes release of a variety of inflammatory mediators many of which are cytotoxic or cytoprotective (Wood, 1995). Phagocytosis of cellular debris resulting from necrotic digestion of parenchyma after blood deprivation along with the release of anti-inflammatory cytokines by microglia occurs in an effort to restore tissue homeostasis. In time, this attenuates the detrimental effects of inflammation and aids in tissue repair. Our findings report the longitudinal fate of such activated microglia, showing that they decrease in number and focus their presence around the tissue that has suffered the most damage: ischemia and mechanical manipulation by the electrocoagulation forceps. Reactive astrogliosis (Sofroniew and Vinters, 2010) is defined as the process that induces proliferation of astrocytes and increases their GFAP levels. Because they are less vulnerable to glutamate excitotoxicity than neurons, it is not surprising to find – surviving – astrocytes in the area mostly affected by ischemia where neurons are necrotic, shortly after stroke i.e. 48 hours after dMCAO as shown in our results. Susarla and colleagues report that reactive astrocytes in the cortex start proliferating 3-5 days after injury and place themselves in areas surrounding severe focal lesions (Susarla et al., 2014). This statement is in accordance with our findings beyond the first week after stroke: we found focally recruited GFAP positive cells closely surrounding the lesion site, becoming more concentrated over time. These changes can result in reorganization of tissue architecture without the formation of dense narrow and compact barriers, as in glial scars (Shimada et al., 2011). Finally, in the early stages after stroke, I have demonstrated that astrocytes can be densely found in the deep cortical layers, adjacent to the corpus callosum. This in an interesting finding because it relates the presence of astrocytes in the same territory where the cortical layers are preserved as stated in the above paragraphs, presumably due to the angiogenesis-enabling properties of astrocytes. Several factors secreted by astrocytic cells such as TGFβ, glial derived neurotrophic factor (GDNF), basic fibroblast growth factor (bFGF) and angioprotein 1 (Ang1) stimulate the production of new blood vessels and the proliferation of endothelial progenitor cells (Cross et al., 2001, Babei et al., 2003, Wuestefeld et al., 2012).

The focal ischemic lesion leads to a localized increase in the sensorimotor connectivity network. Within the first two weeks after stroke, it mainly affects the connectivity between the primary somatosensory and motor cortices, in both ipsi- and contralesional hemispheres. Although the cortico-thalamic circuitry and the caudate putamen associations to the cortex were also included in the analysis, I focused on the gross seed regions located in the tissue irrigated by the MCA and on the motor cortex. The greatest surprise within the current data was the marked and gradual increases in connectivity among somatosensory and motor cortices in both hemispheres, reflected in cross-correlations between seeds. Harris and colleagues have observed hyperconnectivity levels in somatosensory and cortical regions after traumatic brain injury persisting for 4 weeks. This increase may possibly indicate some residual potential for reorganization in these regions, although this may not explain the mirrored results observed in the contralateral hemisphere (Harris et al., 2016). In order to claim that the increases in connectivity are a consequence of the ischemic changes, the mice cohort that was sham operated should not show identical results. In accordance to this statement, results in our sham occluded group show a mild increase in transhemispheric connectivities starting at week 12 after surgery, and no changes to report before that time point. Since the inflammatory and structural changes in this group are minimal to non-existent, it can be suggested that the accumulation of inflammatory cytokines over a threshold can trigger late variations in the connectivity network. This is one possible explanation for the observed phenomenon, provided that the sham occlusion and concomitant disruption of the blood brain-barrier activate the inflammatory response in a slow and cumulative fashion.

The relationship between functional connectivity (temporal coherence) and the physiological basis of the BOLD signal are complex, taking into account the multidimensional pathological changes that can occur following brain damage (e.g., alterations on cerebral blood flow, oxidative metabolism, neuronal firing and sodium channels). A research group with extensive experience in resting state analysis in pathological brains reports hyperconnectivity patterns in sensory-motor regions in multiple sclerosis patients (Hillary et al., 2015). They observe large consistency between the hyperconnectivity observed in their studies – including other brain pathologies – and clinical fMRI studies of mean signal change (amplitude) revealing neural recruitment in clinical samples (see also Hillary, 2008; and Hillary, 2006). Another issue to consider when interpreting literature focused on network connectivity has to do with the mechanism of action of neural connections. With respect to such mechanism of action in the connections observed in the time series data in the aforementioned research group, the BOLD signal cannot decipher between the various inputs including excitatory and inhibitory sources. Therefore, the increased synchronization between selected regions can be interpreted as increased involvement of the network, but little can be said about the nature of that involvement (Hillary et al., 2015). It should be noted that there is significant evidence in studies using electrophysiological methods supporting the hyperconnectivity findings in fMRI (Castellanos et al., 2010, Tijms et al., 2013). In light of this evidence, and because the neurovascular methods are not able to clarify the nature of the neural activity, it is unlikely that the hyperconnectivity results can be explained as a vascular anomaly alone decoupling it from neuronal signaling.

It is improbable that increased connectivity occurs in isolation, instead a combination of gain and loss is expressed throughout the network. As a consequence of applying a threshold and selecting few seed ROIs, we may have missed eventual less intense decreases in connectivity, or significant losses beyond the observed cortical areas. I conclude that the most logical explanation for the increases observed in my study is that it is a compensatory response, meaning a nonspecific increase in neural resource use operating as a buffer against network disruption.

4

Chapter 4

Neural stem cell implantation as a therapeutic strategy for cortical ischemic stroke

4.1 AIM

Cell therapy may provide a promising new treatment for stroke, reducing stroke-related disability. Further investigation is needed to determine specific effects of cell therapy and to optimize cell delivery methods, cell dosing, type of cells used, timing of delivery, infarct size and location of infarct that are likely to benefit from cell therapy (Kenmuir and Wechsler, 2017).

In an attempt to shed more light on some of the above mentioned experimental settings, I conducted a longitudinal experiment of neural stem cell implantation in an ischemic brain, after characterizing the lesion thoroughly (see the previous chapter). I was particularly interested in investigating the therapeutic power of the neural stem cell engraftment in the ischemic brain, implanting it outside of the ischemic area as opposed to previous studies in which the graft is implanted in the penumbra area of the stroke (Boehm-Sturm et al., 2013). To date, the study of cell therapy in stroke models has mainly been limited to *in vitro*, *ex vivo* and behavioral assessments. Therefore, much effort was invested in elucidating the behavior of the cells *in vivo* throughout the 3 months period of the experiment duration. In our lab, we have the adequate imaging tools to follow the viability of the graft and its influence on the functional connectivity of the tissues, *in vivo*.

4.2 EXPERIMENTAL DESIGN

Same as for the characterization of dMCAO described in the previous chapter, the study was designed to obtain the largest amount of meaningful data with the least amount of interventions on the animal, as each measurement is considered a source of stress for the mouse due to the anesthesia induction. For comparison purposes, many of the assessments done in the dMCAO characterization were repeated in this study and more tests were added to the basic battery in order to monitor the cells *in vivo*. The viability of the cells was carefully followed up, very frequently directly after cell implantation when the most amount of cells could be lost. In this regard, two BLI measurements were performed per week during the first two weeks after implantation, one per week during the 3 weeks following that, and once every second week for the rest of the experimental weeks.

Behavioral assessment was extended beyond the second week after stroke and also performed every second week in the latest time points. Resting state fMRI measurements were synchronized with the previous study to have the same data point for comparison: pre-surgery, two, six and twelve weeks after stroke (one, five and eleven weeks after cell implantation, respectively). To supplement our imaging assessments, the research group of Dr. Schwartz in the University Hospital of Bonn (Germany) chemically cleared the brain of some of our subjects and performed LFSM analysis right after the last MRI measurement at 12 weeks. Moreover, the research group of Prof. Dr. Kloppenburg in the Institute for Zoology from the University of Cologne, agreed to perform electrophysiological measurements in the engrafted cells in the brain cortex for some of our subjects at the end of the study, slightly delayed beyond the last MRI measurement, at 16 weeks after stroke.

As performed with all experiments, I included MRI sessions before surgeries for baseline images of the brain and behavioral tests to obtain baseline values. The timeline of experiments is loaded with assessments, it consists of a similar experimental design to the characterization of dMCAO plus frequent BLI evaluations, extended behavioral testing (although only one test was chosen for this study, see section 4.3.3 for further details), electrophysiology and LSFM.

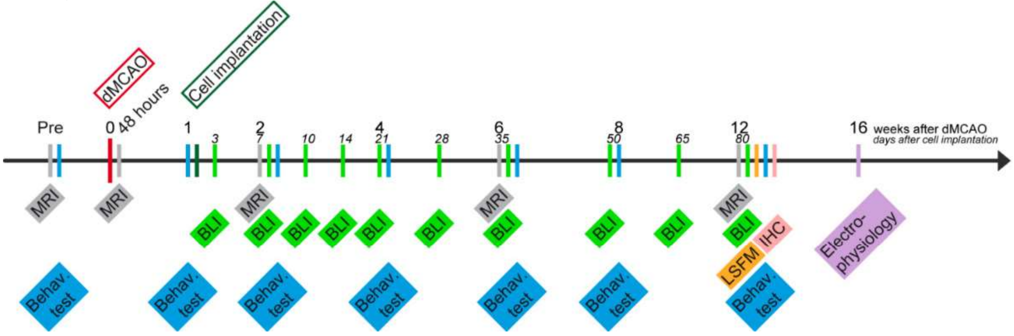

Figure 4.1: Schematic of the experimental protocol. Outline of experimental design for the cohort of mice with dMCAO and cell implantation. The control group was similarly designed, without the dMCAO surgery and behavioral assessments. The time unit is set to ‘weeks’ after dMCAO and on parallel to ‘days after cells implantation’ in italic and with a smaller font size.

The control group for this study consisted of a cohort of mice of the same age and weight, implanted with the same amount and type of cells, but without having any surgery for stroke induction, not even a sham occlusion. In this regard, the implantation of cells happened in a “healthy” or naïve brain. It is important to point out that only the control group was exposed to all the BLI measurements described in the above paragraph. I performed three less BLI sessions in the mice that had the ischemia, reducing the amount of stress and anesthesia they were exposed to in the first weeks, the acute period. There was no measurement at 10, 14 and 28 days after cell implantation for this group.

In Figure 4.1 I have drawn a detailed timeline of procedures applied to the subjects. Note the double labeling for the axis, due to the double surgeries: dMCAO and cell implantation. On the upper row, the weeks after dMCAO can be read, on the lower row, the days after cell implantation are explained which entail a one week delay related to the dMCAO.

Choosing the timing of cell engraftment at one week after ischemic onset was a decision made envisioning a future collaboration with the Lund Stem Cell Center in Sweden and based on a study performed by Oki and colleagues, where the group implanted the stem cells one week after stroke (Oki et al., 2012). By choosing an identical experimental set up, the reproducibility and comparison of results is eased. Please refer to the following chapter for further details about such collaboration.

The site of cell engraftment was chosen to be outside of the edematous tissue shown 48 hours after stroke in MRI measurements in an attempt to keep the cells as close as possible to the lesion, however far enough to avoid a premature cellular loss due to the neurotoxic effect of necrotic factors secreted by the dying nutrition-deprived neurons. A recent study in our lab by Dr. Green (Green et al., 2018) had shown the decrease in cell viability when implanting the graft adjacent to the lesion produced by the filament model of MCAO where the ischemic areas are bigger in size compared to my model. It was my objective to also determine if the size of the lesion – edema affects viability of the graft.

The amount of implanted cells was carefully chosen taking into consideration previous studies from our research group, in particular from experiments performed by my colleague Dr. Stefanie Vogel (Vogel et al., 2018).

Before beginning the experiments in this cohort, several tests were performed to sort out the best experimental details of the implantation surgery. I tested for the depth of cortical implantation in which the cells remain in the cortex and do not diffuse along the corpus callosum, I also tested for a minimally invasive injection of cells with two different needle gauges that would allow implantation without clogging the device with cells.

4.3 Results

4.3.1 Bioluminescence imaging

Given the fact that the implanted stem cells are genetically modified to express Luciferase constitutively, as long as they remain alive the housekeeping mechanism of the cell will allow for a steady production of the enzyme. I could closely inspect if the graft was still viable throughout the entire period of the longitudinal study, starting as early as 3 days after implantation. I considered it unnecessary to expose the animal to an anesthesia session before that time due to the stress and poor acute state produced by the cell implantation surgery.

Animals were imaged in groups of two or three to find the subjects that would be most suitable to be measured next to each other: since signals were of different order of magnitude, not all animals could be randomly allocated to be scanned together, they had to be grouped depending on their signal amplitude with similar ones. In Figure 4.2 there is an example of 3 subjects being measured together, whose signal amplitude falls in the same order of magnitude, thus eligible to continue being scanned together.

Circular ROIs of the same size were drawn on top of the animal’s head where the signal was observed. An additional rectangular ROI contain-

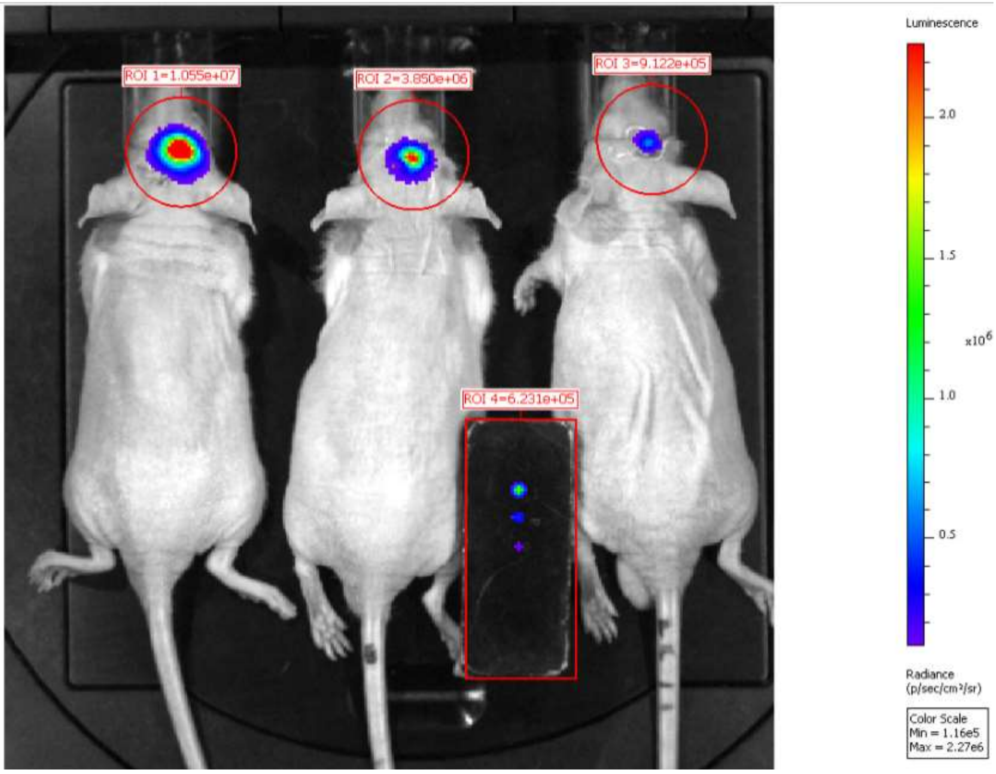

Figure 4.2: BLI signal acquisition snapshot. Example of 3 subjects with a different BLI signal intensity but on the same order of magnitude. The color scale depicts radiance in p/sec/cm^2/str and when the signal inside of a drawn circular ROI is measured, the units of the measured value is p/sec.

ing the total signal given by the standard was placed over the standard lid. Results were expressed as total flux in photons per seconds for each ROI. The standard signal was checked to be stable throughout the 30 minutes of measurement and to discard major fluctuations in the acquired signal, however it was not used to standardize the subject's signal.

13 of the 14 subjects from the "cells in ischemic brain" group showed clear signal starting from the first day of measurement. All 9 subjects from the control group which entailed implanted cells in a naïve environment showed signal during the first measurement too.

The signal magnitude for each subject was very heterogeneous in amplitude. Plotting the signal of all 13 subjects in the same graph did not allow a clear visualization of each animal's signal dynamic, as shown in Figure 4.3. From this plot I was able to inspect each curve individually for the

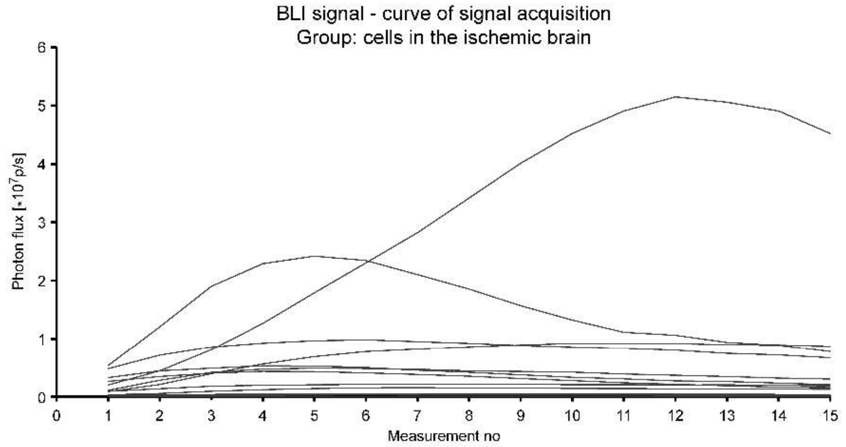

Figure 4.3: BLI signal acquisition dynamics. Individual signal dynamics during the 30 minutes of signal acquisition (1 measurement every 2 minutes). The 14 different subjects have not been color coded since it is not the purpose of this graph to identify them, but to show them as a pool of signals.

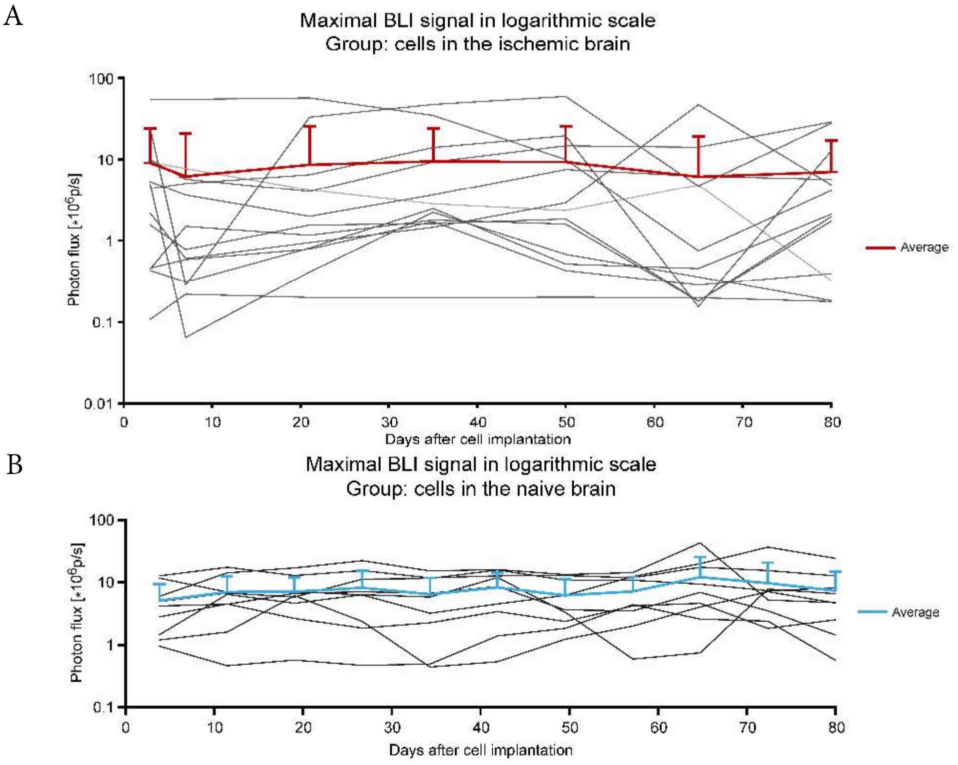

Figure 4.4: Maximal BLI signal in a logarithmic scale. Individual and average (A in red, B in blue) maximum values for all time points during the 11 weeks. The individual values show positive and negative timewise variations, yet the average cancels them out and the result is a steady signal.

dynamics of luciferase activity and maximum peak, and the resulting value was extracted from each animal for each time point to generate a different dataset as shown in Figure 4.4A, using a logarithmic scale to avoid smashing all lower values next to the x-axis. Figure 4.4B displays the maximum values of photon emission for each subject and time point for the control group "Cell in a naïve environment". The average of measurements for all animals on the same measurement day was calculated and plotted together with its standard deviation in the graphs of Figure 4.4, the average values are highlighted in color against the individual values in gray. Results show that BLI signal glows in the same order of magnitude for most of the subjects and also remains within the same order of magnitude over time, for each subject. There were few exceptions in which the order of magnitude of the obtained BLI signal was not homogenous with the majority, these measurements were first repeated just in case of an experimental error – and the same values were obtained. These subjects that differ from the majority were still taken into account for the analyses, but data had to be analyzed differently (explained in the following paragraphs).

Because of the heterogeneity in orders of magnitude for photon emission for the different subjects, it made more sense to analyze the signal variation for each subject over time. For this purpose, I calculated the fold increase along the 11 weeks of observation for all animals and the results for

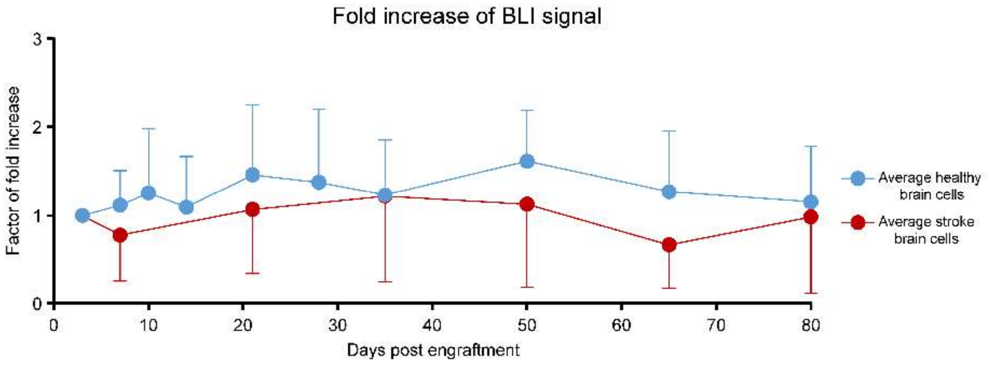

Figure 4.5: Net fold increase of BLI signal for all time points. For the purpose of comparison, the fold increase of BLI signal corresponding to both groups – 'cells' and 'stroke + cells' – is displayed in the same chart. No net increase of decrease compared to baseline values can be observed.

both groups are shown in Figure 4.5.

There is no statistical significance in the variations of the fold increase for any of the groups. This means that the signal does not decrease or increase during the entire observation period but stays constant.

4.3.2 Correlation between BLI signal intensity and graft size and location

As mentioned in the section above, the signal intensity of the different grafted animals was heterogeneous for the profile curves to be plotted raw in the same figure. An interesting point is that regardless of the graft size at the end of the observation period, the signal remained stable for every animal throughout the 11 weeks. This finding is shown in Figure 4.5 where the fold increases of BLI signal (or lack thereof) were calculated. Figure 4.6 illustrates a snapshot of BLI signal acquisition for 8 representative animals for all time points and a scaled picture of the graft found after perfusion. Here, the following findings are observed: the signal strength does not correlate to graft location (cortical surface vs. cortical depth) nor to the graft size (sleek vertical grafts vs chunky round grafts). The signal seems to correlate to a complex interaction of the aforementioned variables, however due to the absence of cell count assays the graft can only be qualitatively inspected for size.

4.3.3 Behavioral tests

Behavioral tests were applied only to the group of cell implantations in the ischemic brain. Having tested for the corner test in the dMCAO characterization group and having concluded that the model is not suitable for the test, I did not perform it again in the present group. Nor did I test for the Rotarod since one week after dMCAO the animals were undergoing another surgery and were not fit enough to perform on the same day of surgery to extract results for comparison with the “Stroke only” group. Therefore, only the Rotating Beam test was used to monitor for sensorimotor performance in this group.

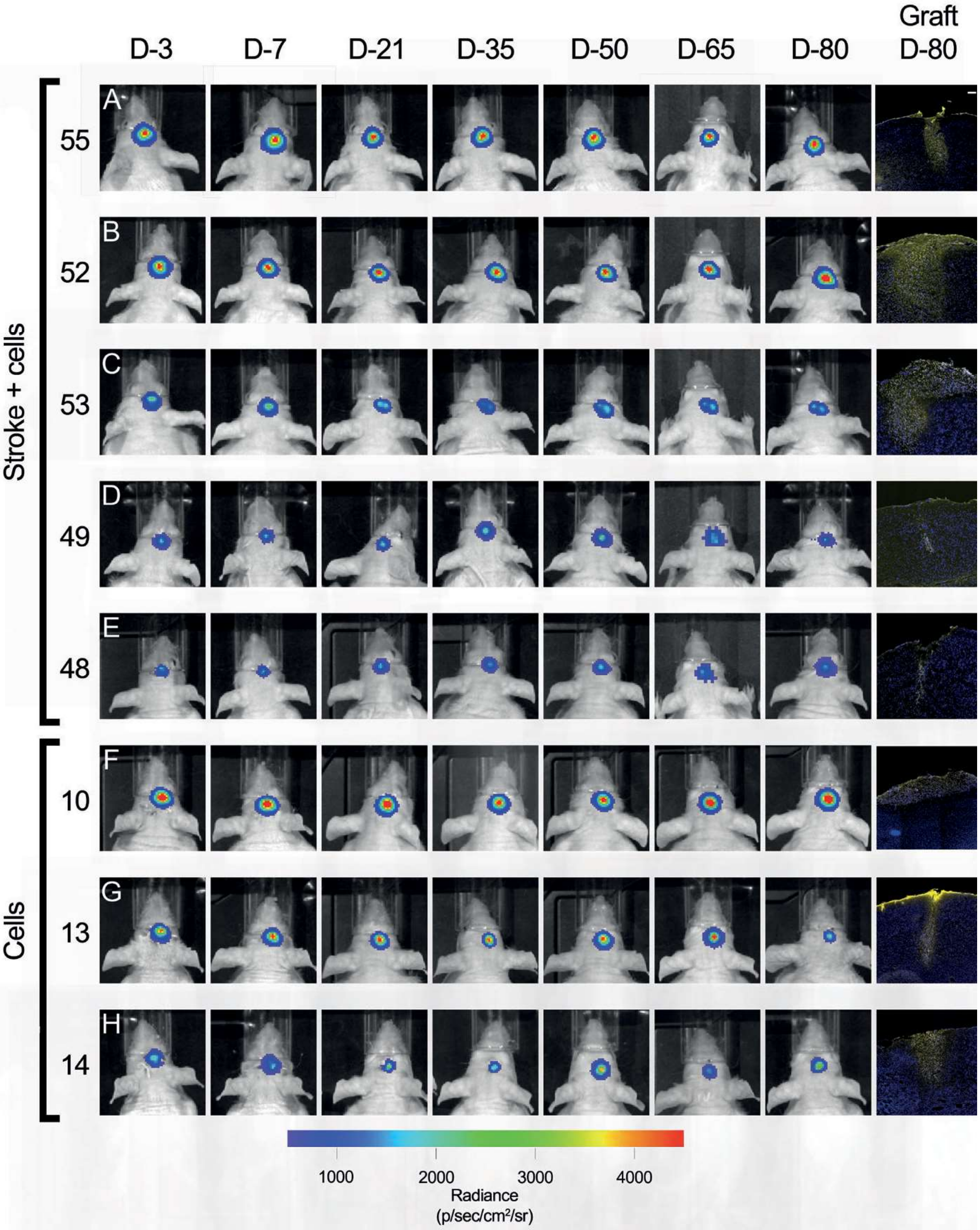

Figure 4.6: Timewise development of BLI signal intensity. Snapshots for all time points for 5 representative subjects of the 'stroke + cells' group and 3 subjects of the 'cells' group. The color bar is representative for subjects A, B, C, D, E and H. For animals F and G, in order to be able to observe the steady signal throughout the 80 days, the scale bar was modified to a max. of 2000 p/sec/cm^2/sr. Right column: size and location of the graft at the end of the observation period (12 weeks after stroke, 11 weeks after cell implantation). No correlation is observed between stroke size and amount of emitted photons.

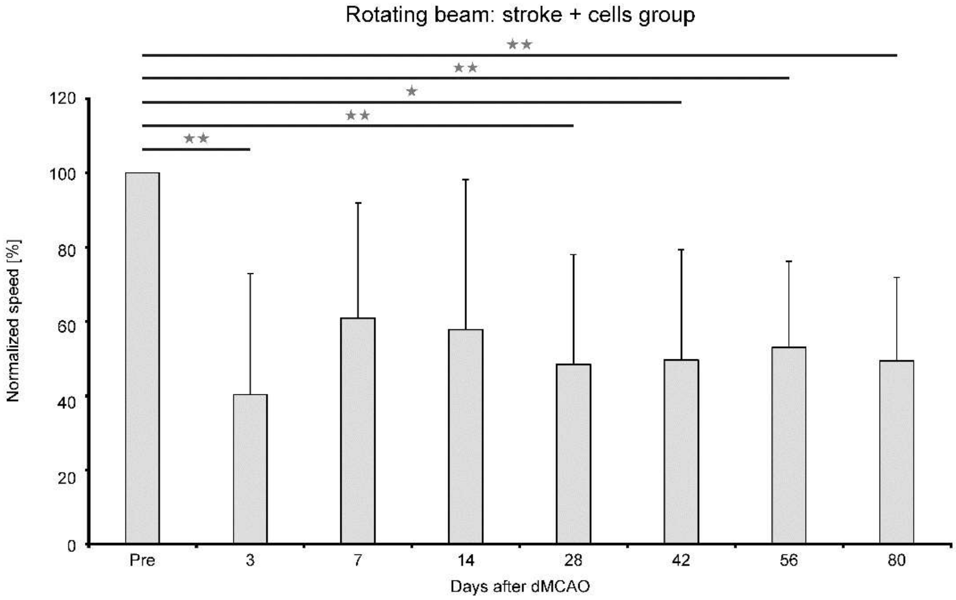

Figure 4.7: Behavioral test. The rotating beam test shows a significant performance reduction of the cohort 'stroke + cells' relative to the pre-surgeries situation, persisting at all time points until the end of the observation period, 12 weeks (80 days) after dMCAO. Cells were implanted on day 7 post dMCAO, after behavioral assessment. One star $p<0.05$; two stars $p<0.005$.

One of the 14 subjects had to be excluded since he could not be trained with the same amount of training sessions as the rest of the cohort. For the rest, they showed heterogeneous speeds at the end of the training period, so once more I decided to normalize the results to baseline values before dMCAO in order to be able to analyze them together and compare each normalized average to a theoretical mean of 100 using a one sample Student's t test.

Taking a look at Figure 4.7, the similarity between this group and the "dMCAO characterization cohort" from the last Chapter 3 can be shown at day 3 after ischemia. The difference between the randomly chosen mean=100 and normilized (to baseline) speed at day 3 is highly significant. Because of the wide distribution of the data (and high standard deviation values) there is no significance at day 7 and day 14 compared to baseline. High significance between the mean value and 100 is again found at day 28, 56 and 80. The significance for day 42 is not high, since the p-value = 0.006 and we have defined high significance below 0.005.

The results are evidencing a drop in performance after both surgeries, however difficult to interpret due to the complexity of the statistical analysis. Statistically, the drp at day 3 is significant, but not the decreases at day 7 and 14. It would make common sense to assume that the values for both of those time points are closer to the one in day 3, but the heterogeneity of the acquired data does not allow the satistical test to distinguish those means from 100.

4.3.4 IMMUNOHISTOCHEMISTRY

The ICH analysis for the groups containing grafted cells focused on the characterization of the graft and its immediate surroundings. To achieve this, it was necessary to identify the localization and shape of the graft, and to discriminate it from its surrounding cells, which was achieved through the Human Nuclei staining (HuNu).

The generation of new neurons was checked with NeuN antibody, which attaches specifically to the Fox3 protein and is a marker of maturing neuronal lineage (Gusel'nikova and Korzhevskiy 2015). Tissue sections from both groups were double stained for HuNu and NeuN. For all subjects the graft was clearly distinguishable from its surrounding environment, the graft's borders were easily recognized implying no diffusion of graft cells into the cortical tissue 12 weeks after ischemia.

Graft cell migration to remote areas of the brain or to the lesioned cortical tissue was absent. Interestingly, no cells with double expression of the markers HuNu (red) and NeuN (green) were identified within the cell graft. However, multiple mature neuronal cells were found in the close proximity of the graft's borders. Figure 4.8 depicts the images taken from 2 subjects of the "Cells in the naïve brain" group – Figure 4.8A a brain slice containing a sleek graft with almost no cells on the cortical surface, and Figure 4.8B a brain slice with a thicker graft – and one subject from the "Cells in the ischemic brain" group, Figure 4.8C. Nuclei from all cells were counterstained with DAPI (blue). The purple (red + blue) nuclei in the overlaid image rep-

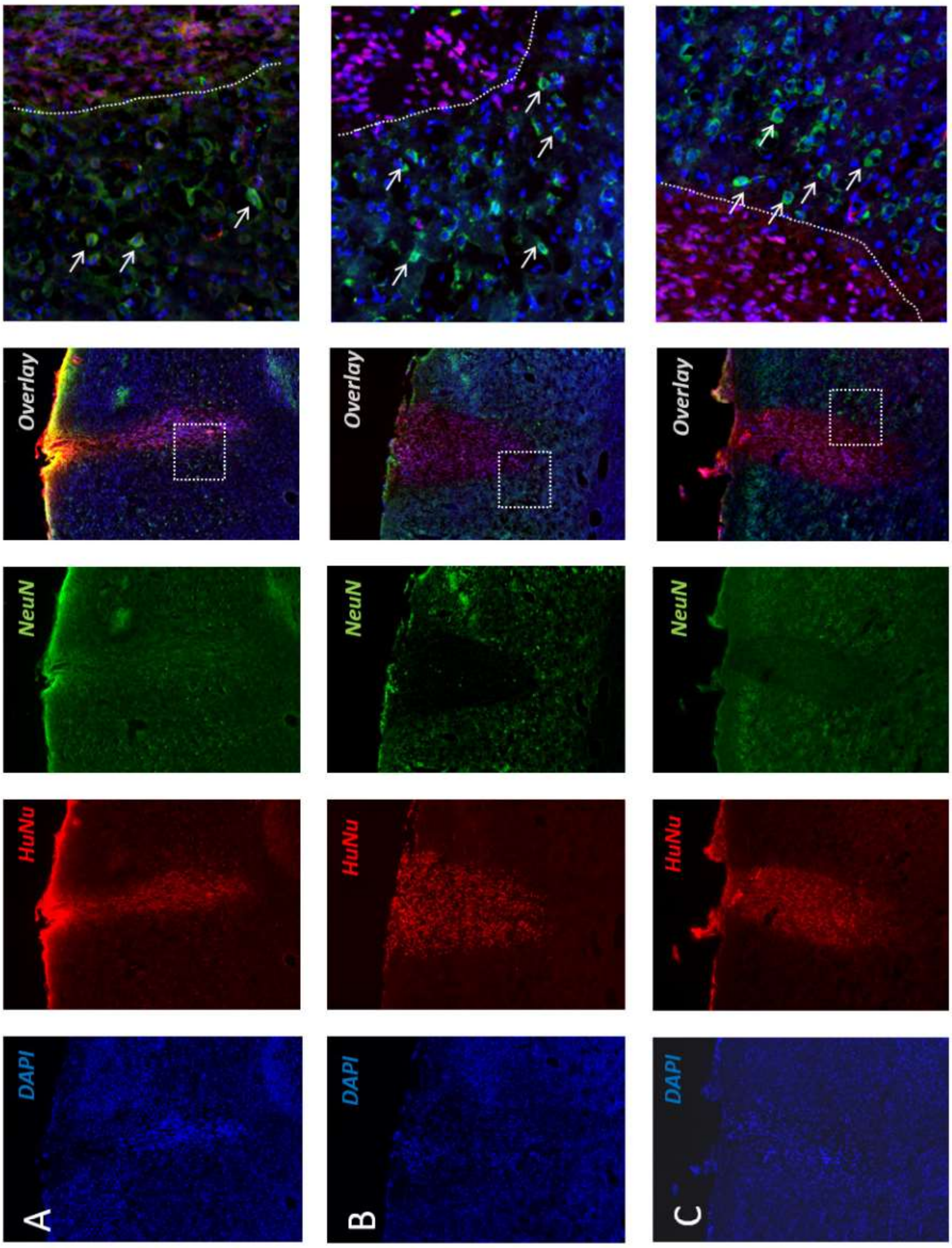

Figure 4.8: Immunohistochemical staining for graft location and new neurons. First column: blue channel, DAPI stain for cell nuclei. Second column: red channel, HuNu stain for the graft nuclei. Third column: green channel, NeuN stain for maturing neurons all over the cortex. Fourth column: overlay of all 3 channels. Fifth column: zoomed-in dashed square of the fourth panel. Dashed lines represent the border of the graft, white arrows point at NeuN positive cells.

resent the nuclei of the implanted cells. A close-up of the graft and its immediate surrounding is shown on the far right: The arrows point at some of the many cells with NeuN expression (green cytoplasm and blue nucleus); the dashed white line defines the border of the graft. As mentioned above, the NeuN positive cells did not originate from the graft.

The expression of GFP transfected into the genome was checked with anti-GFP antibodies. Although eGFP is a protein that emits photons at 510 nm after excitation at 488 nm, in our sections the tissue's autofluorescence signal at 510 nm was too high for any endogenous GFP signal from the graft to be detected. At 60x few eGFP positive cells were detected in the core of the graft and neurites were difficult to visualize. Therefore, we improved its detectability specifically staining with the antibody against the protein and exciting at a different wavelength. It is possible to see in Figure 4.9 the stained eGFP in green. At 60x, the neurites of the implanted cells protruding towards the surrounding tissue where they have been grafted can be noted. Such neurites are pointed with white arrows, regardless if the cells are located in the core (Figure 4.9A) or periphery (Figure 4.9B and 4.9C) of the graft.

Figure 4.9 shows a double staining for GFAP expression from astrocytic cells (in red) and eGFP expressed by the implanted cells (in green). A more careful inspection at 60x magnification shows no double expression in implanted cells, meaning that they are not expressing astrocytic markers. However, the implantation site is full of astrocytes, even if they are not originating from the eGFP-expressing implanted cells. This means that there is a strong astrocytic scar formation where the graft is sitting at the moment of perfusion.

The glial response after cell engraftment was further evidenced by staining the graft and its surroundings with anti-GFAP antibodies and checking if any of them originates from the implanted cells, which is possible to evidence staining with a marker that only and all the implanted cells would show. If some graft cells had differentiated into the astrocytic lineage, they would also be detectable combining the staining with HuNu (Figure 4.10). Images show a vast presence of astrocytic-like cells in the core of the graft and its borders through the entire extension of the implantation canal

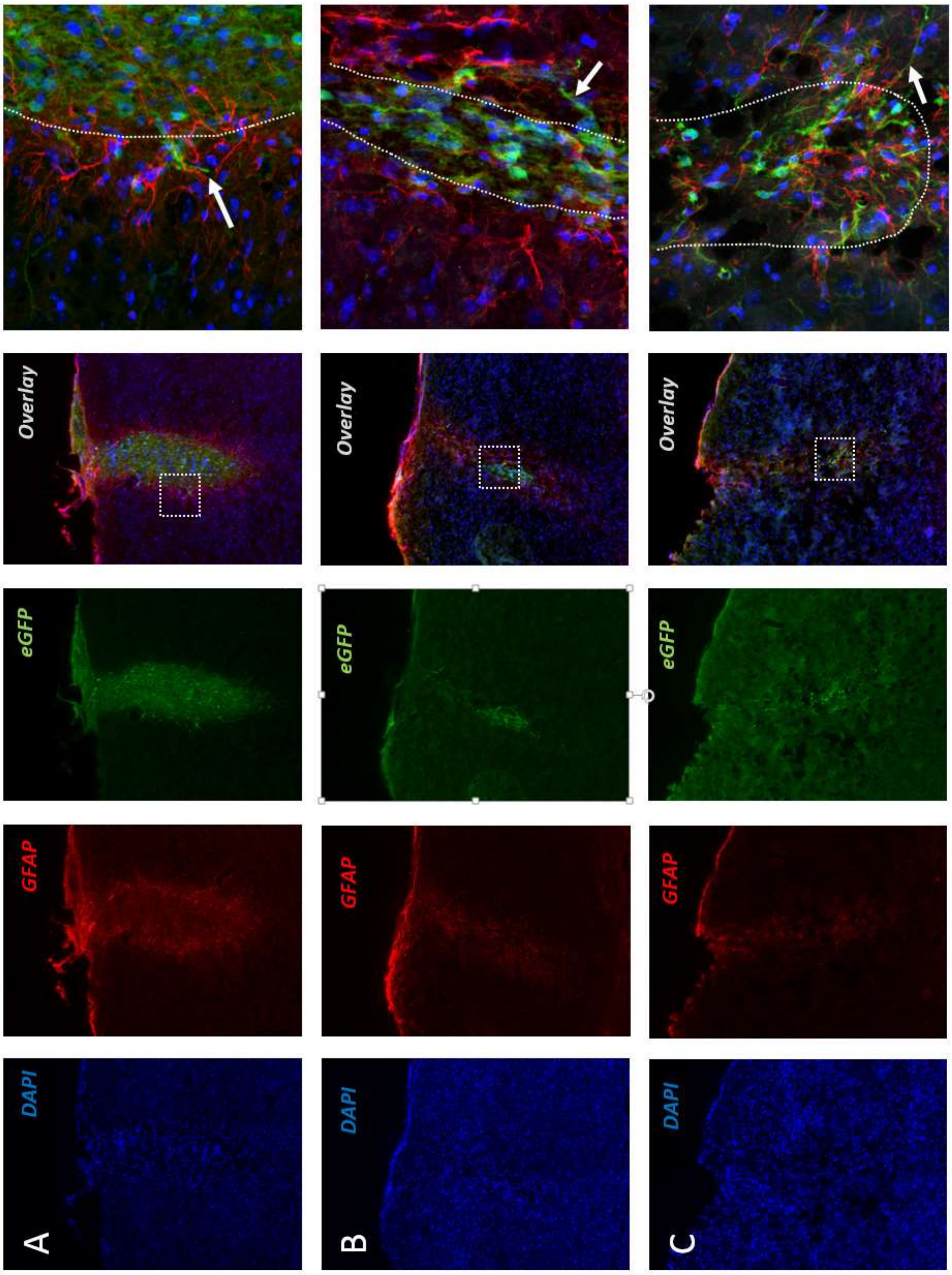

Figure 4.9: Immunohistochemical staining for engrafted cells morphology and gliosis. First column: blue channel, DAPI stain for cell nuclei. Second column: red channel, GFAP stain for the astrocytic cells. Third column: green channel, eGFP for endogenous expression of the graft GFP. Fourth column: overlay of 3 channels. Fifth column: zoomed in dashed square of the fourth panel. Dashed lines represent the border of the graft, white arrows point at projections outside the stem cell graft.

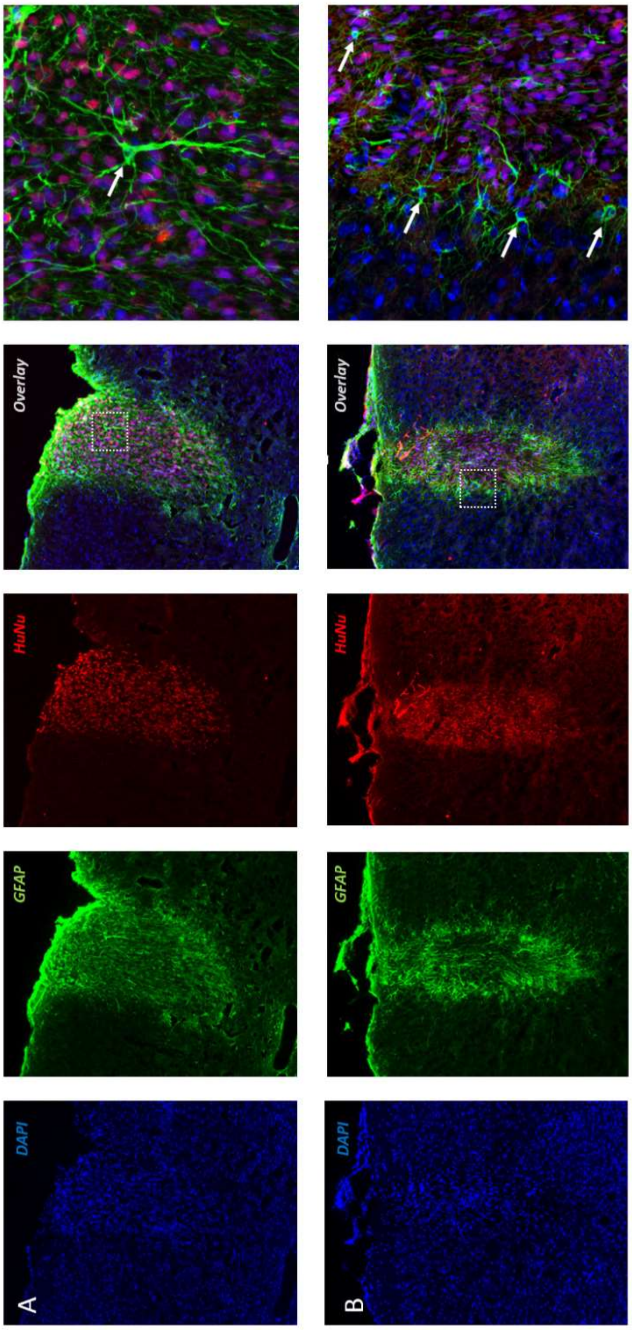

Figure 4.10: Immunohistochemical staining for graft location and gliosis. First column: blue channel, DAPI stain for cell nuclei. Second column: green channel, GFAP stain for the astrocytic cells. Third column: red channel, HuNu stain for the graft nuclei. Fourth column: overlay of 3 channels. Fifth column: zoomed in dashed square of the fourth panel. White arrows point at astrocytes, their nuclei are negative for HuNu.

in randomly selected subjects from both groups (Figure 4.10A “cells in the healthy brain” group, Figure 4.10B “cells in the ischemic brain” group). Astrocytes nuclei were checked for HuNu signal, but only DAPI stained nuclei were found. There was no evidence of double positive GFAP/HuNu cells. In the low magnified overlays of Figures 4.9B and 4.9C it is possible to see the implantation channel colonized by astrocytes whereas the implanted cells can only be seen deeper in the cortex.

4.3.5 Lightsheet Fluorescence Microscopy (LSFM)

The graft was analyzed for its exact location and eventual migrating cells in a 3D brain model. The technique allows the identification of the graft due to the cells’ expression of the fluorescence marker eGPF captured by the LSFM microscope. Two subjects were randomly selected from the group “cells in the ischemic brain” to clear their brain with the technique described in the Materials and Methods chapter. After acquisition of brain images in the microscope, this LSFM data was coregistered with the Allen Brain Atlas (Lein et al., 2007). Upon coregistration it was possible to identify the exact cortical subregion where the implanted cells had been engrafted (see Figure

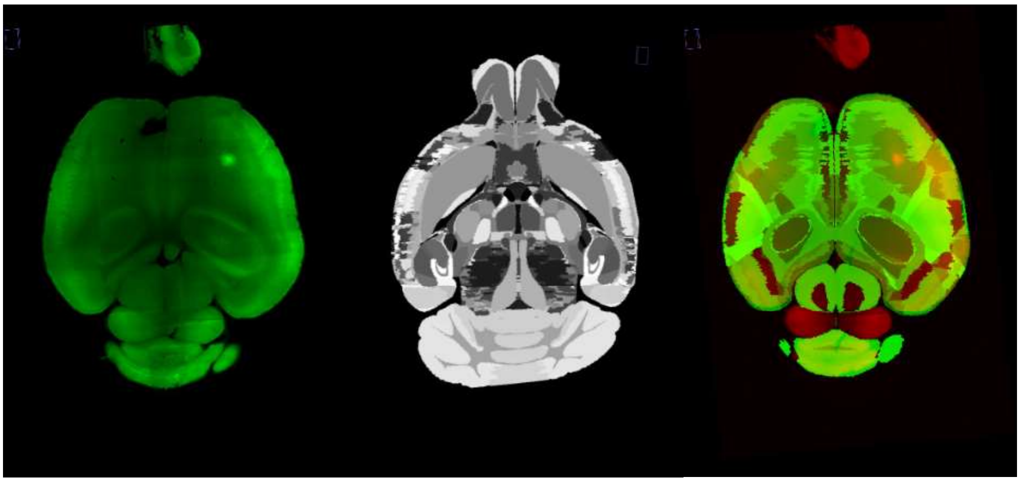

Figure 4.11: Spatial distribution of engrafted H9 cells assessed via LSFM. Left: LFSM dataset. Middle: Allen Brain Atlas, color coded in gray scale for different labels (indexed). Right: Composite. Here it is possible to localize the graft on the specific brain region.

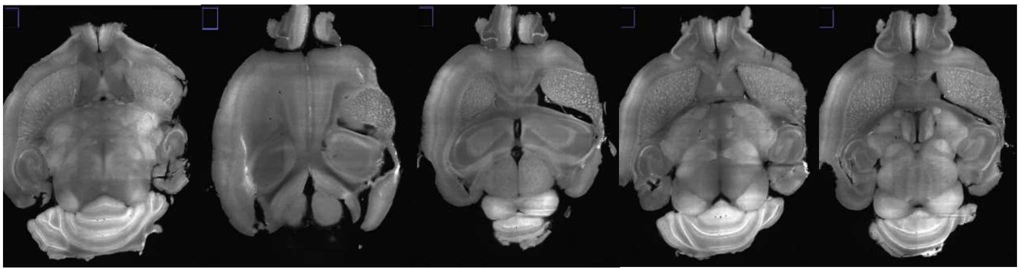

Figure 4.12: Axial sections of the brain 12 weeks after stroke. Representative sections taken from dorsal to ventral orientation (left to right). The distortion of the hippocampus can be clearly distinguished in the right hemisphere.

4.11 for original image with the graft, brain atlas and coregistered image). Grafts were identified in both analyzed animals and the eGFP positive cells were detected within the primary motor area exclusively, in layers 1 to 6a. Apart from the localization of the cells, it was possible to show in one of the animals the distorted hippocampus in the anatomical sections. Figure 4.12 shows five representative images taken every 100 sections of the LSFM dataset in the dorso-ventral plane. Note the lack of cortical tissue bordering the hippocampus. A 3D model of the brain was created to further explore the localization of the graft and eventual migratory cells (Figure 4.13).

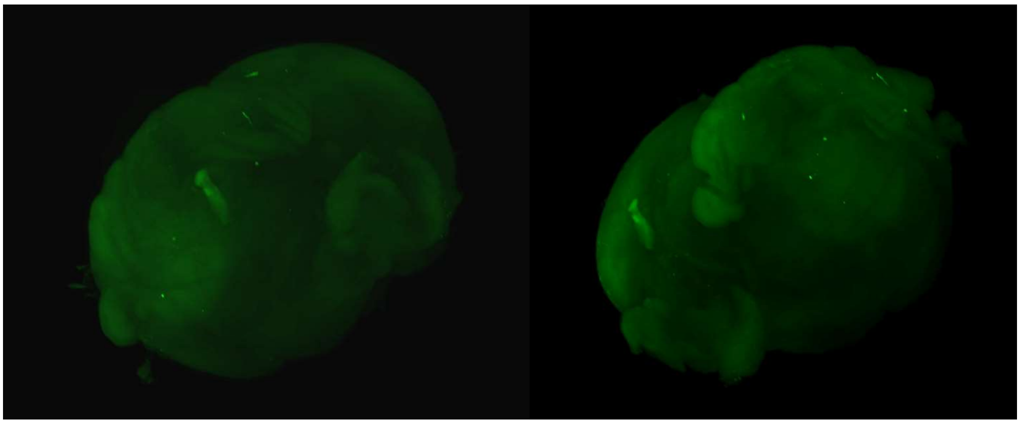

Figure 4.13: 3D view of the brain with GFP positive cell graft. Two different 3D views of the cleared brain containing the graft. The green signal of the graft corresponds to the GFP fluorescence. Top image: view of the brain from the anterior-dorsal right corner. Bottom image: View of the brain from the anterior-ventral left corner. Since the brain is transparent, the graft can be recognized in the right cortex from every angle.

4.3.6 Resting state fMRI

Results of the resting state functional MRI evaluation are expressed as correlation factors among different regions of interest pre-selected before the data analysis. As already detailed in the previous chapter, the resulting correlation factors of functional connectivity between all regions were numerically expressed and visualized in colors in a matrix.

Once again, my approach was first to evaluate the group that suffered no ischemia and served as control to the stroke in the cell implanted brain. Animals were scanned before the cell implantation and one, five and eleven weeks after it to have comparable points to the ischemic brain (see timeline of experiments at the beginning of this chapter for a better overview of experimental design).

The resulting matrices for all 8 subjects of this group are shown in Figure 4.14 (above). If we assume that the global connectivity strength is reflected in the color overview of the matrix, then an increase in the connectivity can be observed in the second week time point, followed by a gradual reversal that touches the baseline values at week 12. The biggest change observed is the jump between pre surgery and the "2 weeks" which is only one week after cell implantation.

Again, analyzing the change in all factors of the matrix, I filtered out all variations with a difference of less than 0,2 to the baseline value, and plotted the remaining significant changes on an anatomical template with regions of interest for a better visualization (Figure 4.14, before). The location of the graft is diagrammed as a yellow cone. As anticipated in the paragraph above, the largest changes in connectivity are observed between the pre-surgery and 2 weeks time point. An increase in correlation between transhemispheric regions M and SS1 is clearly recognizable, added to increased correlation between intrahemispheric M and SS1 for both hemispheres, the one containing the implanted graft and the contralateral.

On the 6th week time point, there is still an increase in connectivity between left M and SS1 regions to be observed, however the other incre-

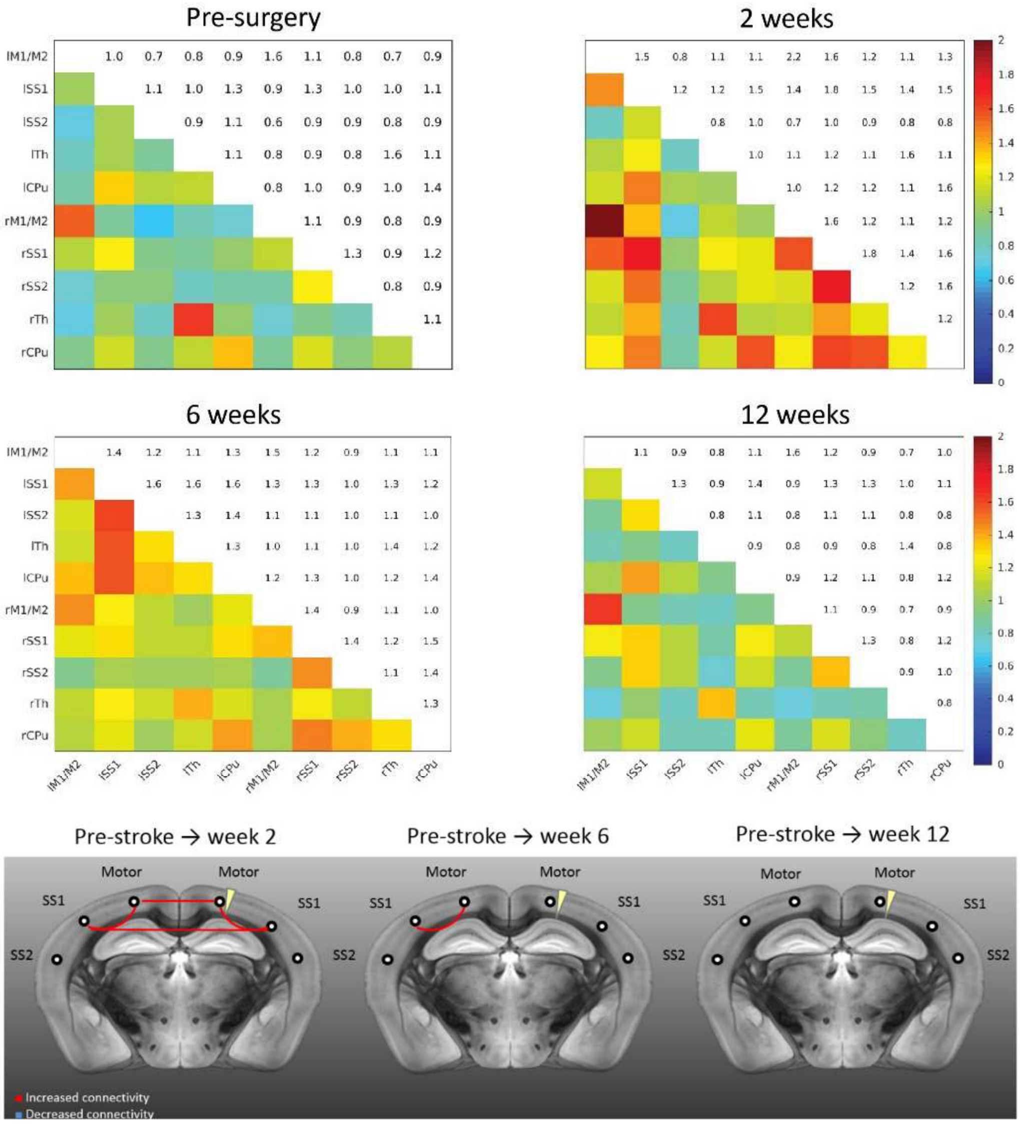

Figure 4.14: Results from the bilateral functional data analysis for the 'cells' group. A) The correlation strengths are visualized color-coded with dark red being the highest correlation and dark blue the lowest. Each matrix mirrors the correlation values in colors and numbers. The two matrices on top represent the first two time point measurements, the two below the later measurements. At first sight, the global connectivity increases after cell implantation and decreases gradually to reach the pre-surgery status at the end of the observation period. B) Significant connectivity changes are represented over a coronal template. Increases in connectivity become evident when looking at the values of z-score. N=9, animals with negative z-scores have been excluded from the analysis.

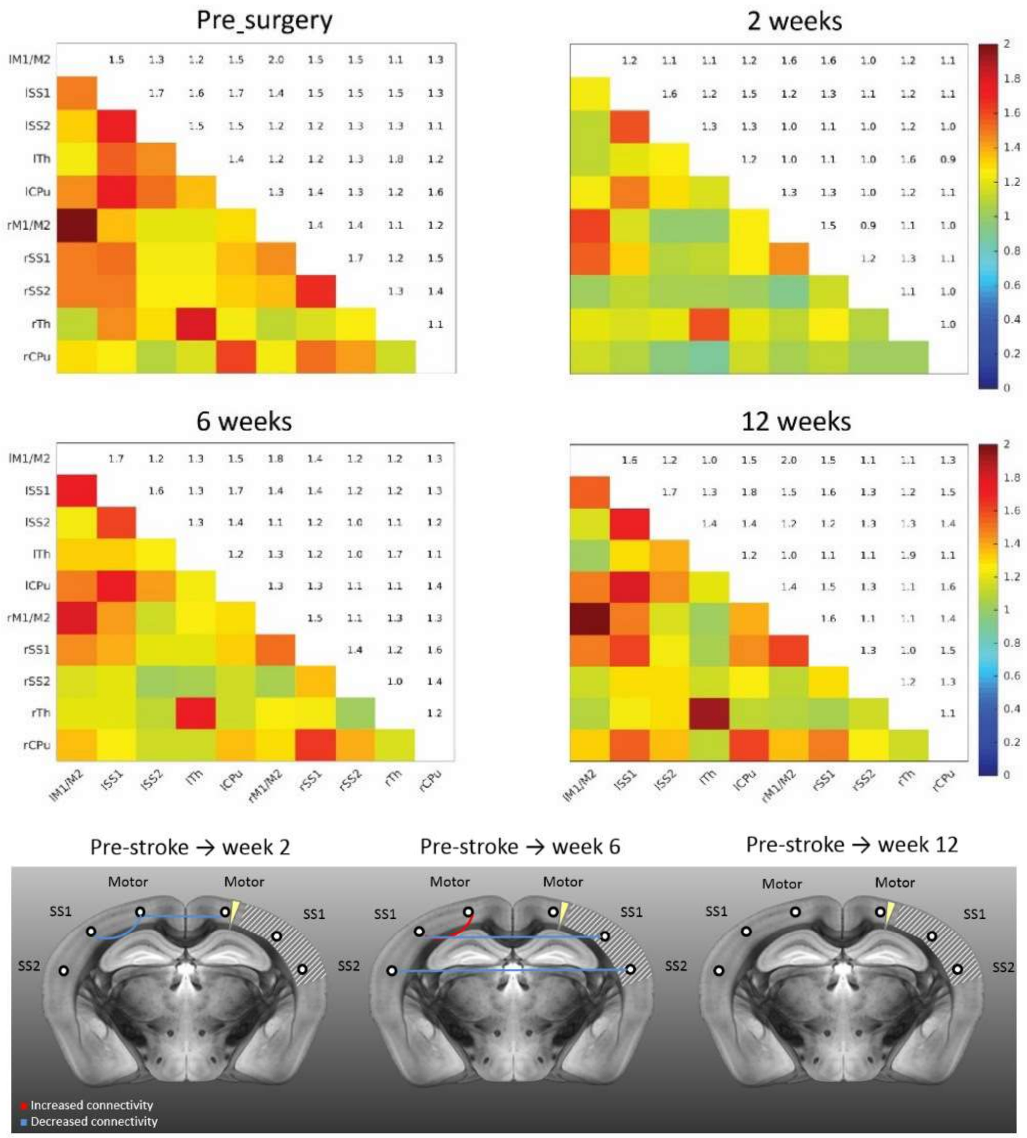

Figure 4.15: Results from the bilateral functional data analysis for the 'stroke + cells' group. A) The correlation strengths are visualized color-coded with dark red being the highest correlation and dark blue the lowest. Each matrix mirrors the correlation values in colors and numbers. The two matrices on top represent the first two time point measurements, the two below the later measurements. At first sight, the global connectivity drops after both surgeries and increases gradually to reach the pre-surgery status at the end of the observation period. B) Significant connectivity changes are represented over a coronal template. Decreases in connectivity become evident when looking at the values of z-score. N=14, animals with negative z-scores have been excluded from the analysis.

ments visible at the second week are no longer distinguished. On week number 12, there are no changes above a difference of 0,2 to report compared to baseline values.

The next set of data analyzed was the functional connectivity over time corresponding to the "cells in the ischemic brain" cohort. The bird's eye evaluation of the timewise progression shows a decrease in global connectivity between the baseline and the 2nd week measurements, followed by a steady and progressive increase returning to baseline values by the 12th week of experiments (Figure 4.15, left).

In order to asses if such changes are significant, I applied the 0,2 of z-score difference threshold again to each of the correlation factor differences observed between baseline values and the time point in question, to discard minor changes. The changes between time points are always calculated against the baseline, not to the previous time point. Figure 4.15 (above) illustrates the resulting changes on the anatomical template. For better visualization purposes, the area of the initial edema on the cortex and the localization of the cell graft have been highlighted with a striped pattern and a yellow cone respectively.

On the second week after stroke and one week after cell implantation, the major alterations in connectivity correlation are a decrease between the left and right motor cortices and a decrease between the contralateral motor and primary somatosensory cortex.

On the following time point, 6 weeks after stroke, there is a pronounced connectivity decrease between left and right primary somatosensory cortices and left and right secondary somatosensory cortices. Moreover, an increase between the contralesional motor and primary somatosensory cortex can be observed. There are no changes equal or above of 0,2 to report in the comparison between the 12th week time point and baseline.

4.3.7 Electrophysiology

In order to test for the excitability of the implanted cells and its capability to generate action potentials, 2 mice containing GFP positive stem cell grafts were analyzed via patch clamp electrophysiology. Figure 4.16 shows different plot corresponding to several cells from both subjects. The grafts could easily be located in the sectioned brains due to an IHC staining for eGFP (Figure 4.16A). It the Figure we see an extensive graft localized on the cortical surface of the brain. Figure 4.16B shows the border of the graft on its ventral end, where several neurites can be recognized protruding deep into the cortex (white arrows). The patch-clamped cell were selected by its morphological characteristics: those extending their neurites into the cortex were preferred for analysis above the less developed ones. The Biocytin labeling depicted in figure 4.16C shows the entire morphology of a single cell, the neurites can easily be distinguished as they protrude perpendicularly to the cortical surface and in radial directions towards the rest of the graft.

The aforementioned cell was evaluated for spontaneous activity (Figure 4.16D) which was positive and pulsatile, heterogenic in its frequency. Action potentials were abolished by adding a specific sodium channel blocker, Tetrodotoxin (TTX) 1uM, which indicates the presence of voltage gated sodium channels (Figure 4.16F). The high voltage amplitude in the action potential (Figure 4.16E) suggests that the analyzed cell is in an advanced developmental stage and has acquired neuronal like characteristics. The hyperpolarization of the cell to -140 mV reveals the presence of hyperpolarization-activated cyclic nucleotide regulated cation channels (Figure 4.16G).

All electrophysiology experiments were performed by Dr. Simon Hess from the working group of Prof. Dr. Kloppenburg, Biocenter, Cologne, Germany. The images were also taken, edited and put together by him, together with the figure legends.

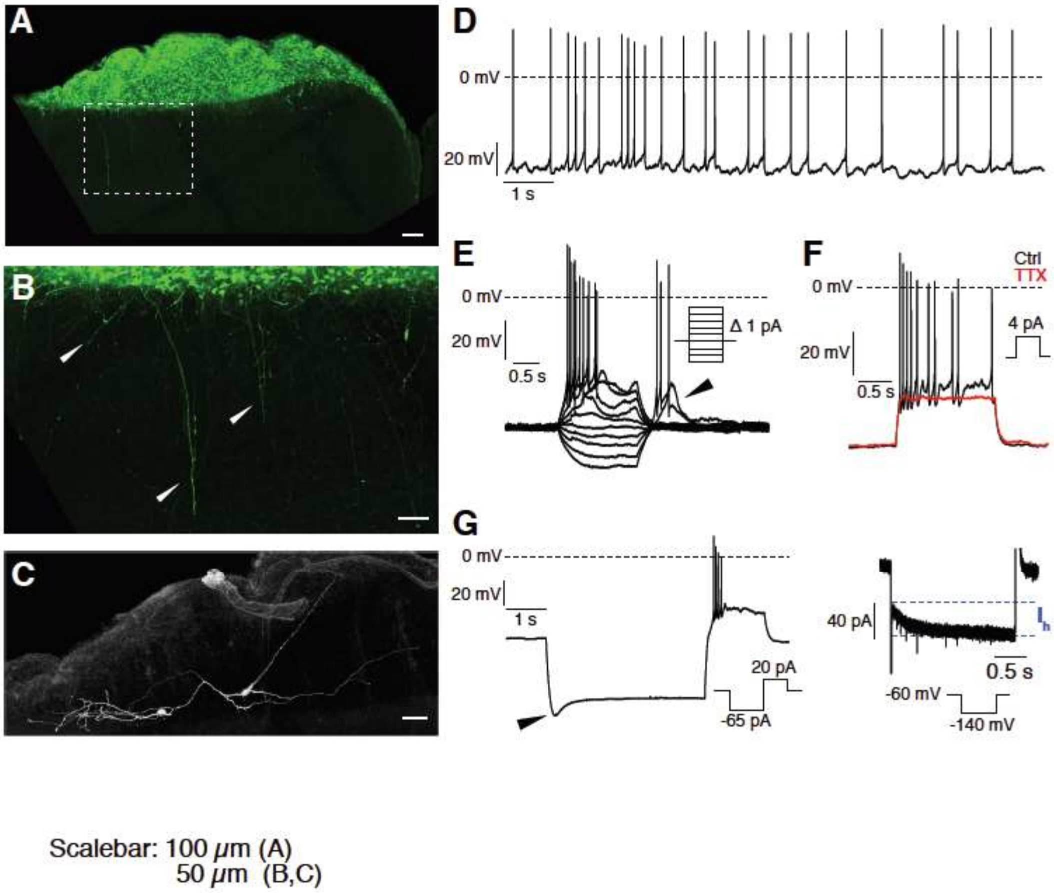

Figure 4.16: Electrophysiological characteristics of H9 neural stem cells at 12 weeks post engraftment. A) GFP staining of the implanted graft. Scalebar: 100 µm. B) Magnification of the dotted square in A showing projections from the graft into the cortex. Scalebar: 50 µm. C) Biocytin-labeling of a recorded cell. Scalebar: 50 µm. D) Spontaneous activity of a recorded cell. E) Current injections during recording elicited action potentials. Arrowhead: Post inhibitory rebound with APs. F) Abolishemebnt of Aps by TTX (1 µM) indicated the presence of voltage-gated sodium channels. Black trace: control; red trace: TTX. G) Right, hyperpolarization of the cell to -140 mV reveals a sag-potential (arrowhead) which is mediated by hyperpolarization-activated, cyclic nucleotide-regulated cation (lh) channels. Left, lh current elicited by a voltage step to -140 mV.

4.4 SUMMARY

1. BLI signal intensity among subjects is heterogeneous, however it stays within the same order of magnitude over time for each subject.
2. There is no net increase or decrease in the BLI signal intensity average for the "Cells in a healthy environment" group.
3. There is no net increase or decrease in the BLI signal intensity average for the "Cells in an ischemic environment" group.
4. There is no correlation between signal intensity and graft size or graft location (graft on the cortex surface vs. graft through the cortex).
5. The performance of the ischemic cohort in the Rotating Beam decreases after ischemia and shown no improvement related to cell implantation.
6. NeuN positive cells are found outside of the graft. They are cells belonging to the mouse tissue and not migrating cells from the graft.
7. Astrocytes are densely found in the borders of the graft and less densely in the graft core.
8. Neurites of the implanted cells project beyond the graft borders.
9. GFAP positive cells found in the graft borders or core belong to an astrocytic reaction (scar tissue) of the host and do not stem from the implanted cells.
10. Analysis of coregistration between LSFM images and Allen Brain Atlas show that the location of the graft is limited to the primary motor area, layers 1 to 6a.
11. 3D visualization of the graft inside of the cleared mouse brain (prepared for LSFM) shows no evident migration of implanted cells at 12 weeks after stroke – 11 weeks after cell implantation.
12. For the "Cells in a healthy environment" group, there is an increase in connectivity correlation factors compared to baseline, as follows:
    a. Week 2: intrahemispherically between SS1s and Ms, in both hemispheres; transhemispherically for SS1s and Ms.
    b. Week 6: contralaterally to the cell implantation for SS1 to M.
13. For the "Cells in an ischemic environment" group, there are changes

in connectivity correlation factors compared to baseline, as follows:
    a. Week 2: Decrease between transhemispheric Ms; decrease between contralesional SS1 to M.
    b. Week 6: Increase in contralesional SS1 to M; decrease in transhemispheric SS1 to SS2.

14. The electrophysiological recording suggest that the clamped cells are in an advanced developed stage and have acquired depolarizing abilities, characteristic of neuronal cells.
15. The action potentials are enabled through voltage gated sodium channels.

4.5 DISCUSSION

In this chapter I investigated the effect of implanted neural stem cells after cortical stroke, focusing on the viability, location and differentiation of engrafted cells, the functional connectivity in selected seed regions and the behavioral performance of the cohort of mice after cell implantation. In order to obtain significant conclusions, the results had to be analyzed taking into account if each of the procedures applied to the mice contributed to the observed changes. This was achieved by including control groups for every surgery before starting with the final experimental cohort of implanted cells in the ischemic cortex. Hence, the model of stroke was fully characterized (see Chapter 3) before starting experiments of cell implantation. It was also necessary to include relevant control groups to ensure that any reported changes after cell implantation in the ischemic brain would be a consequence of the cell presence and not secondary effects of the ischemia or the implantation surgical procedure itself.

The capacity of neural stem cells to differentiate into mature neurons has given rise to the therapeutic idea of replacement of neuronal degenerative or dead tissue. In the first few days after stroke, the target of cell therapy is most likely an inflammatory process that enhances the extent of brain injury and impedes the recovery process (Savitz, 2015). Scoping beyond the sub-acute period after stroke, in patients with residual deficits months or years after ischemic arrest, there is typically minimal if any further recovery and no effective therapies. In this late time frame, inflammation is likely less important and the major targets of cell therapy are neurogenesis, angiogenesis, synaptogenesis and enhanced plasticity in cells bordering the area of infarction. Trials in this time frame target direct injection into the brain (as opposed to intra-arterial administration) using stereotactic techniques delivering cells to the surround of the infarcted region to enhance repair and recovery most likely through secretion of growth factors or small molecules that may stimulate the local environment (Kenmuir and Wechsler, 2017). To date, there is little information about the differentiation process of the implanted cells *in vivo* because most of the studies are based on histological post mortem results at previously defined time points after implantation. There are many different factors impacting the maturation of the implanted cells: it must be taken into account that different cell lines develop differently depending on the strain of host mouse, the amount of surviving cells – which depends on the initial graft size (Vogel et al., 2018) -, the immune reaction of the host, etc. Studies conducted previously in our group have been able to shed light on the maturation process of implanted neural stem cells that have been genetically modified to express detectable molecules after a desired maturation milestone. Such careful construct design has enabled the elucidation of differentiation timeline of implanted stem cells in the mouse brain by being able to selectively detect implanted cells after their differentiation into early neurons by means of DCX expression or after a later maturation stage when they start expressing synapsin (Tennstaedt et al., 2015). Based on these results, we chose to implant and observe the development of the graft *in vivo* during a minimal amount of time in which we had concluded that the surviving stem cells would be already in a mature state, a period of 11 weeks after the implantation of the H9 graft. The results of the electrophysiological analysis conducted by Dr. Simon Hess, in collaboration for this project, confirmed the mature-neuron electric phenotype displayed by the implanted cells at the end of our observation period, confirming that choosing a longitudinal experiment of 12 weeks was enough to obtain neurons mature enough to be able to elicit a synaptic response upon stimulus.

My purpose was to focus on the differentiation of the cell precursors into the neuronal lineage, however, I also checked for the presence of astrocytic cells. I found them surrounding the graft and the implantation canal, as well as some inside of the graft core, nevertheless none of the detected astrocytes tested positive for HuNu, meaning that they did not originate from the implanted cells themselves but found their way into the graft parenchyma from the host tissue. The fact that I found several positive NeuN cells surrounding the graft, without any of them evidencing their origins from the implanted precursors –checked again with HuNu staining – at 11 weeks after implantation, means that I may have missed to detect the period in which the grafted cells start expressing the afore mentioned protein. However, it is more likely that the antibody had better affinity for the mouse form of NeuN compared to the human one, making it more visible under the fluorescent microscope and thus leading the presumably negative signal from the graft to misinterpretation (Guselnikova and Korzhevskiy, 2015). Previous studies have reported that different neurons from the same subject display different levels of NeuN expression: the protein was poorly expressed in the substantia nigra neurons of the rat, while being completely absent in others (Cannon and Greenamyre, 2009). In humans, neurons have also been proven to have heterogeneous levels of expression (Sukhorukova, 2014). In general, no clear correlation between the intensity of NeuN immunoreactivity and a certain type of neurons has been established. The differences in the intensity in the reaction for NeuN reflect the differences of the expression of this protein in a cell, which are associated with both the constitutive characteristics of the neurons and its functional state, as well as the presence of injuries in the nervous system, which can also affect the expression of the NeuN protein. For example, axonal injury leads to an almost complete loss of NeuN immunoreactivity in motoneurons of the facial nerve nucleus (McPhail et al., 2004).

Previous studies in our lab have shown a linear correlation between photo emission and the number of Luciferase expressing cells *in vivo*, that is comparable to the linear correlations observed for *in vitro* dilution series (Aswendt et al., 2013, Vogel et al., 2018). Vitality of implanted cells – monitored by BLI - has been reported to decline, stay constant or increase. The method is also suitable to detect changes in gene expressions during differentiation of the engrafted cells (Tennstaedt et al., 2015). The technique, however, fails to distinguish if an observed change in the signal intensity is due to a change of viable cells expressing the protein or due to a change in the amount of protein being expressed by each of the cells, unless a careful quantification of living cells is performed right after BLI measurement. Such approach would be extremely complex to perform taking into account the amount of cells that would need to be counted, but if done accurately the results would shed light in knowing where the changes in intensity are stemming from. The results of my experiments show a stable expression of the protein during the 11 weeks of monitoring. For the sake of interpretation I will assume that each cell keeps its expression on a constant level, hence the amount of viable cells also remains constant. Results also report a heterogeneous level of acquired signal among subjects, this doesn't necessarily imply that the emitted signal is different. Factors like depth of engraftment and shape of the graft play an important role in the amount of signal detected and viability of the implanted cells, respectively. As opposed to previous studies from our lab where neural stem cells were implanted adjacent to a stroke delivered by filament MCAO, the implantation site was carefully chosen to be localized outside of the edematous tissue, which was reproducible in the location of the somatosensory cortex. Green and colleagues reported a significant loss of down to 20-30% BLI signal 4 weeks after engraftment (Green et al., 2018), which might be associated with the time of cell implantation after stroke and the severity of the ischemic lesion. In their study, H9 cells were implanted adjacent to an ischemic lesion which was greater in size – striatum and cortex beyond somatosensory areas – and only 2 days after stroke onset, when they claim that the lesion size is not finally defined and it could have been extended further particularly after the cell implantation surgery. In my project, I implanted the cells one week after the brain infarct, when the size of the edema was already decreasing, and adjacent to a stroke lesion that did not endanger the life of the subjects, meaning that the consequences were symptomatic but not life threatening. The integration of the cells into the host tissue depends on the host tissue conditions, hence a successful survival of cells is related to their implantation condition into healthy brain tissue (Buhnemann et al., 2006).

All grafts analyzed histologically were surrounded and infiltrated by GFAP-positive HuNu-negative astrocytes, implying a recruitment of host glial cells to form a glial scar, thus protecting the host tissue from the xenograft and vice versa. This local immune response did not affect the viability of the graft throughout the 11 weeks of observation. The performed intracerebral engraftment is a procedure that disrupts the blood brain-barrier and cortical parenchyma architecture. This triggers a mild inflammatory reaction that attracts reactive astrocytes to the damaged site which then secrete several cytokines including interleukin (IL)-1β, IL-2, IL-4, IL-6, IFN-γ and TNF-α (Mirza et al., 2004). The lineage commitment of neural stem/progenitor cells is affected by the mentioned cytokines, which was extensively studied *in vitro* (Mao-Draayer et al., 2011).

The results from the LSFM imaging show no migration of cells beyond the borders of the graft, at least not detectable single cells away from the implantation site. This finding is closely connected to the amount of glial scar surrounding the graft since it impedes the spreading of grafted cells by forming a cage-like structure that is hard to overcome for single cells and even for outgrowing neurites (McKeon et al., 1991), which is in accordance with the results shown in Chapter 4 (Figure 4.9). Very few neurites are detected outside the graft borders with the eGFP antibody detection, confirmed by eGFP signal detected before electrophysiological recordings (Figure 4.16B). The LSFM method of brain clearing and imaging was applied to only one of the subjects from the "cells in an ischemic environment" group, hence our limitation to generalize this finding to the entire cohort and to the control group. Using this different imaging approach, we could follow the migration – or lack thereof – of the implanted cells and also confirm an observation made in the previous chapter when we characterized the lesion: the hippocampus extends towards the surface of the brain for the greater part of the cortical sections acquired.

As stated above, no results should be interpreted without thorough knowledge of the situation in the control group. In this part of the project, our control group "cells in the naïve brain" showed changes in brain connectivity one week after implantation (two weeks after the hypothetical stroke, thus called “2 weeks time point”). The changes that were observed above the threshold correspond to contralateral increase in connectivity correlation between motor cortices and primary somatosensory cortices, as well as intrahemispheric increases between the M and SS1 cortices. Of all changes, only one increased connectivity remains above threshold in the 6th week, the rest drop back to values closer to baseline and there are no changes to report after that time point. As already explained in the discussion of Chapter 3, an increase in connectivity strength can imply different meanings: in our case a stabilization of a destabilized system is discarded because there is no destabilized system to begin with, cells have been implanted in healthy brains of NMRI-Foxn1nu/nu mice. The hyperconnectivity could be a consequence of the reaction of the brain to the implantation procedure: although there is no rejection of the graft from the host, the recruitment of reactive cells has been evidenced. We must consider the cytokines expressed by such recruited cells and the effect that such cytokines may have on the surrounding tissue, that has been analyzed within the seed region of interest. The difference in the dynamics between the increased connectivity after stroke observed in Chapter 3 – starting at the 2nd week and being more evident at the end of the observation period of 12 weeks - and the increase after cell implantation, where the changes are transient and revert to baseline after week 6 suggest that: not only the ischemic damage but also the inflammatory signal caused by the disruption of parenchymal architecture during the engraftment surgery have a saying in the communication correlation between regions. After characterizing the changes in connectivity strength due to dMCAO and cell engraftment separately, I proceeded to measure the correlation factors after cell implantation in the ischemic brain, which entails a complex scenario after two surgical procedures without knowing how the second modulates the changes produced by the first. It was evident from the results that the combination of surgeries does not result in an arithmetic combination of connectivity changes.

There is a lack of previous studies reporting analysis of resting state connectivity after cell implantation, let alone cell engraftment after stroke. Van Meer and colleagues investigated the functional and structural recovery of the sensorimotor cortex after stroke in rats (van Meer et al., 2010; van Meer et al., 2012). They reported a decrease in connectivity strength that slowly recovered over time, however, these results are not able to be directly compared to ours because they used the filament stroke model which produces vast ischemic damage and inflammatory response. Green and colleagues were the first to report resting state connectivity analysis in an ischemic brain with neural stem cells engraftment (Green et al., 2018). Again, the chosen stroke model in such studies produced more heterogeneous and vast ischemic lesion sizes, a worse mortality rate and an impossibility to analyze the ipsilateral cortex beyond the 2nd week after stroke due to the deformation of the hemisphere and the changes in structure symmetry – that impairs proper localization of the defined seed regions of interest. In the experiments performed in my project the corpus callosum is not affected by the implantation procedure and suffers no injury from the needle, therefore the transhemispheric bilateral correlations in the BOLD signal are not disrupted. To my knowledge this is the second study that utilizes resting state BOLD imaging for a cellular therapeutic approach in post-stroke mice, and the first to analyze correlations in both ipsi- and contralesional hemispheres throughout the entire 12 weeks longitudinal study due to the mild nature of the dMCAO-induced stroke. The decrease in connectivity correlation observed after 2 and 6 weeks in the "Cells in the ischemic brain" group are in accordance with many studies that report such finding after filament MCAO or traumatic brain injury (Harris et al., 2016). However, having inspected all the previous control groups separately, we now know that the observed correlation decrease is due to an accumulation of events and that the combined result cannot be predicted easily. It seems that the second surgery is modulating the changes elicited by the first one and that the combination of surgeries may have affected the transhemispheric communication of homologous cortical regions. There is good evidence for the existence of an imbalance in neuronal excitation-inhibition as indicated by reductions in GABA or increases in glutamate signaling (Cantu et al., 2015; Drexel et al., 2015), then changes in synaptic strength and efficacy might well underpin alterations in the observed functional connectivity, although the biophysical mechanisms behind this observation remain to be determined.

The large number of voxels within the defined ROI entails a great SNR and a smaller signal variance within, as a consequence a large number of voxels will be significantly correlated. This is one of the limitations of analyzing seed based ROIs instead of independent components, and will be further debated in the General Discussion together with the integration of all the observations from Chapters 3 and 4.

5

CHAPTER 5

REMOTE CONTROL OF CELL ACTIVATION

5.1 DREADD TECHNOLOGY

After obtaining promising results with neural stem cells in stroke damaged brains, new tools are necessary to dig into the mechanism underlying functional recovery. To investigate the role of cellular replacement in post-stroke recovery, it is desirable to be able to control the electrical activity of grafted cells. The neuronal stimulation or silencing arising from transplanted NSPCs would be helpful to shed light onto their mode of action. Switching off the neuronal activity of grafted cells would result in a minor or even no relief of symptoms compared to a control where transplanted cells are contributing to regeneration mainly via functional integration.

A molecular tool to remotely control the electrical activity of neurons has been developed recently. Roth and colleagues have succeeded to modify two human muscarinic acetylcholine receptors M_3 and M_4, to derive a new class of designed receptors (Armbruster el at., 2007). While the func-

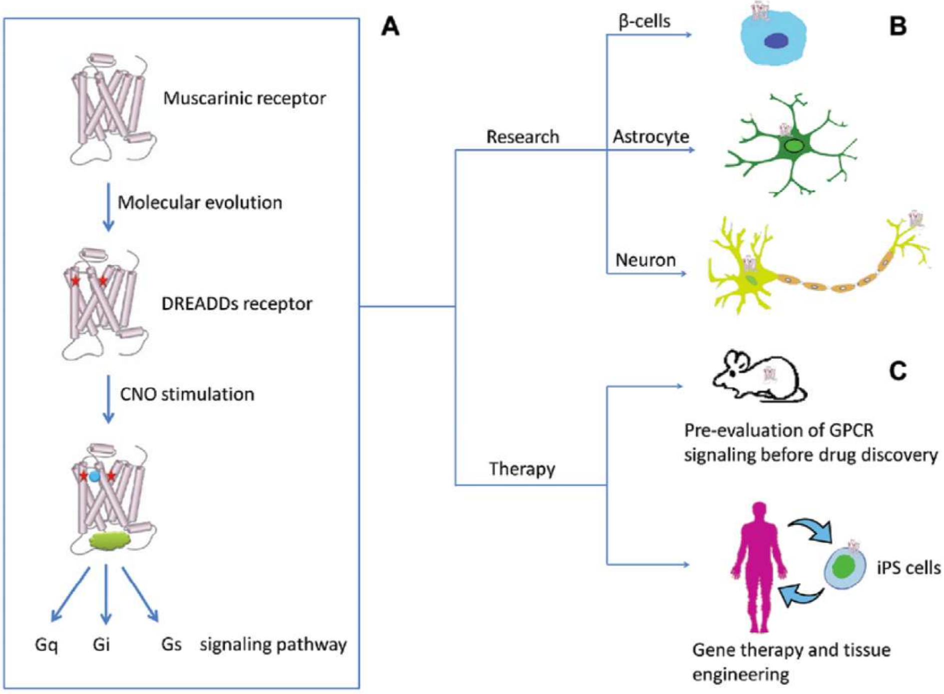

Figure 5.1: DREADDs as a chemogenetic tool to modulate GPCR signaling *in vivo.* (A) Introducing two mutations in transmembrane III and V of muscarinic receptors which create DREADDs receptors that can precisely control the Gq-, Gi-, or Gs-signaling pathways. (B) DREADDs technology has been successfully applied in β-cells, astrocytes, and a variety of neurons to control GPCR signaling *in vivo*. (C) DREADDs technology has a great potential to be used in drug discovery, gene therapy, and tissue engineering. Extracted from Zhu and Roth, 2014.

tion of the modified receptors hM_3D and hM_4D were conserved during the evolution process, the ligand specificity was changed from the natural agonist acetylcholine to the drug clozapine-N-oxide (CNO). Because CNO has no known biological function in the body (Weiner et al., 2004), hM_3D and hM_4D were the first two members in a new class of designed receptors called "Designer Receptors Exclusively Activated by a Designer Drug", abbreviated as DREADDs.

The molecular identity of hM_3D and hM_4D being G protein-coupled receptors (GPCRs), implies their use to alter the electrical activity of neurons. hM3D is a GPCR that couples to G_q proteins while hM_4D interacts with G_i proteins (Armbruster et al., 2007). G proteins in general, once activated by a GPCR, dissociate into their subunits G_α and $G_{\beta\gamma}$ that are involved in different intracellular downstream pathways depending on their class (Wu et al., 2012).

G_q proteins activated by hM_3D evoke the cleavage of phosphatidylinositol-4,5-biphosphate (PIP_2) through action of $G_{\alpha q}$ on phospholipases, which leads to the production of inositol-1,4,5-triphosphate (IP_3). This compound binds to its specific intracellular receptor to open calcium storages like the endoplasmatic reticulum. Thus, activation of hM_3D causes an increase of intracellular calcium levels and eventually a reduction of the membrane potential (depolarization). A partial depolarization of a neuron in turn makes it more prone to fire action potentials so that the stimulation of hM_3D in neurons increases their electrical activity. In contrast, the βγ subunit of activated G_i proteins directly interacts with G-protein inward-rectifying potassium (GIRK) channels. Opening GIRKs in response leads to an efflux of potassium ions from the cell and thereby to an increase of the membrane potential (hyperpolarization).

Although its strength definitely lies in basic neurological research like the investigation of neuron functions (Rogan and Roth, 2011), the DREADD system also holds promises regarding clinical application. In combination with stem cell transplantation it might enable whole new therapeutic approaches if functional integration of implanted NSPCs is confirmed to be crucial for regeneration of damaged brain parenchyma. Since CNO is biologically inert and can pass through the blood brain-barrier (Bender et al., 1994), remote control of the graft's electrical activity by the oral or parenteral administration of CNO would be possible without side effects. For instance, hM_3D could be introduced into striatal grafts for Parkinson's disease that act as an inducible drug pump (Dell'Anno and Caiazzo, 2014). Clinical applications of DREADDs, however, are still distant from today's perspective.

To assess the impact of functional integration of transplanted NSPCs on the relief of stroke-associated symptoms, DREADD technology has to be combined with stem cell transplantation in a model with most clinical relevance. The final set-up of experiments comprises the stereotactical implantation of neuronal precursors carrying hM_4D into the cortex of stroke damaged mice brains. Stroke is induced by the distal middle cerebral artery occlusion model, which produces cortical lesions (see Section 2.3). Specific behavioral tests in the presence and absence of CNO might show the contribution of neuronal activity from the implanted cells to the functional and cognitive improvement.

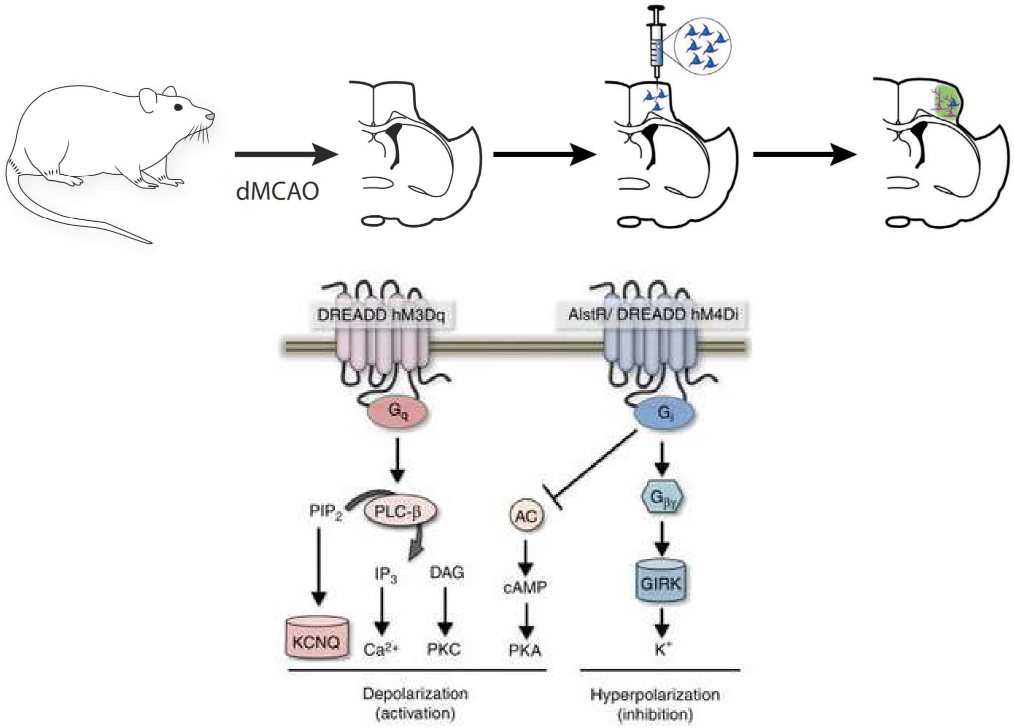

Figure 5.2: Schematic representation of experimental setup on the macroscopic and molecular level. Above: After inducing stroke in the rodent model, the neuronal stem cells carrying the respective receptor are implanted in the periphery of the lesion. The cells are investigated over time to check for functional integration and the animal is assessed for behavioral performance. Courtesy of Dr. Tornero. Below: Modulation of neuronal activity with the DREADD system, showing the molecular mechanisms of receptor activation and the agonist CNO. Extracted from Wulff and Arenkiel, 2011.

Nevertheless, the mentioned *in vivo* studies must be preceded by *in vitro* experiments. Our collaborators in Sweden, in particular Dr. Daniel Tornero from the Lund Stem Center in Lund, had been conducting experiments with long-term self-renewing neuroepithelial-like stem cells (in short, lt-NES cells). These lt-NES cells were isolated from induced pluripotent stem cells (iPSC) applying a protocol that was originally established for embryonic stem cells (ESC) (Koch et al., 2009) back in the lab of Dr. Oliver Brüstle in Bonn. This iPSC-derived cell line is almost identical to ESC-derived lt-NES cells and stably exhibits neural stem cell properties like indefinite self-renewal and potential to differentiate into neuronal and glial cell types with hindbrain specificity (Falk et al., 2012). In Tornero's lab, ESC-derived lt-NES cells had been implanted into the stroke-damaged striatum of mouse brains. After several months, grafted cells had survived, differentiated into different neuronal subtypes, functionally integrated by establishment of afferent and efferent connections and caused relief of stroke-impaired motor functions (Oki et al., 2012). Similar results were achieved by using lt-NEs cells that were fated towards a cortical phenotype before injection into the stroke-lesioned cortex of rat brains (Tornero et al., 2013). Hence, the implantation of lt-NES cells seems to be an effective therapeutic approach for stroke in different regions of the brain.

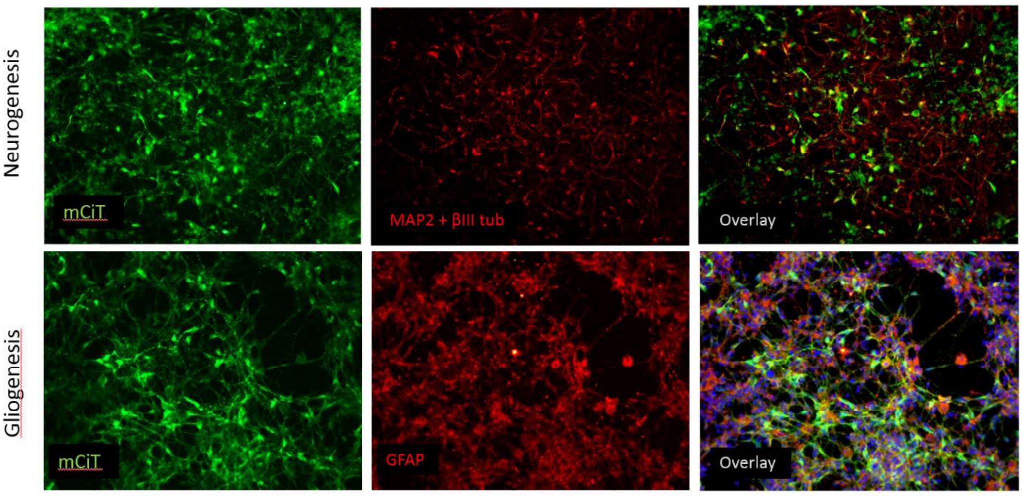

Figure 5.3: Differentiated lt-NES cells after lentiviral transduction with DREADD-hM$_4$D. Since the cell line gives rise to neurons and glia, specific markers for the cell type were used. The above panel shows the expression of DREADD receptors carrying the reporter gene for mCiT and the neuronal cell line reported with MAP2 and βIII tubulin. The panel below also shows the DREADD receptors in green, and GFAP reporting the astrocytes in red. On the right, the overlaid images. Images courtesy of Prof. Tornero.

A collaboration was agreed between our laboratories in which Dr. Tornero would develop the lt-NES cells from iPSCs so that the new line would be as similar as possible to the ones they had received in the past. The DREADD receptor attached to GFP would be double transduced with Luciferase attached to tdTOMATO and included in the genome. The double transduced cells would then be sent to us in Cologne to implant them in the cortex of healthy and ischemic mouse brains, and upon injection of CNO we would follow functional connectivity changes in the brain by means of rsfMRI.

Lentivirus including the DREADD plasmid were generated and they infected lt-NES cells with high efficacy (Figure 5.3). Unfortunately, Dr. Kokaia's group did not obtain positive results validating the constructs *in vitro* using electrophysiology. While hyperpolarization was expected to be seen in response to CNO administration, no effect was recorded in the membrane potential after differentiation of lt-NES cells *in vitro*. To overcome this challenge, two approaches were proposed:

- Transplant the DREADD lt-NES cells in a wild type animal and wait for 4 months until the cells have differentiated *in vivo*. Then, record electrophysiological measurements on acute slices and verify the result. This was proposed since the electrical properties of the cells in the living brain are much better than *in vitro*. Hence, the drugs could be applied *ex vivo* and check if the construct was expressed and if the protein was functioning properly.
- Double transduce the lt-NES cells with DREADD (without electrophysiological *in vitro* validation) and Luciferase and send them to our group to be implanted in the brain cortex, and check for expected results.

The project was canceled due to our impossibility to wait until the cells had differentiated *in vivo*, risking a negative result in electrophysiology measurements afterwards. Double transducing the cells with DREADD and Luciferase and sending them "blindly" to Cologne to start *in vivo* experiments was not considered as an option.

5.2 Optogenetics: The ChannelRhodopsin system

Optogenetics is the combination of genetic and optical methods to achieve gain or loss of function of well-defined events in specific cells of living tissue. On a broader sense, optogenetics includes a core technology –targetable control tools that respond to light and deliver effector function- and enabling technologies for delivering light into tissues under investigation, targeting the control tools to cells of interest, and obtaining compatible readouts and performing analysis. (Matsuno-Yagi and Mukohata, 1977).

Even though the optogenetic approach was coined in the field of the neurosciences, it addresses more unmet needs in the study of all biological systems: the need to control defined events in defined cell types at defined times in intact systems. Having control over these cellular events is important because they are meaningful only in the context of other events occurring in the rest of the tissue and the environment as a whole. (Deisseroth, 2010).

An opsin is defined as a light-gated protein that directly regulate the flow of ions across the plasma membrane and the first one was discovered 40 years ago in microorganisms. (Stoeckenius and Oesterhelt, 1971). Yet it was difficult to believe that these bacterial membrane proteins would not be toxic to mammalian neurons and that they could encompass a single component strategy, since they all needed chemical cofactors to absorb photons. Finally in 2005, it was reported that the introduction of a microbial opsin gene (without any other parts, chemicals or components) made neurons become

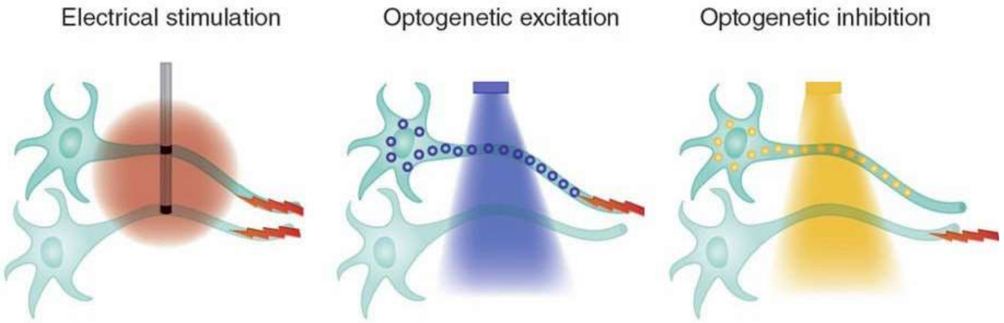

Figure 5.4: Principle of optogenetics in neuroscience. Targeted excitation (as with a blue light-activated channelrhodopsin) or inhibition (as with a yellow light-activated halorhodopsin), conferring cellular specificity and even projection specificity not feasible with electrodes while maintaining high temporal (action-potential scale) precision. Extracted from Deisseroth 2010.

responsive to light (Boyden et al., 2005). The development and improvement of the molecular system escalated over the following years and by the year 2010, channelrhodopsin, bacteriorhodopsin and halorhodopsin had proved capable of turning neurons on or off, rapidly and safely in response to diverse colors of light (Figure 5.4).

We thought of applying the optogenetic technology as an alternative to obtain cells that could be selectively activated, after the DREADD receptors could not be transduced in the lt-NES cell line in Lund.

Therefore, we started the isolation and cloning of the Channelrhodopsin gene into a construct under the expression of the constitutive promoter EF1α and mCherry as a reporter molecule. The chosen Channelrhodopsin was ChR2 (L132), a genetically modified channelrhodopsin that confers more sensitivity to blue light (Boyden et al., 2005; Nagel el al., 2003). This optogenetic actuator functions by regulating the membrane potential of excitable cells, therefore it needs to be expressed on the cell membrane at a very high level or density due to the low single channel conductance in order to generate sufficient membrane depolarization for light-induced action potentials. See Figure 5.5 for a simplified explanation of the cation channel mechanism of action and how the neuron expressing the channel on the surface received the activating blue light.

During the cloning and cell transfection experiments, the setup of the optogenetic system was prepared in parallel. Our project involved a dou-

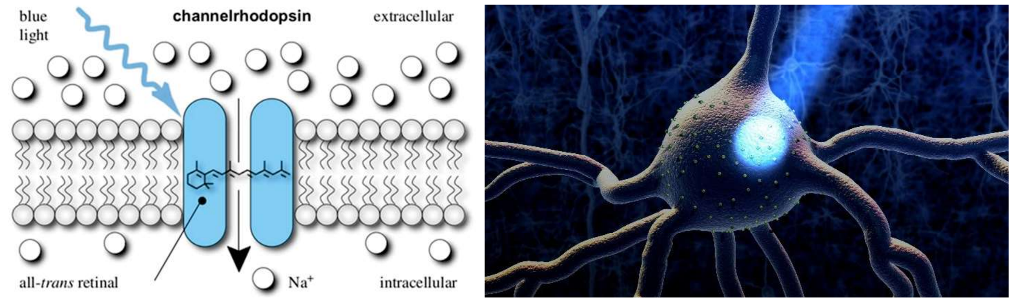

Figure 5.5: Schematic representation of the cation channel mechanism of action. Left: Blue light induces conformational changes in the transmembrane channel and the sodium ions are allowed into the intracellular space, thus inducing a change in membrane voltage and triggering depolarization. Extracted from Wong et al., 2012. Right: a 3D representation of the channels in the neuronal membrane and a ray of blue laser activating several channels located on the surface. Courtesy: National Science Foundation.

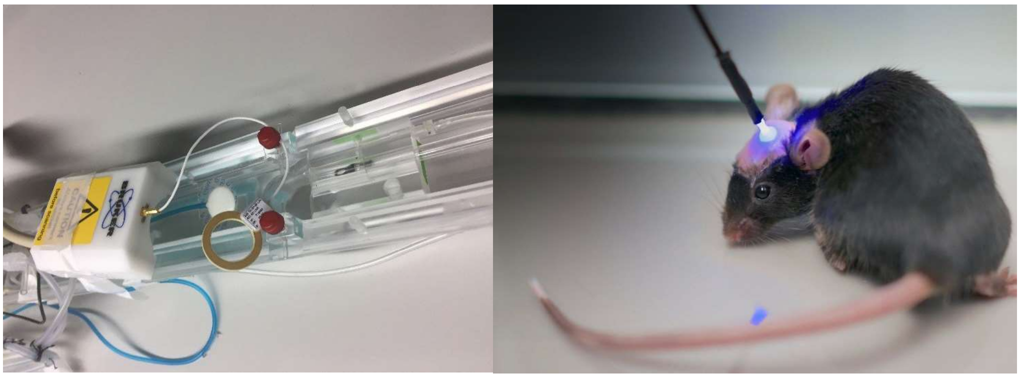

Figure 5.6: Animal holder and coil used for optogenetic measurements in the MRI scanner. On the left the animal holder and surface coil used to place the animal inside of the MRI scanner. Note the circular shape of the coil to allow the attachment of the optic fiber to the subject's skull. On the right, a mouse carrying an optic fiber attached to its scalp and the power source turned on.

ble transduction of H9 cells with a ChR2-containing plasmid and a Luciferase-containing plasmid to be implanted into Nude mice, but we set up the hardware using another strain. We chose for this purpose the commercially available BL6-based ChR2 transgenic mouse line with Thy1 promoter which had been shown to enable extremely high level brain expression of the opsin (Feng et al., 2000) and with a YFP gene as a reporter. Figure 5.6 shows the hardware used to prepare and enable the measurements.

The optic fiber was shallowly implanted into the right cortex of the Thy1 mouse in a location that would be on top of the implanted graft once the Nude mice were engrafted, in order to be able to excite the graft cells with the blue light. The implantation coordinates for the optic fiber were identical to the coordinates for the graft detailed in the Section 2.6, except for the dorsal-ventral location: if the cells would be implanted at DV 0.8 then the optic fiber should not be placed deeper than DV 0.2, taking into account that the cells would flood the implantation channel up to the surface of the brain and that the light intensity would be strong enough to reach cells through all cortex. The optic fiber purchased from Doric (Doric Lenses Inc, Quebec, Canada) was 400 um core diameter – 430 um outer diameter in width, 0,8 mm in length, flat tipped and with a numerical aperture of 0,48.

Once the scan protocol was established in the MRI session, the recorded BOLD image was detected in the right cortex. Several mice were used to set up the experimental details such as power of the light source needed to obtain a recordable response in the tissue. The laser wavelength was set

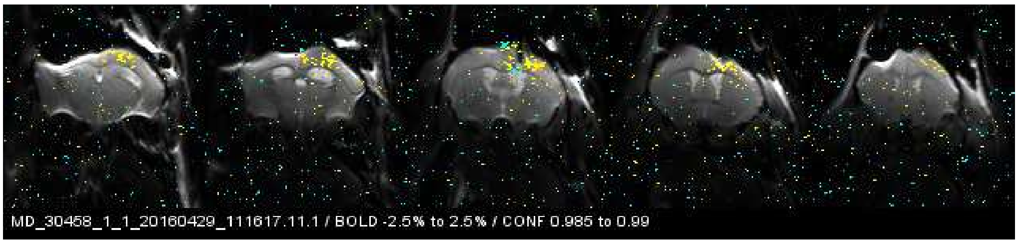

Figure 5.7: MRI images of BOLD signal in the optic fiber-implanted mouse. Five coronal cuts of the brain of a Thy1 mouse and the BOLD signal produced by the activation of neurons due to the blue light shed on Channelrhodopsin receptors. Note the distortion of the image on the right hemisphere of the brain due to the interference of the ceramic glue attached to the optic fiber, above the surface of the brain. The positive BOLD signal is shown in yellow pixels.

to 473 nm and the power to 10 mW on site, which meant 20 mW from the source, since 50% of the power was lost in the extension and curvature of the 3 meters of optic fiber. Figure 5.7 depicts an example of scan images where the anatomical scan is overlapped with the BOLD signal.

Once the gene of interest was successfully cloned into the construct, Dr. Stefanie Vogel proceeded to double transduce the H9 cells with the above-mentioned Channelrhodopsin plasmid and the Luciferase plasmid. As already mentioned, ChR2 (L132) was placed under the EF1α promoter for constitutive expression of the channel and eGFP reporter to track the channels *in vitro*. Luciferase was placed under MAP2 promoter to enhance maximum expression 2 months after implantation of the cell into the cortex and mCherry fluorescence reporter. After transduction, cells were analyzed for the expression of both constructs and the double positive cells were isolated using FACS sorting. Results of this characterization are summarized in Figure 5.8A. The isolated double transduced cells were cultivated and passaged several times in order to obtain a confluent culture and enough amount of cells for implantation. When the culture was confluent, it was observed under the fluorescent microscope. The resulting images are shown in Figure 5.8B. Moreover, the cells were characterized electrophysiologically to assess the functionality of the cation channels. Laser light was shed over the culture but no depolarization was recorded, as shown in Figure 5.8C.

The results imply a successful double transduction for a very low number of cells and a low expression of both proteins in the double transduced cells. Further characterization of protein expression would be needed in order to decipher the reason of the channel unresponsiveness to the activating blue light. An educated assumption would be that the amount of expressed membrane proteins were not enough to induce depolarization. The low expression of the proteins of interest could be explained by an exhaustion of the expressing machinery of the cell. Remarkably, the construct was successfully expressed in the HEK (Human Embryonic Kidney) 293 cell line, that was used as a control. They responded positively to the electrophysiological stimulation (results of HEK cells not shown in this thesis), which implies that the plasmid was correctly engineered but the H9 cells did not express them in their membrane.

The H9 cells failed to be assessed for successful expression of both genes and function of both proteins, hence we decided to use a different source of cells for our experiments involving implantations and the selectively activated concept was left further unexplored.

A

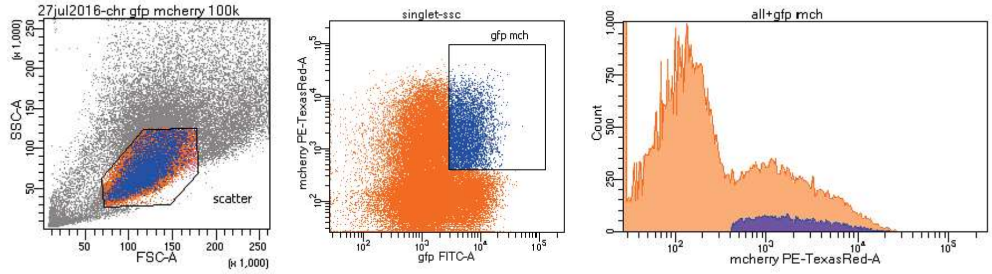

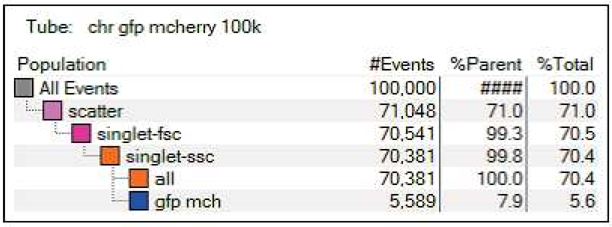

Tube: chr gfp mcherry 100k

Population	#Events	%Parent	%Total
All Events	100,000	####	100.0
scatter	71,048	71.0	71.0
singlet-fsc	70,541	99.3	70.5
singlet-ssc	70,381	99.8	70.4
all	70,381	100.0	70.4
gfp mch	5,589	7.9	5.6

B

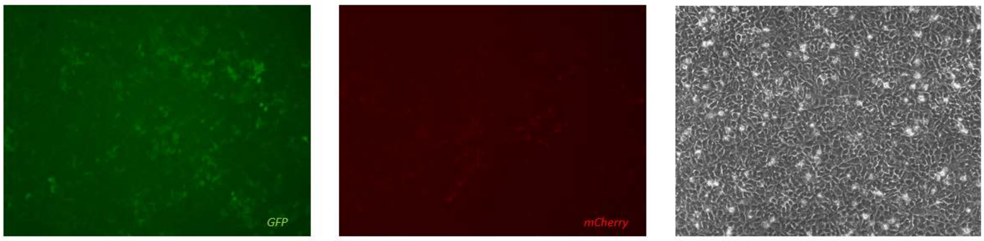

C

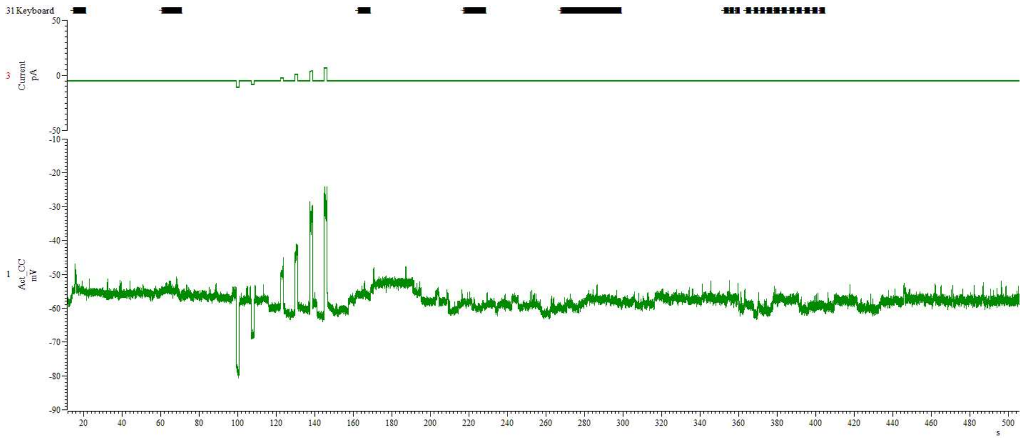

Figure 5.8: Isolation and characterization of double transduced H9 cells for optogenetics. A) FACS analysis of transduced H9 cells. In orange all the quantified events, in blue the double positive events EF1α-ChR2(L132)-eGFP + MAP2-Luc2-mCherry. Note the low proportion of double transduced cells compared to the total amount of cells (previous page). B) Microscope analysis of the double transduced cells. On the left the green channel for eGFP signal, on the center the red channel for mCherry signal, on the right phase contrast image of the culture (previous page). C) Electrophysiological validation of cation channels activity. The black stripes on top of the image depict the stimulation of the cells with a 473 nm laser. Electrophysiological recordings were made by Dr. Collienne in the lab of Prof. Dr. Kloppenburg, Biocenter, Cologne.

6

CHAPTER 6

CONCLUDING REMARKS

6.1 General discussion

In this thesis I uniquely investigated functional changes in the mouse brain that undergoes an ischemic damage and a potential therapy with neural stem cells. I divided the thesis project into two major parts so that I could present preliminary results halfway and make decisions about further experimental setup for the cell engraftment. Both parts belong to the same project which entailed following up functional alterations of a predefined network after a cortical stroke was treated with neural stem cell implantations. I was able to verify that, even though stem cell therapy has been widely proposed as a potential treatment for ischemic damage, there is little if not null information reported about longitudinal studies that can mimic a chronic state in the rodent. The functional changes measured by means of resting state fMRI represent only one approach of the changes happening after the ischemic insult and cell engraftment. Supplementary approaches were included in my project in order to have a more complete picture of the developing changes. I followed the viability of implanted cells, the distribution and recruitment of two inflammation-activated cell types such as microglia and astrocytes, I checked for the migration of implanted cells at the end of the experiment, the formation of scar tissue in the graft location, the phenotypic development and electrical activity of the graft and the changes in fractional anisotropy in the lesion core. Moreover, I also supplemented all imaging techniques with behavioral testing to have a better understanding about the loss and potential recovery of motor and sensorial functions.

In this longitudinal study, no behavioral functional improvement was observed with the implantation of neural stem cells. Results from other groups have been inconclusive in regard with the benefits reported after the sub-acute stage of stroke. Kim and colleagues reported no clear benefits 3 weeks after cell implantation in the dMCAO-induced ischemic rat brain (Kim et al., 2007), Hicks and colleagues observed modest recovery in the forelimb asymmetry task, but none in the staircase task (Hicks et al., 2009) and Daadi and colleagues observed improvement when cells were implanted in the striatum, assessed in the cylinder test (Daadi et al., 2008). In mice, several groups have reported functional improvement when cells are implanted in ischemic brains – filament model – (Stroemer et al., 2009; Hassani et al., 2012). Taken together, these results lead to the conclusion that the success in functional recovery depends on several factors such as the coordinates of cell engraftment, the severity of the stroke – transient filament or permanent coagulation models –, the species used and most importantly the power of the sensorimotor behavioral test to detect deficits caused by the stroke and benefits provided by the cells. Therefore, if the cells implanted in our project are contributing to the recovery of the affected functions is a finding we have not observed. Behavioral recovery cannot be discarded if a different experimental set up is proposed, including longer observation periods and more sensitive behavioral tests.

Van Meer and colleagues reported the loss of bilateral sensorimotor network connectivity measured by resting state, following transient filament MCAO (van Meer et al., 2010a, 2010b). We observed that the sensorimotor network is also sensitive to cortical damage caused by stereotaxic injection. Our results are not in coherence with theirs since we do not observe loss of connectivity after ischemic damage and one of the reasons is probably the extent and severity of the stroke. As already described in previous chapters, we obtained smaller areas of edematous tissue compared to the filament MCAO and an increase of network functional connectivity intensity after stroke onset. It would be interesting to test the relationship between lesion size and connectivity strength more accurately. However, we would be sacrificing reproducibility of the lesion location and survival rates if we were to mimic a larger stroke size; it would also be less useful to the human therapeutic approach.

Green and colleagues tested an experimental setup very similar to mine (Green et al., 2018). We implanted H9 neural stem cells into the cortex of an ischemic brain, induced by filament MCAO. Their results linked the cell vitality to functional connectivity strength: once the cells started dying, the correlation factors among selected regions of interest also decreased. We did not find such connection: the cells implanted in my project survived steadily during the entire observation period of 12 weeks, both in the naïve or in the ischemic brain, which brings me to the conclusion that the size of the inflammatory reaction caused by the ischemic lesion is small enough to preserve the viability of the graft. The network connectivity in my experiments was not linked to the viability of the cells but to the combination of surgical procedures performed in the mouse brain: whereas dMCAO or cell implantation in the naïve brain elicited hyperconnectivity in the selected network, the combination of both (one surgery following the other with time gap of one week) made the network lose its strength, referencing to pre-surgeries values. It is also important to mention that the observed changes among

ROIs depend greatly on the threshold we choose to set the cutting value. The threshold must be chosen taking into account the distribution of data behind the average values displayed in the matrices (which will impact in the standard deviation of each mean) and also taking into account the threshold from earlier studies that have used the same analysis methodology, in order to be able to compare the obtained results in a context. As mentioned before, Green and colleagues performed the only study available in the literature that combined implantation of cells in an ischemic model in the mouse brain and seed-based functional connectivity analysis in a longitudinal study (Green et al., 2018). Hence, I decided to compare my results to hers and chose the same threshold value. Lowering such value would have meant the inclusion of more changes to report, as evidenced in the numerical half of the matrices, since the changes are placed in a continuum compared to baseline and a more complex network of changes to analyze. Raising the threshold would have had the consequence of missing out some of the observed changes and even the risk of not reporting any change.

Because of the above-mentioned methodological limitations when processing the resting state fMRI data and the availability of several approaches to check network strength, the absolute interpretation of results is a challenge. Hyper- and hypoconnectivity of networks have both been reported in pathological brains, therefore it is impossible to affirm which one of those states is closer to a healthy brain. Judging the therapeutic potential of stem cell implantation by solely looking at the connectivity changes in the network would lead to inaccurate and premature conclusions because it is impossible to distinguish if an increase or a decrease in connectivity leads to recovery of the disturbed network, as stated above. More longitudinal studies are needed to establish “normal development of network connectivity” after an ischemic insult followed by the disruption of the parenchyma architecture due to the cell implantation procedure. My study was the first to follow up such development in the whole brain, an approach that was enabled thanks to the mild changes in the symmetry axis of the brain after dMCAO – compared to the filament model – and to a thorough manual drawing of structures for each subject around the affected cortical area and hippocampus expansion.

In order to restore neuronal circuits lost in the ischemic damage, engrafted neural stem cells should go through certain milestones: the cells should integrate into the host tissue, they should differentiate into mature neurons with synaptic characteristics, they should be able to couple to other phenotypically similar cells and they should project neurites to long-distant regions. The patch-clamp electrophysiology experiments revealed that the recorded cells are able to generate and transmit action potentials. The Biocytin intracellular labeling displayed in Figure 4.16C showed neuronal morphology with wide-branching processes projecting outside of the graft. Even though I observed the formation of a glial scar around the graft area, this did not prevent the neurite outgrowth in this model of stroke. This breaks through past findings with similar and weaker astrocytic reaction observed in our lab. The cells seem to be integrating well in the host tissue, yet we observe no behavioral improvement, no therapeutic effect. Therefore, it is not enough for cells to fulfill all the requisites described above, they also need to specialize into the type of neuron that has been lost in order to have a successful integration. By specialization, I am implying that they need to reinstate the exact function that was lost, in the moment that is needed, projecting towards specific neurons belonging to a certain network that was damaged. To illustrate this statement, let us imagine a focal network damage located in the "limbs" subregion of the primary somatosensory cortex which functional consequence is the loss of neuronal firing upon sensory stimulus exposure. If neural stem cells are grafted next to the damaged tissue, they differentiate into mature neurons, show electrical potential, project neurites to adjacent tissue but do not contribute to restoring the sensitivity of the limb, then the cell therapy is unsuccessful, whatever the mechanism of action (direct replacement or bystander effect).

In summary, I have observed that the grafted cells have integrated in the tissue but have not resolved behavioral deficits. It would be interesting to assess the behavior with different sensorimotor test or different strain of mice in order to check if an improvement is detected. The functional connectivity in the sensorimotor network is affected after all surgical procedures: it increases after stroke or cell implantation and it decreases when both surgeries are combined, which seems counterintuitive. The causes underlying this phenomenon are beyond the scope of this thesis.

These conclusions would not have been reached if the experiment wasn't designed to be a longitudinal study *in vivo* with corresponding control groups for all the procedures separately. This is the first study of its kind, where the bilateral sensorimotor connectivity network in all experimental groups is followed up for 12 weeks. We are also the first ones to report the expansion of the hippocampus and shrinkage of the cortex in the chronic period after dMCAO.

6.2 Outlook

The ultimate objective of preclinical research lies in the possibility to use extensively characterized therapies to treat disease in the human being. We mustn't lose sight, even on basic research, that every research project should entail a translational capacity. Longitudinal studies *in vivo* are the most adequate approaches for such purpose since they mimic a long term situation of a therapeutic trial in the living subject, integrating the complexity of the system into the equation.

During the course of this work, I was the first to study the functional connectivity of the sensorimotor network in the whole brain after ischemic damage and after neural stem cell implantation as a therapeutic approach. Many experimental factors determined the success of the experiments, namely the appropriate choice of animal strain, stroke model, cell linage, fluorescence reporters, *in vivo* reporters, just to name a few.

As part of the project, I explored the possibility to remotely activate implanted cells in the brain. The challenges we encountered could be overcome by choosing a different source of cells: DREADD receptors are functional in ESC-derived lt-NES cells and ChannelRhodopsin can be sufficiently expressed on the membrane in other cells lines.

The strong evidence showing alteration in functional brain networks caused by the cell implantation procedure is counterproductive when following the development of brain connectivity in the "normal" progress of the brain after ischemic arrest and after an attempt to place stem cells next to the injury. Future experiments should overcome this limitation by delivering neural stem cells into the injured area without the invasive needle puncture that has been used so far. Some alternative routes of administration have already been thoroughly studied – each with their own pitfalls. Intravenous administration of cells is the quickest and less invasive, but carries the risk of being delivered in many different organs. The blood brain-barrier temporary permeability after stroke would allow the diffusion of the cells into the brain, where they could be attracted by chemogenic factors expressed exclusively by inflamed host tissue, provided that the xenocells had been previously engineered for such chemical gradient recognition.

It has been proposed that cell therapy may improve recovery by immune modulation e.g. secretion of anti-inflammatory cytokines. This would represent an alternative therapy to stem cell delivery, since the cytokine molecules could pass into the brain easier than cells and downregulate pro-inflammatory protein expression at the site where they are being over-expressed. The concentration of inflammation-activated cells in the ischemic area has been widely characterized – also in this thesis. As for the direct cell replacement in the damaged tissue as a therapeutic strategy, a full integration of the neuron is needed. Not only the cell maturity and electric properties should be similar to the surrounding tissue, the engrafted cells should also establish precise synaptic connections with the neurons they need to excite or inhibit, which implies a complex restauration of cellular architecture, to date difficult to envision.

The results of my thesis research project could be complemented assessing behavioral changes with tests that are more sensitive to sensorimotor deficits, such as the cylinder test. Results from this more sensitive behavioral assessment could help decipher if the stem cells are contributing to any functional recovery during the long period of observation. In mice, some sensorimotor deficits recover spontaneously after ischemic damage, the timing depending on the severity of the stroke. Therefore, the proposed dMCAO model seems ideal to study behavioral recovery since it does not affect other cerebral areas outside of the cortex, ensuring survival of all the subjects and guaranteeing that no striatal damage is compromising the overall recovery of the mouse. Moreover, a longer period of observation is desired, since we did not detect return of the motor performance to baseline values within the 3 months after stroke. Finally, a mouse strain that has been thoroughly characterized for fine sensorimotor assessment should be chosen; in our project the Nude mice presented the advantage of no immune rejection against the graft, but the strain had not been extensively studied for behavioral tests, according to the literature. I propose that a different mouse strain is chosen and that the immune rejection of the graft is prevented alternatively, e.g. with cyclosporine.

Tractography of fibers – and any other MRI based technique - could be carried out since the challenges of data processing in the long term dMCAO model have been surpassed. Evaluating the development of structural axonal changes on a microscopic level would shed light on the still-poorly-understood process of neuronal plasticity, particularly if behavioral recovery is observed during the observation period – hence the proposal of longer experiments. It would be interesting to carry out a similar research project in different species to test the outcomes in a larger and more complex brain where spontaneous behavioral recovery has not been documented.

Abbreviations

This list contains the abbreviations that are repeated throughout the entire document, most of them have been introduced in the text. Abbreviations that only appear once have been introduced in the corresponding section and are not included in this list. Plasmid names, solution components, antibodies and chemical formulas are excluded from this list as well.

AMBMC	Australian Mouse Brain Mapping Consortium
AP	Anterior-posterior
ATP	Adenosine triphosphate
BLI	Bioluminescence imaging
BOLD	Blood Oxygenation level dependent
CA	Cornu ammonis
ChR2	ChannelRhodopsin
CNO	Clozapine-N-oxide
CPu	Caudate putamen
DCX	Neuronal migration protein doublecortin
(d)MCA(O)	(distal) Middle cerebral artery (occlusion)
DNA	Deoxyribonucleic acid
DREADD	Designer receptors exclusively activated by a designer drug
DV	Dorso-ventral
eGFP	(enhanced) green fluorescent protein
ESCs	Embryonic stem cells
FA	Fractional anisotropy
FDA	Food and Drug Administration
(f)MRI	(functional) Magnetic resonance imaging
FOV	Field of view
GABA	Gamma-aminobutiric acid

GFAP	Glial fibrillary acidic protein
GPCR	G-protein coupled receptors
GRE-EPI	Gradient-echo echo-planar
(h)NSC	(human) neural stem cells
IL	Interleukin
iPSCs	Induced pluripotent stem cells
LSFM	Lightsheet fluorescence microscopy
lt-NES	long-term self-renewing neuroepithelial-like stem cells
M1	Motor cortex
ML	Medial-lateral
mNDS	modified neurological deficit score
MSCs	Mesenchymal stem cells
MSME	Multi slice multi echo
NMDA	N-methyl-D-aspartate
NMR	Nuclear magnetic resonance
NSPCs	neural stem and precursor cells
ROI	Region of interest
RS	Resting state
SE	Spin echo
SNR	Signal-to-noise
SS1	Primary somatosensory cortex
SS2	Secondary somatosensory cortex
TE	Echo time
Th	Thalamus
TR	Repetition time
V1	Primary visual cortex

List of figures

References

Akaike, N., & Harata, N. (1994). Nystatin perforated patch recording and its applications to analyses of intracellular mechanisms. Jpn J Physiol, 44(5), 433-473.

Albers, G. W., Hart, R. G., Lutsep, H. L., Newell, D. W., & Sacco, R. L. (1999). AHA Scientific Statement. Supplement to the guidelines for the management of transient ischemic attacks: A statement from the Ad Hoc Committee on Guidelines for the Management of Transient Ischemic Attacks, Stroke Council, American Heart Association. Stroke, 30(11), 2502-2511.

Armbruster, B. N., Li, X., Pausch, M. H., Herlitze, S., & Roth, B. L. (2007). Evolving the lock to fit the key to create a family of G protein-coupled receptors potently activated by an inert ligand. Proc Natl Acad Sci U S A, 104(12), 5163-5168. doi:10.1073/pnas.0700293104

Ashby, F. G. (2011). Statistical analysis of fMRI data: MIT Press.

Aswendt, M., Adamczak, J., Couillard-Despres, S., & Hoehn, M. (2013). Boosting bioluminescence neuroimaging: an optimized protocol for brain studies. PLoS One, 8(2), e55662. doi:10.1371/journal.pone.0055662

Avants, B. B., Tustison, N. J., Song, G., Cook, P. A., Klein, A., & Gee, J. C. (2011). A reproducible evaluation of ANTs similarity metric performance in brain image registration. Neuroimage, 54(3), 2033-2044. doi:10.1016/j.neuroimage.2010.09.025

Balkaya, M., Krober, J. M., Rex, A., & Endres, M. (2013). Assessing post-stroke behavior in mouse models of focal ischemia. J Cereb Blood Flow Metab, 33(3), 330-338. doi:10.1038/jcbfm.2012.185

Barbosa da Fonseca, L. M., Gutfilen, B., Rosado de Castro, P. H., Battistella, V., Goldenberg, R. C., Kasai-Brunswick, T., . . . de Freitas, G. R. (2010). Migration and homing of bone-marrow mononuclear cells in chronic ischemic stroke after intra-arterial injection. Exp Neurol, 221(1), 122-128. doi:10.1016/j.expneurol.2009.10.010

Barth, M., & Poser, B. A. (2011). Advances in High-Field BOLD fMRI. Materials (Basel), 4(11), 1941-1955. doi:10.3390/ma4111941

Bender, D., Holschbach, M., & Stocklin, G. (1994). Synthesis of n.c.a. carbon-11 labelled clozapine and its major metabolite clozapine-N-oxide and comparison of their biodistribution in mice. Nucl Med Biol, 21(7), 921-925.

Berger, F., Paulmurugan, R., Bhaumik, S., & Gambhir, S. S. (2008). Uptake kinetics and biodistribution of 14C-D-luciferin--a radiolabeled substrate for the firefly luciferase catalyzed bioluminescence reaction: impact on bioluminescence based reporter gene imaging. Eur J Nucl Med Mol Imaging, 35(12), 2275-2285. doi:10.1007/s00259-008-0870-6

Bhasin, A., Srivastava, M. V., Kumaran, S. S., Mohanty, S., Bhatia, R., Bose, S., . . . Airan, B. (2011). Autologous mesenchymal stem cells in chronic stroke. Cerebrovasc Dis Extra, 1(1), 93-104. doi:10.1159/000333381

Biswal, B., DeYoe, E. A., & Hyde, J. S. (1996). Reduction of physiological fluctuations in fMRI using digital filters. Magn Reson Med, 35(1), 107-113.

Biswal, B., Yetkin, F. Z., Haughton, V. M., & Hyde, J. S. (1995). Functional connectivity in the motor cortex of resting human brain using echo-planar MRI. Magn Reson Med, 34(4), 537-541.

Bjorklund, A., & Lindvall, O. (2000). Cell replacement therapies for central nervous system disorders. Nat Neurosci, 3(6), 537-544. doi:10.1038/75705

Boehm-Sturm, P., Aswendt, M., Minassian, A., Michalk, S., Mengler, L., Adamczak, J., . . . Hoehn, M. (2014). A multi-modality platform to image stem cell graft survival in the naive and stroke-damaged mouse brain. Biomaterials, 35(7), 2218-2226. doi:10.1016/j.biomaterials.2013.11.085

Boyden, E. S., Zhang, F., Bamberg, E., Nagel, G., & Deisseroth, K. (2005). Millisecond-timescale, genetically targeted optical control of neural activity. Nat Neurosci, 8(9), 1263-1268. doi:10.1038/nn1525

Branchini, B. R. (2013). Chemistry of firefly bioluminescence. Retrieved from https://d-nb.info/1020843276/34

Brott, T., Adams, H. P., Jr., Olinger, C. P., Marler, J. R., Barsan, W. G., Biller, J., . . . et al. (1989). Measurements of acute cerebral infarction: a clinical examination scale. Stroke, 20(7), 864-870.

Buhnemann, C., Scholz, A., Bernreuther, C., Malik, C. Y., Braun, H., Schachner, M., . . . Dihne, M. (2006). Neuronal differentiation of transplanted embryonic stem cell-derived precursors in stroke lesions of adult rats. Brain, 129(Pt 12), 3238-3248. doi:10.1093/brain/awl261

Burns, B. L. (2014). Sparse image reconstruction and artifact correction of multidimensional spectroscopic imaging data - PhD thesis. University of California, USA. Retrieved from https://www.researchgate.net/publication/267327279_Sparse_image_reconstruction_and_artifact_correction_of_multi-dimensional_spectroscopic_imaging_data

Caballero-Garrido, E., Pena-Philippides, J. C., Lordkipanidze, T., Bragin, D., Yang, Y., Erhardt, E. B., & Roitbak, T. (2015). In Vivo Inhibition of miR-155 Promotes Recovery after Experimental Mouse Stroke. J Neurosci, 35(36), 12446-12464. doi:10.1523/JNEUROSCI.1641-15.2015

Cannon, J. R., & Greenamyre, J. T. (2009). NeuN is not a reliable marker of dopamine neurons in rat substantia nigra. Neurosci Lett, 464(1), 14-17. doi:10.1016/j.neulet.2009.08.023

Cantu, D., Walker, K., Andresen, L., Taylor-Weiner, A., Hampton, D., Tesco, G., & Dulla, C. G. (2015). Traumatic Brain Injury Increases Cortical Glutamate Network Activity by Compromising GABAergic Control. Cereb Cortex, 25(8), 2306-2320. doi:10.1093/cercor/bhu041

Carmichael, S. T. (2005). Rodent models of focal stroke: size, mechanism, and purpose. NeuroRx, 2(3), 396-409. doi:10.1602/neurorx.2.3.396

Castellanos, N. P., Paul, N., Ordonez, V. E., Demuynck, O., Bajo, R., Campo, P., . . . Maestu, F. (2010). Reorganization of functional connectivity as a correlate of cognitive recovery in acquired brain injury. Brain, 133(Pt 8), 2365-2381. doi:10.1093/brain/awq174

Choi, D. W., & Rothman, S. M. (1990). The role of glutamate neurotoxicity in hypoxic-ischemic neuronal death. Annu Rev Neurosci, 13, 171-182. doi:10.1146/annurev.ne.13.030190.001131

Collignon, A., Maes, F., Delaere, D., Vandermeulen, D., Suetens, P., & Marchal, G. (1995). Automated multi-modality image registration based on information theory. Information Processing in Medical Imaging, 263-274. doi:citeulike-article-id:1107095

Contag, P. R., Olomu, I. N., Stevenson, D. K., & Contag, C. H. (1998). Bioluminescent indicators in living mammals. Nat Med, 4(2), 245-247.

Currie, S., Hoggard, N., Craven, I. J., Hadjivassiliou, M., & Wilkinson, I. D. (2013). Understanding MRI: basic MR physics for physicians. Postgrad Med J, 89(1050), 209-223.

doi:10.1136/postgradmedj-2012-131342

Daadi, M. M., Maag, A. L., & Steinberg, G. K. (2008). Adherent self-renewable human embryonic stem cell-derived neural stem cell line: functional engraftment in experimental stroke model. PLoS One, 3(2), e1644. doi:10.1371/journal.pone.0001644

Deisseroth, K. (2010). Controlling the brain with light. Sci Am, 303(5), 48-55.

Detante, O., Moisan, A., Dimastromatteo, J., Richard, M. J., Riou, L., Grillon, E., . . . Remy, C. (2009). Intravenous administration of 99mTc-HMPAO-labeled human mesenchymal stem cells after stroke: in vivo imaging and biodistribution. Cell Transplant, 18(12), 1369-1379. doi:10.3727/096368909X474230

Dezawa, M., Kanno, H., Hoshino, M., Cho, H., Matsumoto, N., Itokazu, Y., . . . Ide, C. (2004). Specific induction of neuronal cells from bone marrow stromal cells and application for autologous transplantation. J Clin Invest, 113(12), 1701-1710. doi:10.1172/JCI20935

Dirnagl, U. (2004). Inflammation in stroke: the good, the bad, and the unknown. Ernst Schering Res Found Workshop(47), 87-99.

Disbrow, E. A., Slutsky, D. A., Roberts, T. P., & Krubitzer, L. A. (2000). Functional MRI at 1.5 tesla: a comparison of the blood oxygenation level-dependent signal and electrophysiology. Proc Natl Acad Sci U S A, 97(17), 9718-9723. doi:10.1073/pnas.170205497

Dodt, H. U., Leischner, U., Schierloh, A., Jahrling, N., Mauch, C. P., Deininger, K., . . . Becker, K. (2007). Ultramicroscopy: three-dimensional visualization of neuronal networks in the whole mouse brain. Nat Methods, 4(4), 331-336. doi:10.1038/nmeth1036

Doeppner, T. R., Ewert, T. A., Tonges, L., Herz, J., Zechariah, A., ElAli, A., . . . Bahr, M. (2012). Transduction of neural precursor cells with TAT-heat shock protein 70 chaperone: therapeutic potential against ischemic stroke after intrastriatal and systemic transplantation. Stem Cells, 30(6), 1297-1310. doi:10.1002/stem.1098

Drexel, M., Puhakka, N., Kirchmair, E., Hortnagl, H., Pitkanen, A., & Sperk, G. (2015). Expression of GABA receptor subunits in the hippocampus and thalamus after experimental traumatic brain injury. Neuropharmacology, 88, 122-133. doi:10.1016/j.neuropharm.2014.08.023

Ellis, J. A., Youngerman, B. E., Higashida, R. T., Altschul, D., & Meyers, P. M. (2011). Endovascular treatment strategies for acute ischemic stroke. Int J Stroke, 6(6), 511-522. doi:10.1111/j.1747-4949.2011.00670.x

Feng, G., Mellor, R. H., Bernstein, M., Keller-Peck, C., Nguyen, Q. T., Wallace, M., . . . Sanes, J. R. (2000). Imaging neuronal subsets in transgenic mice expressing multiple spectral variants of GFP. Neuron, 28(1), 41-51.

Fox, P. T., & Raichle, M. E. (1986). Focal physiological uncoupling of cerebral blood flow and oxidative metabolism during somatosensory stimulation in human subjects. Proc Natl Acad Sci U S A, 83(4), 1140-1144.

Freret, T., Bouet, V., Leconte, C., Roussel, S., Chazalviel, L., Divoux, D., . . . Boulouard, M. (2009). Behavioral deficits after distal focal cerebral ischemia in mice: Usefulness of adhesive removal test. Behav Neurosci, 123(1), 224-230. doi:10.1037/a0014157

G., M. J. a. M. (2004). The atlas of heart disease and stroke. Retrieved from http://www.who.int/cardiovascular_diseases/resources/atlas/en/

Goense, J. B., Zappe, A. C., & Logothetis, N. K. (2007). High-resolution fMRI of macaque V1.

Magn Reson Imaging, 25(6), 740-747. doi:10.1016/j.mri.2007.02.013

Grandjean, J., Schroeter, A., Batata, I., & Rudin, M. (2014). Optimization of anesthesia protocol for resting-state fMRI in mice based on differential effects of anesthetics on functional connectivity patterns. Neuroimage, 102 Pt 2, 838-847. doi:10.1016/j.neuroimage.2014.08.043

Green, C. (2017). Structural and functional characterization of neuronal network changes with MRI in the mouse brain - PhD thesis., University of Cologne, Germany,. Retrieved from https://kups.ub.uni-koeln.de/7626/

Green, C., Minassian, A., Vogel, S., Diedenhofen, M., Beyrau, A., Wiedermann, D., & Hoehn, M. (2018). Sensorimotor Functional and Structural Networks after Intracerebral Stem Cell Grafts in the Ischemic Mouse Brain. J Neurosci, 38(7), 1648-1661. doi:10.1523/JNEUROSCI.2715-17.2018

Gusel'nikova, V. V., & Korzhevskiy, D. E. (2015). NeuN As a Neuronal Nuclear Antigen and Neuron Differentiation Marker. Acta Naturae, 7(2), 42-47.

Gusnard, D. A., Raichle, M. E., & Raichle, M. E. (2001). Searching for a baseline: functional imaging and the resting human brain. Nat Rev Neurosci, 2(10), 685-694. doi:10.1038/35094500

Hahn, E. L. (1950). Spin Echoes. Physical Review, 80(4), 580-594. doi:10.1103/PhysRev.80.580

Hamzei Taj, S., Kho, W., Riou, A., Wiedermann, D., & Hoehn, M. (2016). MiRNA-124 induces neuroprotection and functional improvement after focal cerebral ischemia. Biomaterials, 91, 151-165. doi:10.1016/j.biomaterials.2016.03.025

Harris, N. G., Verley, D. R., Gutman, B. A., Thompson, P. M., Yeh, H. J., & Brown, J. A. (2016). Disconnection and hyper-connectivity underlie reorganization after TBI: A rodent functional connectomic analysis. Exp Neurol, 277, 124-138. doi:10.1016/j.expneurol.2015.12.020

Hassani, Z., O'Reilly, J., Pearse, Y., Stroemer, P., Tang, E., Sinden, J., . . . Thuret, S. (2012). Human neural progenitor cell engraftment increases neurogenesis and microglial recruitment in the brain of rats with stroke. PLoS One, 7(11), e50444. doi:10.1371/journal.pone.0050444

Hayashi, T., Noshita, N., Sugawara, T., & Chan, P. H. (2003). Temporal profile of angiogenesis and expression of related genes in the brain after ischemia. J Cereb Blood Flow Metab, 23(2), 166-180. doi:10.1097/01.WCB.0000041283.53351.CB

He, B. J., Snyder, A. Z., Zempel, J. M., Smyth, M. D., & Raichle, M. E. (2008). Electrophysiological correlates of the brain's intrinsic large-scale functional architecture. Proc Natl Acad Sci U S A, 105(41), 16039-16044. doi:10.1073/pnas.0807010105

Heiss, W. D. (2016). Malignant MCA Infarction: Pathophysiology and Imaging for Early Diagnosis and Management Decisions. Cerebrovasc Dis, 41(1-2), 1-7. doi:10.1159/000441627

Hermann, D. M., & Chopp, M. (2012). Promoting brain remodelling and plasticity for stroke recovery: therapeutic promise and potential pitfalls of clinical translation. Lancet Neurol, 11(4), 369-380. doi:10.1016/S1474-4422(12)70039-X

Hermann, D. M., Peruzzotti-Jametti, L., Schlechter, J., Bernstock, J. D., Doeppner, T. R., & Pluchino, S. (2014). Neural precursor cells in the ischemic brain - integration, cellular crosstalk, and consequences for stroke recovery. Front Cell Neurosci, 8, 291. doi:10.3389/fncel.2014.00291

Herrmann, O., Baumann, B., de Lorenzi, R., Muhammad, S., Zhang, W., Kleesiek, J., . . . Schwaninger, M. (2005). IKK mediates ischemia-induced neuronal death. Nat Med, 11(12), 1322-1329. doi:10.1038/nm1323

Hicks, A. U., Lappalainen, R. S., Narkilahti, S., Suuronen, R., Corbett, D., Sivenius, J., . . . Jolkkonen, J. (2009). Transplantation of human embryonic stem cell-derived neural precursor cells and enriched environment after cortical stroke in rats: cell survival and functional recovery. Eur J Neurosci, 29(3), 562-574. doi:10.1111/j.1460-9568.2008.06599.x

Hillary, F. G. (2008). Neuroimaging of working memory dysfunction and the dilemma with brain reorganization hypotheses. J Int Neuropsychol Soc, 14(4), 526-534. doi:10.1017/S1355617708080788

Hillary, F. G., Genova, H. M., Chiaravalloti, N. D., Rypma, B., & DeLuca, J. (2006). Prefrontal modulation of working memory performance in brain injury and disease. Hum Brain Mapp, 27(11), 837-847. doi:10.1002/hbm.20226

Hillary, F. G., Roman, C. A., Venkatesan, U., Rajtmajer, S. M., Bajo, R., & Castellanos, N. D. (2015). Hyperconnectivity is a fundamental response to neurological disruption. Neuropsychology, 29(1), 59-75. doi:10.1037/neu0000110

Honmou, O., Houkin, K., Matsunaga, T., Niitsu, Y., Ishiai, S., Onodera, R., . . . Kocsis, J. D. (2011). Intravenous administration of auto serum-expanded autologous mesenchymal stem cells in stroke. Brain, 134(Pt 6), 1790-1807. doi:10.1093/brain/awr063

Horn, R., & Marty, A. (1988). Muscarinic activation of ionic currents measured by a new whole-cell recording method. J Gen Physiol, 92(2), 145-159.

Howarth, C., Gleeson, P., & Attwell, D. (2012). Updated energy budgets for neural computation in the neocortex and cerebellum. J Cereb Blood Flow Metab, 32(7), 1222-1232. doi:10.1038/jcbfm.2012.35

James, M. L., & Gambhir, S. S. (2012). A molecular imaging primer: modalities, imaging agents, and applications. Physiol Rev, 92(2), 897-965. doi:10.1152/physrev.00049.2010

Jenkinson, M., Bannister, P., Brady, M., & Smith, S. (2002). Improved optimization for the robust and accurate linear registration and motion correction of brain images. Neuroimage, 17(2), 825-841.

Jenkinson, M., & Smith, S. (2001). A global optimisation method for robust affine registration of brain images. Med Image Anal, 5(2), 143-156.

Jezzard, P., & Balaban, R. S. (1995). Correction for geometric distortion in echo planar images from B0 field variations. Magn Reson Med, 34(1), 65-73.

Kalthoff, D. (2011). Functional connectivity of the rat brain in MRI - PhD thesis. RWTH Aachen University, Germany. Retrieved from https://d-nb.info/1020843276/34

Kaneko, D., Nakamura, N., & Ogawa, T. (1985). Cerebral infarction in rats using homologous blood emboli: development of a new experimental model. Stroke, 16(1), 76-84.

Kenmuir, C. L., & Wechsler, L. R. (2017). Update on cell therapy for stroke. Stroke Vasc Neurol, 2(2), 59-64. doi:10.1136/svn-2017-000070

Kim, D. Y., Park, S. H., Lee, S. U., Choi, D. H., Park, H. W., Paek, S. H., . . . Lim, J. H. (2007). Effect of human embryonic stem cell-derived neuronal precursor cell transplantation into the cerebral infarct model of rat with exercise. Neurosci Res, 58(2), 164-175. doi:10.1016/j.neures.2007.02.016

Kim, S. U., & de Vellis, J. (2009). Stem cell-based cell therapy in neurological diseases: a review. J Neurosci Res, 87(10), 2183-2200. doi:10.1002/jnr.22054

Knight, J. C., Scharf, E. L., & Mao-Draayer, Y. (2010). Fas activation increases neural progenitor cell survival. J Neurosci Res, 88(4), 746-757. doi:10.1002/jnr.22253

Koizumi, J.-i., Yoshida, Y., Nakazawa, T., & Ooneda, G. (1986). Experimental studies of ischemic brain edema

1. A new experimental model of cerebral embolism in rats in which recirculation can be introduced in the ischemic area. Nosotchu, 8(1), 1-8. doi:10.3995/jstroke.8.1

Kuraoka, M., Furuta, T., Matsuwaki, T., Omatsu, T., Ishii, Y., Kyuwa, S., & Yoshikawa, Y. (2009). Direct experimental occlusion of the distal middle cerebral artery induces high reproducibility of brain ischemia in mice. Exp Anim, 58(1), 19-29.

Lee, J. S., Hong, J. M., Moon, G. J., Lee, P. H., Ahn, Y. H., Bang, O. Y., & collaborators, S. (2010). A long-term follow-up study of intravenous autologous mesenchymal stem cell transplantation in patients with ischemic stroke. Stem Cells, 28(6), 1099-1106. doi:10.1002/stem.430

Lein, E. S., Hawrylycz, M. J., Ao, N., Ayres, M., Bensinger, A., Bernard, A., . . . Jones, A. R. (2007). Genome-wide atlas of gene expression in the adult mouse brain. Nature, 445(7124), 168-176. doi:10.1038/nature05453

Leopold, D. A., Murayama, Y., & Logothetis, N. K. (2003). Very slow activity fluctuations in monkey visual cortex: implications for functional brain imaging. Cereb Cortex, 13(4), 422-433.

Liang, Z., Liu, X., & Zhang, N. (2015). Dynamic resting state functional connectivity in awake and anesthetized rodents. Neuroimage, 104, 89-99. doi:10.1016/j.neuroimage.2014.10.013

Lin, A. L., Fox, P. T., Hardies, J., Duong, T. Q., & Gao, J. H. (2010). Nonlinear coupling between cerebral blood flow, oxygen consumption, and ATP production in human visual cortex. Proc Natl Acad Sci U S A, 107(18), 8446-8451. doi:10.1073/pnas.0909711107

Lindvall, O., & Bjorklund, A. (2004). Cell therapy in Parkinson's disease. NeuroRx, 1(4), 382-393. doi:10.1602/neurorx.1.4.382

Lindvall, O., & Kokaia, Z. (2011). Stem cell research in stroke: how far from the clinic? Stroke, 42(8), 2369-2375. doi:10.1161/STROKEAHA.110.599654

Lo, E. H., Dalkara, T., & Moskowitz, M. A. (2003). Mechanisms, challenges and opportunities in stroke. Nat Rev Neurosci, 4(5), 399-415. doi:10.1038/nrn1106

Logothetis, N. K. (2003). The underpinnings of the BOLD functional magnetic resonance imaging signal. J Neurosci, 23(10), 3963-3971.

Longa, E. Z., Weinstein, P. R., Carlson, S., & Cummins, R. (1989). Reversible middle cerebral artery occlusion without craniectomy in rats. Stroke, 20(1), 84-91.

Lopez, A. D., & Mathers, C. D. (2006). Measuring the global burden of disease and epidemiological transitions: 2002-2030. Ann Trop Med Parasitol, 100(5-6), 481-499. doi:10.1179/136485906X97417

Lubjuhn, J., Gastens, A., von Wilpert, G., Bargiotas, P., Herrmann, O., Murikinati, S., . . . Schwaninger, M. (2009). Functional testing in a mouse stroke model induced by occlusion of the distal middle cerebral artery. J Neurosci Methods, 184(1), 95-103. doi:10.1016/j.jneumeth.2009.07.029

Lundkvist, J., & Lendahl, U. (2001). Notch and the birth of glial cells. Trends Neurosci, 24(9), 492-494.

Lyden, P. D., Zweifler, R., Mahdavi, Z., & Lonzo, L. (1994). A rapid, reliable, and valid method for measuring infarct and brain compartment volumes from computed tomographic scans. Stroke, 25(12), 2421-2428.

Macrae, I. M. (2011). Preclinical stroke research--advantages and disadvantages of the most common rodent models of focal ischaemia. Br J Pharmacol, 164(4), 1062-1078. doi:10.1111/j.1476-5381.2011.01398.x

Macrae, I. M., Robinson, M. J., Graham, D. I., Reid, J. L., & McCulloch, J. (1993). Endothelin-1-induced reductions in cerebral blood flow: dose dependency, time course, and neuropathological consequences. J Cereb Blood Flow Metab, 13(2), 276-284. doi:10.1038/jcbfm.1993.34

Mangia, S., Giove, F., Tkac, I., Logothetis, N. K., Henry, P. G., Olman, C. A., . . . Ugurbil, K. (2009). Metabolic and hemodynamic events after changes in neuronal activity: current hypotheses, theoretical predictions and in vivo NMR experimental findings. J Cereb Blood Flow Metab, 29(3), 441-463. doi:10.1038/jcbfm.2008.134

Marti, H. J., Bernaudin, M., Bellail, A., Schoch, H., Euler, M., Petit, E., & Risau, W. (2000). Hypoxia-induced vascular endothelial growth factor expression precedes neovascularization after cerebral ischemia. Am J Pathol, 156(3), 965-976. doi:10.1016/S0002-9440(10)64964-4

Matsuno-Yagi, A., & Mukohata, Y. (1977). Two possible roles of bacteriorhodopsin; a comparative study of strains of Halobacterium halobium differing in pigmentation. Biochem Biophys Res Commun, 78(1), 237-243.

McGill, J. K., Gallagher, L., Carswell, H. V., Irving, E. A., Dominiczak, A. F., & Macrae, I. M. (2005). Impaired functional recovery after stroke in the stroke-prone spontaneously hypertensive rat. Stroke, 36(1), 135-141. doi:10.1161/01.STR.0000149629.32525.b7

McKeon, R. J., Schreiber, R. C., Rudge, J. S., & Silver, J. (1991). Reduction of neurite outgrowth in a model of glial scarring following CNS injury is correlated with the expression of inhibitory molecules on reactive astrocytes. J Neurosci, 11(11), 3398-3411.

McPhail, L. T., McBride, C. B., McGraw, J., Steeves, J. D., & Tetzlaff, W. (2004). Axotomy abolishes NeuN expression in facial but not rubrospinal neurons. Exp Neurol, 185(1), 182-190.

Mirza, B., Krook, H., Andersson, P., Larsson, L. C., Korsgren, O., & Widner, H. (2004). Intracerebral cytokine profiles in adult rats grafted with neural tissue of different immunological disparity. Brain Res Bull, 63(2), 105-118. doi:10.1016/j.brainresbull.2004.01.009

Mora-Lee, S., Sirerol-Piquer, M. S., Gutierrez-Perez, M., Gomez-Pinedo, U., Roobrouck, V. D., Lopez, T., . . . Garcia-Verdugo, J. M. (2012). Therapeutic effects of hMAPC and hMSC transplantation after stroke in mice. PLoS One, 7(8), e43683. doi:10.1371/journal.pone.0043683

Muthaian, R., Minhas, G., & Anand, A. (2012). Pathophysiology of stroke and stroke-induced retinal ischemia: emerging role of stem cells. J Cell Physiol, 227(3), 1269-1279. doi:10.1002/jcp.23048

Nagel, G., Szellas, T., Huhn, W., Kateriya, S., Adeishvili, N., Berthold, P., . . . Bamberg, E. (2003). Channelrhodopsin-2, a directly light-gated cation-selective membrane channel. Proc Natl Acad Sci U S A, 100(24), 13940-13945. doi:10.1073/pnas.1936192100

Neuhaus, A. A., Couch, Y., Hadley, G., & Buchan, A. M. (2017). Neuroprotection in stroke: the importance of collaboration and reproducibility. Brain, 140(8), 2079-2092. doi:10.1093/

brain/awx126

Norrving, B., & Kissela, B. (2013). The global burden of stroke and need for a continuum of care. Neurology, 80(3 Suppl 2), S5-12. doi:10.1212/WNL.0b013e3182762397

Oesterhelt, D., & Stoeckenius, W. (1971). Rhodopsin-like protein from the purple membrane of Halobacterium halobium. Nat New Biol, 233(39), 149-152.

Ogawa, S., Lee, T. M., Nayak, A. S., & Glynn, P. (1990). Oxygenation-sensitive contrast in magnetic resonance image of rodent brain at high magnetic fields. Magn Reson Med, 14(1), 68-78.

Oki, K., Tatarishvili, J., Wood, J., Koch, P., Wattananit, S., Mine, Y., . . . Kokaia, Z. (2012). Human-induced pluripotent stem cells form functional neurons and improve recovery after grafting in stroke-damaged brain. Stem Cells, 30(6), 1120-1133. doi:10.1002/stem.1104

Ord, E. N., Shirley, R., van Kralingen, J. C., Graves, A., McClure, J. D., Wilkinson, M., . . . Work, L. M. (2012). Positive impact of pre-stroke surgery on survival following transient focal ischemia in hypertensive rats. J Neurosci Methods, 211(2), 305-308. doi:10.1016/j.jneumeth.2012.09.001

Orset, C., Macrez, R., Young, A. R., Panthou, D., Angles-Cano, E., Maubert, E., . . . Vivien, D. (2007). Mouse model of in situ thromboembolic stroke and reperfusion. Stroke, 38(10), 2771-2778. doi:10.1161/STROKEAHA.107.487520

Pena-Philippides, J. C., Yang, Y., Bragina, O., Hagberg, S., Nemoto, E., & Roitbak, T. (2014). Effect of pulsed electromagnetic field (PEMF) on infarct size and inflammation after cerebral ischemia in mice. Transl Stroke Res, 5(4), 491-500. doi:10.1007/s12975-014-0334-1

Raichle, M. E., MacLeod, A. M., Snyder, A. Z., Powers, W. J., Gusnard, D. A., & Shulman, G. L. (2001). A default mode of brain function. Proc Natl Acad Sci U S A, 98(2), 676-682. doi:10.1073/pnas.98.2.676

Rice, B. W., Cable, M. D., & Nelson, M. B. (2001). In vivo imaging of light-emitting probes. J Biomed Opt, 6(4), 432-440. doi:10.1117/1.1413210

Rogan, S. C., & Roth, B. L. (2011). Remote control of neuronal signaling. Pharmacol Rev, 63(2), 291-315. doi:10.1124/pr.110.003020

Rosell, A., Agin, V., Rahman, M., Morancho, A., Ali, C., Koistinaho, J., . . . Montaner, J. (2013). Distal occlusion of the middle cerebral artery in mice: are we ready to assess long-term functional outcome? Transl Stroke Res, 4(3), 297-307. doi:10.1007/s12975-012-0234-1

Roy, C. S., & Sherrington, C. S. (1890). On the Regulation of the Blood-supply of the Brain. J Physiol, 11(1-2), 85-158 117.

Sadikot, R. T., & Blackwell, T. S. (2005). Bioluminescence imaging. Proc Am Thorac Soc, 2(6), 537-540, 511-532. doi:10.1513/pats.200507-067DS

Savitz, S. I. (2015). Developing Cellular Therapies for Stroke. Stroke, 46(7), 2026-2031. doi:10.1161/STROKEAHA.115.007149

Schmid-Elsaesser, R., Zausinger, S., Hungerhuber, E., Baethmann, A., & Reulen, H. J. (1998). A critical reevaluation of the intraluminal thread model of focal cerebral ischemia: evidence of inadvertent premature reperfusion and subarachnoid hemorrhage in rats by laser-Doppler flowmetry. Stroke, 29(10), 2162-2170.

Schwarz, M. K., Scherbarth, A., Sprengel, R., Engelhardt, J., Theer, P., & Giese, G. (2015).

Fluorescent-protein stabilization and high-resolution imaging of cleared, intact mouse brains. PLoS One, 10(5), e0124650. doi:10.1371/journal.pone.0124650

Sharkey, J., Ritchie, I. M., & Kelly, P. A. (1993). Perivascular microapplication of endothelin-1: a new model of focal cerebral ischaemia in the rat. J Cereb Blood Flow Metab, 13(5), 865-871. doi:10.1038/jcbfm.1993.108

Shimada, I. S., Borders, A., Aronshtam, A., & Spees, J. L. (2011). Proliferating reactive astrocytes are regulated by Notch-1 in the peri-infarct area after stroke. Stroke, 42(11), 3231-3237. doi:10.1161/STROKEAHA.111.623280

Sofroniew, M. V., & Vinters, H. V. (2010). Astrocytes: biology and pathology. Acta Neuropathol, 119(1), 7-35. doi:10.1007/s00401-009-0619-8

Steinberg, G. K., Kondziolka, D., Wechsler, L. R., Lunsford, L. D., Coburn, M. L., Billigen, J. B., . . . Schwartz, N. E. (2016). Clinical Outcomes of Transplanted Modified Bone Marrow-Derived Mesenchymal Stem Cells in Stroke: A Phase 1/2a Study. Stroke, 47(7), 1817-1824. doi:10.1161/STROKEAHA.116.012995

Stroemer, P., Patel, S., Hope, A., Oliveira, C., Pollock, K., & Sinden, J. (2009). The neural stem cell line CTX0E03 promotes behavioral recovery and endogenous neurogenesis after experimental stroke in a dose-dependent fashion. Neurorehabil Neural Repair, 23(9), 895-909. doi:10.1177/1545968309335978

Strong, K., Mathers, C., & Bonita, R. (2007). Preventing stroke: saving lives around the world. Lancet Neurol, 6(2), 182-187. doi:10.1016/S1474-4422(07)70031-5

Sukhorukova, E. G. (2014). Nuclear Protein NeuN in Neurons in the Human Substantia Nigra. Neuroscience and Behavioral Physiology, 44(5), 539-541. doi:10.1007/s11055-014-9947-9

Susarla, B. T., Villapol, S., Yi, J. H., Geller, H. M., & Symes, A. J. (2014). Temporal patterns of cortical proliferation of glial cell populations after traumatic brain injury in mice. ASN Neuro, 6(3), 159-170. doi:10.1042/AN20130034

Tamura, A., Graham, D. I., McCulloch, J., & Teasdale, G. M. (1981). Focal cerebral ischaemia in the rat: 1. Description of technique and early neuropathological consequences following middle cerebral artery occlusion. J Cereb Blood Flow Metab, 1(1), 53-60. doi:10.1038/jcbfm.1981.6

Tennstaedt, A., Aswendt, M., Adamczak, J., Collienne, U., Selt, M., Schneider, G., . . . Hoehn, M. (2015). Human neural stem cell intracerebral grafts show spontaneous early neuronal differentiation after several weeks. Biomaterials, 44, 143-154. doi:10.1016/j.biomaterials.2014.12.038

Tijms, B. M., Wink, A. M., de Haan, W., van der Flier, W. M., Stam, C. J., Scheltens, P., & Barkhof, F. (2013). Alzheimer's disease: connecting findings from graph theoretical studies of brain networks. Neurobiol Aging, 34(8), 2023-2036. doi:10.1016/j.neurobiolaging.2013.02.020

Uccelli, A., Moretta, L., & Pistoia, V. (2008). Mesenchymal stem cells in health and disease. Nat Rev Immunol, 8(9), 726-736. doi:10.1038/nri2395

Ullmann, J. F., Watson, C., Janke, A. L., Kurniawan, N. D., & Reutens, D. C. (2013). A segmentation protocol and MRI atlas of the C57BL/6J mouse neocortex. Neuroimage, 78, 196-203. doi:10.1016/j.neuroimage.2013.04.008

van Meer, M. P., Otte, W. M., van der Marel, K., Nijboer, C. H., Kavelaars, A., van der Sprenkel, J. W., . . . Dijkhuizen, R. M. (2012). Extent of bilateral neuronal network reorganization and functional recovery in relation to stroke severity. J Neurosci, 32(13), 4495-4507. doi:10.1523/JNEUROSCI.3662-11.2012

van Meer, M. P., van der Marel, K., Otte, W. M., Berkelbach van der Sprenkel, J. W., & Dijkhuizen, R. M. (2010). Correspondence between altered functional and structural connectivity in the contralesional sensorimotor cortex after unilateral stroke in rats: a combined resting-state functional MRI and manganese-enhanced MRI study. J Cereb Blood Flow Metab, 30(10), 1707-1711. doi:10.1038/jcbfm.2010.124

van Meer, M. P., van der Marel, K., Wang, K., Otte, W. M., El Bouazati, S., Roeling, T. A., . . . Dijkhuizen, R. M. (2010). Recovery of sensorimotor function after experimental stroke correlates with restoration of resting-state interhemispheric functional connectivity. J Neurosci, 30(11), 3964-3972. doi:10.1523/JNEUROSCI.5709-09.2010

Vogel, S., Aswendt, M., Nelles, M., Henn, N., Schneider, G., & Hoehn, M. (2018). Initial graft size and not the innate immune response limit survival of engrafted neural stem cells. J Tissue Eng Regen Med, 12(3), 784-793. doi:10.1002/term.2497

Vogel, S., Collmann, F. M., & Hoehn, M. (2017). Perspectives of In Vivo Bioluminescence Imaging: Application to Basic and Translational Neuroscience. Curr Pharm Des, 23(13), 1963-1973. doi:10.2174/1381612822666161226151811

Watson, B. D., Dietrich, W. D., Busto, R., Wachtel, M. S., & Ginsberg, M. D. (1985). Induction of reproducible brain infarction by photochemically initiated thrombosis. Ann Neurol, 17(5), 497-504. doi:10.1002/ana.410170513

Wegener, S., Weber, R., Ramos-Cabrer, P., Uhlenkueken, U., Wiedermann, D., Kandal, K., . . . Hoehn, M. (2005). Subcortical lesions after transient thread occlusion in the rat: T2-weighted magnetic resonance imaging findings without corresponding sensorimotor deficits. J Magn Reson Imaging, 21(4), 340-346. doi:10.1002/jmri.20270

Weiner, D. M., Meltzer, H. Y., Veinbergs, I., Donohue, E. M., Spalding, T. A., Smith, T. T., . . . Brann, M. R. (2004). The role of M1 muscarinic receptor agonism of N-desmethylclozapine in the unique clinical effects of clozapine. Psychopharmacology (Berl), 177(1-2), 207-216. doi:10.1007/s00213-004-1940-5

Weisskoff, R. M., & Kiihne, S. (1992). MRI susceptometry: image-based measurement of absolute susceptibility of MR contrast agents and human blood. Magn Reson Med, 24(2), 375-383.

Wood, P. L. (1995). Microglia as a unique cellular target in the treatment of stroke: potential neurotoxic mediators produced by activated microglia. Neurol Res, 17(4), 242-248.

Wu, J., Xie, N., Zhao, X., Nice, E. C., & Huang, C. (2012). Dissection of aberrant GPCR signaling in tumorigenesis--a systems biology approach. Cancer Genomics Proteomics, 9(1), 37-50.

Zhang, J., & Chopp, M. (2013). Cell-based therapy for ischemic stroke. Expert Opin Biol Ther, 13(9), 1229-1240. doi:10.1517/14712598.2013.804507

Zhang, S. C., Wernig, M., Duncan, I. D., Brustle, O., & Thomson, J. A. (2001). In vitro differentiation of transplantable neural precursors from human embryonic stem cells. Nat Biotechnol, 19(12), 1129-1133. doi:10.1038/nbt1201-1129

Zhu, H., & Roth, B. L. (2014). DREADD: a chemogenetic GPCR signaling platform. Int J Neuropsychopharmacol, 18(1). doi:10.1093/ijnp/pyu007

ERKLÄRUNG

Ich versichere, dass ich die von mir vorgelegte Dissertation selbständig angefertigt, die benutzten Quellen und Hilfsmittel vollständig angegeben und die Stellen der Arbeit – einschließlich Tabellen, Karten und Abbildungen –, die anderen Werken im Wortlaut oder dem Sinn nach entnommen sind, in jedem Einzelfall als Entlehnung kenntlich gemacht habe; dass diese Dissertation noch keiner anderen Fakultät oder Universität zur Prüfung vorgelegen hat; dass sie – abgesehen von unten angegebenen Teilpublikationen – noch nicht veröffentlicht worden ist, sowie, dass ich eine solche Veröffentlichung vor Abschluss des Promotionsverfahrens nicht vornehmen werde. Die Bestimmungen der Promotionsordnung sind mir bekannt. Die von mir vorgelegte Dissertation ist von Herrn Prof. Dr. Mathias Höhn betreut worden.

Köln, den 17. 12. 2018.